AD-A266 467

Army Research Laboratory

COMPLEX TERRAIN WIND MODEL EVALUATION

Martin E. Lee

ARL-TR-54

June 1993

93-15328

NOTICES

Disclaimers

Destruction Notice

Public reporting burden for this collection of information is estimated to average 1 hour per response, including the time for reviewing instructions, searching existing data sources, gathering and maintaining the data needed, and completing and reviewing the collection of information. Send comments regarding this burden estimate or any other aspect of this collection of information, including suggestions for reducing this burden, to Washington Headquarters Services, Directorate for Information Operations and Reports, 1215 Jefferson Davis Highway, Suite 1204, Arlington, VA 22202-4302, and to the Office of Management and Budget, Paperwork Reduction Project (0704-0188), Washington, DC 20503.

1. AGENCY USE ONLY (Leave blank)	2. REPORT DATE June 1993	3. REPORT TYPE AND DATES COVERED Final

4. TITLE AND SUBTITLE COMPLEX TERRAIN WIND MODEL EVALUATION	5. FUNDING NUMBERS 61102/B53A (6.1)
6. AUTHOR(S) Martin E. Lee	

7. PERFORMING ORGANIZATION NAME(S) AND ADDRESS(ES) U.S. Army Research Laboratory Battlefield Environment Directorate ATTN: AMSRL-BE-S White Sands Missile Range, NM 88002-5501	8. PERFORMING ORGANIZATION REPORT NUMBER ARL-TR-54

9. SPONSORING/MONITORING AGENCY NAME(S) AND ADDRESS(ES) U.S. Army Research Laboratory 2800 Powder Mill Road Adelphi, MD 20783-1145	10. SPONSORING/MONITORING AGENCY REPORT NUMBER

11. SUPPLEMENTARY NOTES

12a. DISTRIBUTION/AVAILABILITY STATEMENT Approved for public release; distribution unlimited.	12b. DISTRIBUTION CODE

13. ABSTRACT (Maximum 200 words) The Winds on Critical Streamline Surfaces (WOCSS) complex terrain wind flow model is designed to simulate lateral, mechanical forcing effects on air flows along elevated, solid boundaries, these effects exert significant influence on observed flow field properties, such as transport and diffusion. The degree to which WOCSS model outputs are more reliable than a basic mass consistency model (that does not address lateral forcing dynamics in complex terrain) is discussed in terms of statistical and spatial results, and conclusions regarding this comparison are presented. Results indicate that the WOCSS model does not predict directional changes resulting from lateral forcing, which is a serious limiting factor in its potential application. The WOCSS model was also found to have an oversimplified mass consistency algorithm, averaging speed-up effects over the entire lateral free-flow surface, which restricts prediction of localized lateral speed-up effects in the vicinity of mechanical flow obstacles. Finally, the WOCSS model tends to over-predict the quantity of flow restricted space under both stable and unstable conditions in the transition from moderate to rugged complex terrain when wind speeds are generally less than or equal to 4.0 m/s. However, despite the observed WOCSS model limitations, the WOCSS model did demonstrate the potential to selectively predict reasonable and significant dynamic lateral forcing spaces over a variety of terrain and stability conditions. And because the observed WOCSS model limitations may be overcome to varying degrees by coupling WOCSS outputs to more directionally responsive models (including forecaster interpretation), it does have the potential to contribute a significantly improved degree of validity in atmospheric flow simulation work required to accurately predict dynamic atmospheric flow structures observed in nature.

14. SUBJECT TERMS Winds on Critical Streamline Surfaces (WOCSS) Model, Objective Wind Analysis (OBWIND) Model, Digital Terrain Elevation Data (DTED)	15. NUMBER OF PAGES 149
	16. PRICE CODE

17. SECURITY CLASSIFICATION OF REPORT Unclassified	18. SECURITY CLASSIFICATION OF THIS PAGE Unclassified	19. SECURITY CLASSIFICATION OF ABSTRACT Unclassified	20. LIMITATION OF ABSTRACT SAR

TABLE OF CONTENTS

iii

LIST OF TABLES

v

LIST OF APPENDIX TABLES

LIST OF FIGURES

LIST OF APPENDIX FIGURES

1 INTRODUCTION

The modeling of wind flow fields over complex terrain is a difficult problem
that is not new to the field of Meteorology (Queney, 1948; Liu and Goodin, 1976).
The complicated flow patterns produced from air flowing past irregular surfaces
and obstacles are similar to wave and eddy features seen in rushing stream wa-
ter. Calculations necessary to predict such flow patterns are, needless to say,
computationaly intensive (Deardorff et al., 1984; Endlich, 1984). To ease the
computational burden, model developers make many simplifying assumptions
regarding flow characteristics and boundary conditions (Kao, 1981). Unfortu-
nately this often leads to an over simplified flow solution. For example, even low
hills can significantly affect wind flow patterns (Smedman and Bergstrom, 1984).
Nastrom et al. (1987) note that complex terrain induces significant variability
to local wind fields.

Real atmospheric flow patterns are marked by complicated trajectories in 3-
dimensional space (Endlich, 1967). Therefore, if realistic wind fields over complex
terrain are to be realized in model outputs, solutions must integrate horizontal
flow behaviors with those in the vertical. When the 3-dimensional mechanical
effects of terrain on flow fields are not considered, then high speed flows through
mountain passes and deviations in flow direction along the edges of solid obsta-
cles will not be correctly modeled (Sherman, 1978).

1.1 Literature Review

Why is so much effort expended in developing models to simulate these compli-
cated wind field behaviors? Accurate representation of wind flow fields is im-
portant to realistically determine where, and in what quantities, air pollutants
may be found (Davis et al., 1984; King and Bunker, 1984). This also applies
to the simulation of dust and smoke aerosol models used to simulate battlefield

1

obscurants (Hoock et al., 1987). The prediction of low level aviation hazard areas in complex terrain (Lee and Hansen, 1989), or deciding where to place wind power stations (Bhumralkar et al., 1980) are other applications areas that require detailed wind field predictions. Because it is not practical to measure wind vector field properties at all locations over a selected area, wind models have been developed to estimate winds at other locations using only a selected amount of available data (Bhumralkar et al., 1980).

Wind flow properties may be studied at many different levels of detail, and that presents design problems to model developers. A major issue among atmospheric modelers has been agreeing upon the scale employed to resolve flow field features (Asculai et al., 1984; Bannon and Zehnder, 1989). Naturally, many modelers would prefer to study flows in great detail, but this has not always been practical because of the computational burdens that detailed models present. However, each major improvement in computer storage capacity and speed eases this problem to some degree. The trend is, therefore, to model flow fields using ever smaller grid spacing – from 100's of kilometers to less than 1 kilometer (Erasmus, 1986; Fast and Takle, 1988). Model performance in this proposal will be examined in a high resolution grid (e.g., $\leq$ 1 km grid spacing).

Consistent approaches that have become widely accepted in the field of complex terrain wind flow modeling include the use of sigma, or terrain following coordinate systems (Mahrer and Pielke, 1975; Mass and Dempsey, 1985), and the assumption of neutral stability throughout the modeled flow field (Beljaars et al., 1987). Also, today's modelers seem to be placing more emphasis on the application of dynamic flow theory (Beljaars et al., 1987; Smith, 1988; Bannon and Zehnder, 1989) than on empirical parameterization of flows (Han et al., 1982; Marwitz, 1983; Dinar, 1984; Lee and Kau, 1984). All these approaches were integrated to a significant degree in developing the model to be evaluated in this proposal (Ludwig and Endlich, 1988).

2

In the relatively short history of wind modeling, some model developers took more complex 3-dimensional approaches than others, to develop very accurate representations of real flow field properties (Dickerson, 1978; Sherman, 1978). For example, Ludwig et al. (1990) developed a model that budgets gravitational potential energy, mgy, and kinetic flow energy, $\frac{1}{2}mv^2$, parallel to wind field streamlines where m is mass, g is acceleration due to gravity, y is distance along the vertical axis, and v is the flow velocity (Sears et al., 1982). This budgeting process allows for lateral mass transfer determinations to be made from mechanical, terrain forcing effects. Lateral mass transfer processes are compared to the overly simplified, vertical forcing method as shown in Figure 1. The part of the lateral transfer potential model that actually calculates wind fields is originally from a previous endeavor (Ludwig and Endlich, 1988) and is referred to as the Winds on Critical Streamline Surfaces (WOCSS) code. There was also a precursor to the WOCSS model, described by Ludwig et al. (1986), which incorporated an initialization scheme that used a very small amount of observation data.

Figure 2 illustrates that the WOCSS code evolved from well researched and widely accepted wind modeling principles. Consideration of lateral mass transfer, although a unique aspect of the WOCSS code, is not the only strong point of this particular model; the WOCSS model is diagnostic, which means that it does not require time-dependent boundary conditions (Endlich, 1984). Prognostic models are used to make time-dependent forecasts via the integration of conservation relations, which involves many added calculations; diagnostic models, however, "are very economical and appear to be effective mesoscale tools when the dominant forcing is terrain ...," according to Pielke (1984, p.480). As a result of selecting the diagnostic approach, Ludwig et al. (1990) were able to develop a compact code that could be installed on micro-computers, and could also be executed relatively faster than many other models that simulate wind flow over rough terrain.

VERTICAL FORCING CASE

FLOW STREAMLINES

COMPLEX TERRAIN

(a)

LATERAL FORCING CASE

FLOW STREAMLINES

COMPLEX TERRAIN

(b)
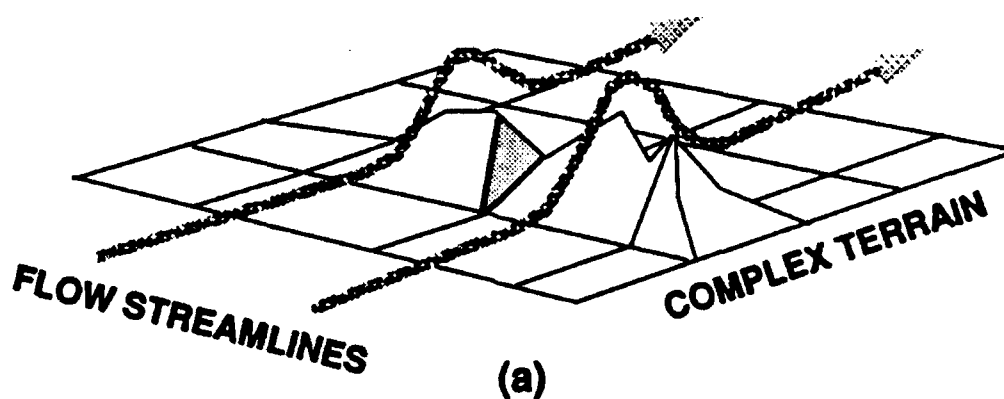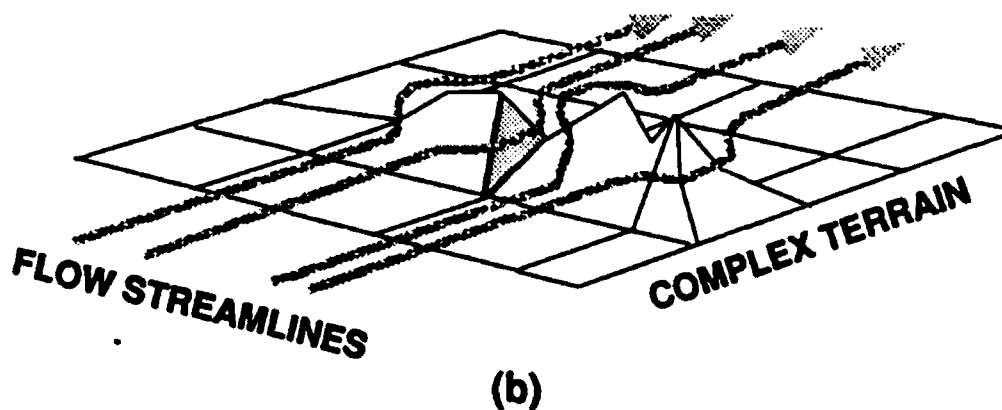
Figure 1. Vertical forcing wind flow model solutions (a) do not make the
necessary potential energy considerations to simulate the effect
of lateral mass transfer that occurs in nature (b).
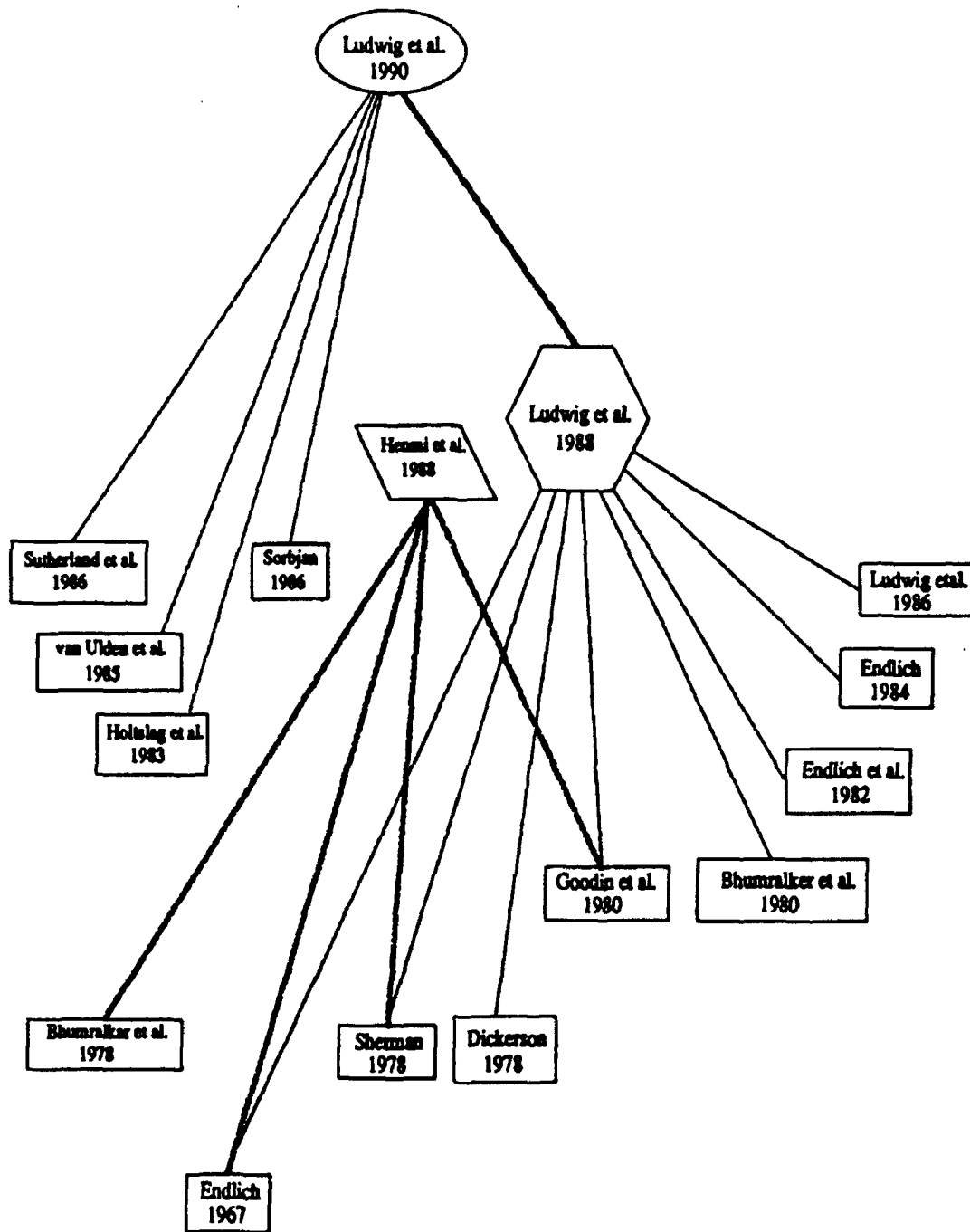
Figure 2. This figure illustrates a map of the reference links, or information scheme, of central importance to this research work. Ludwig and Endlich (1988) describe the wind model selected for validation in this study. The foundation for the design of the model is based on references to well known work in the field of wind modeling. Foundations to some of Henmi's (1988) modeling work, parallel to Ludwig's work, are also illustrated in this figure.

1.2 Hypotheses

The WOCSS complex terrain wind flow model is designed to efficiently simulate: 1) lateral mechanical speed up effects of air flows; and 2) changing wind directions along elevated, solid boundaries. These considerations should make the WOCSS model outputs significantly more reliable than other models that do not address lateral forcing in complex terrain. Therefore, the major assumption made prior to the commencement of this research work was that the WOCSS model was significantly more reliable than basic, vertical forcing wind models because the WOCSS model makes considerations for lateral flow adjustment; it was further assumed that this increase in reliability was not defeated by excessive additional processing time.

1.3 Research Objectives

The WOCSS model has not yet been independently evaluated, and Ludwig et al. (1990) admit that more testing and evaluation of the WOCSS model are required to validate the hypothetical strengths of their model. Therefore, the primary objective of this research work was to implement the WOCSS model on selected computer resources, and establish quantitative, statistical measures of the WOCSS complex terrain model's performance characteristics via comparisons made using high resolution meteorological wind data sets (both surface and upper-air wind profiles), with a basic vertical forcing wind model developed by Henmi and Tabor (1988). Henmi's model, used in this research work, employed an objective wind analysis approach and will hereafter be referred to as the OBWIND model.

The WOCSS evaluation process was carried out using three separate complex terrain surfaces. Finally, the WOCSS model was evaluated using a remote, fourth complex terrain surface under sparse meteorological data initialization conditions; this study was carried out to further appraise the potential utility of the WOCSS model for use in supporting U.S. Army research of battalion-

regiment size battlefield problems. Figure 3 is a conceptual illustration of the basic study design.

The WOCSS model evaluation process carried out in this study represents necessary third party analysis as a step toward model validation. Simply defining model validation has become a significant exercise in itself. However, it is generally considered by many scientific communities to be a process leading to the determination of whether a model reliably predicts events that actually occur in the real world (Hodges and Dewar, 1990). The comparisons described in the previous paragraph were developed to identify measures of the WOCSS model's ability to predict atmospheric flow structures, as they actually occur in nature; and the contrast of model types used in making these comparisons was also intended to improve physical insight into fundamental properties of atmospheric motions in complex terrain (Holton, 1979).
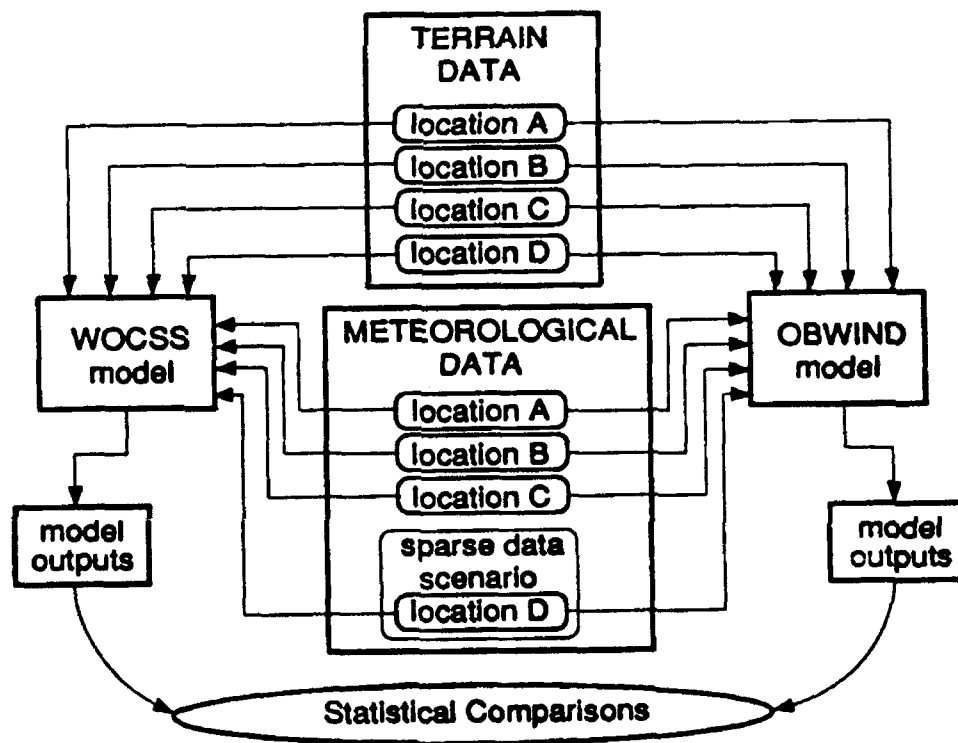
Figure 3. Basic wind model evaluation study design.

2 METHODS

The steps taken to develop this study included the selection of terrain and meteorological data, and preparation of the WOCSS and OBWIND models for case study runs.

2.1 Terrain Data Bases

Four complex terrain sites were selected for use in this validation study. All four complex terrain areas were set to 20.0 km × 20.0 km sizes, representative of selected battalion-regiment size battlefield engagement areas. As a result, these four areas were immediately representative of mesoscale[1] dimensions, in meteorological terms.

The four sites selected were 1) the Orogrande region, located on the White Sands Missile Range (WSMR) in the Tularosa Basin, south central New Mexico; 2) the National Training Center (NTC), Fort Irwin California, which is located south of Death Valley; 3) the Sierra Nevada foothills, near Red Bluff, California; and 4) a complex terrain region approximately 25 km southwest of Pilsen, Czechoslovakia. The general locations, and a contoured, topographic plot, of sites 1-4 are listed in Table 1 and illustrated in Figs. 4-7.

Mesoscale meteorological observation programs have been conducted on complex terrain sites 1-3. In fact, one of the most extensive and detailed meteorological observation programs that has ever been conducted, took place in the site 3 region; this program was called Project WIND (Cionco, 1989). Therefore, site 3 will be referred to hereafter in this report as the Project Wind site. Project WIND will be referred to later when meteorological data is discussed.

---

[1]Pielke (1984, p.1) defines *mesoscale* as a horizontal scale "on the order of a few kilometers to several hundred kilometers or so, with a time scale of about 1 to 12h."

(b)

(a)
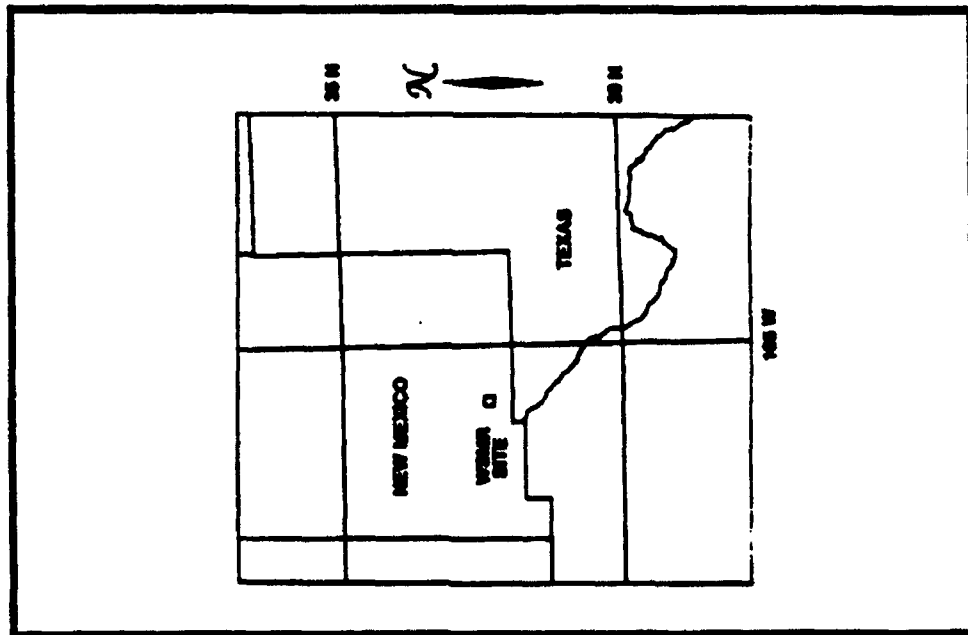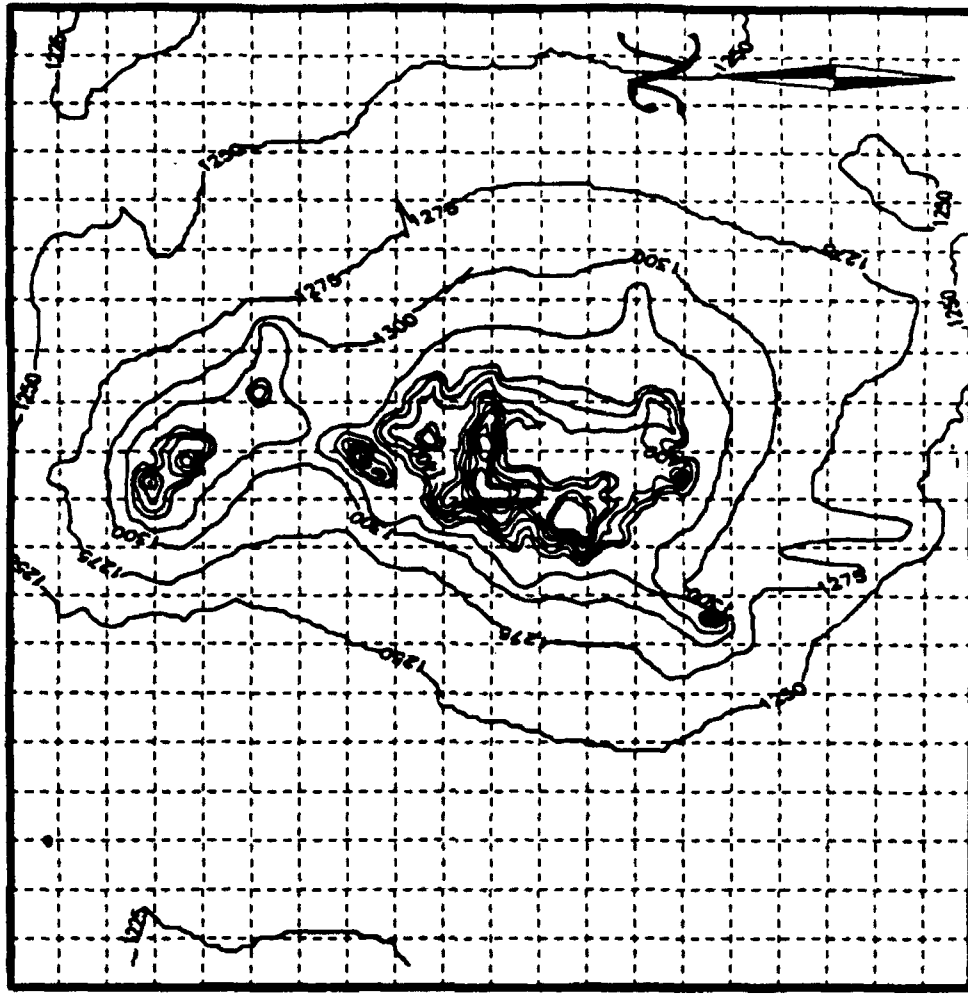
Figure 4. General location of the WSMR site, marked by the small box in south-central New Mexico (a); and a topographic map of the 20 X 20 km site area (b), where each grid cell represents a 1 X 1 km area, with a 25 m contour interval.
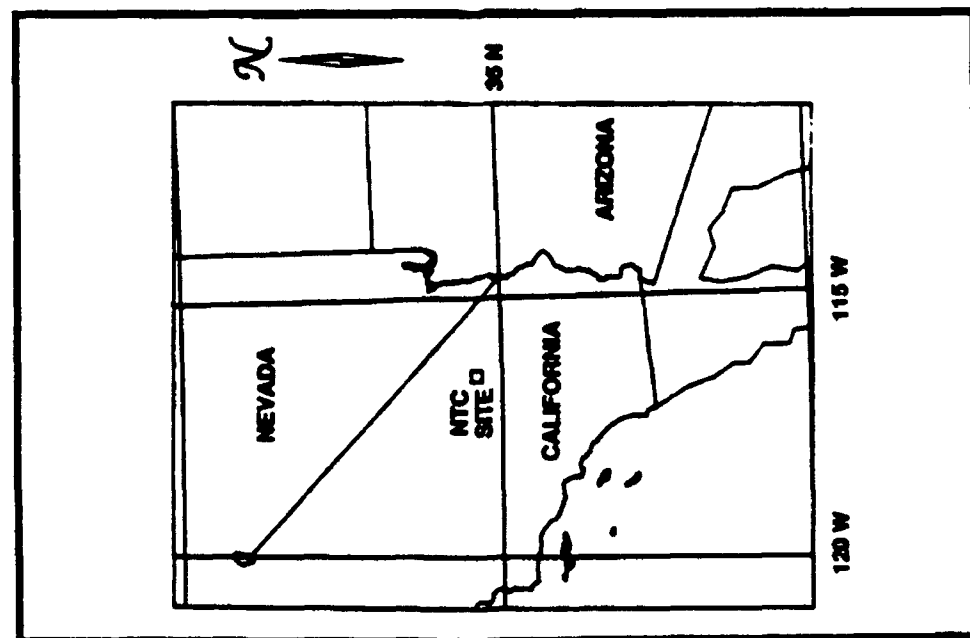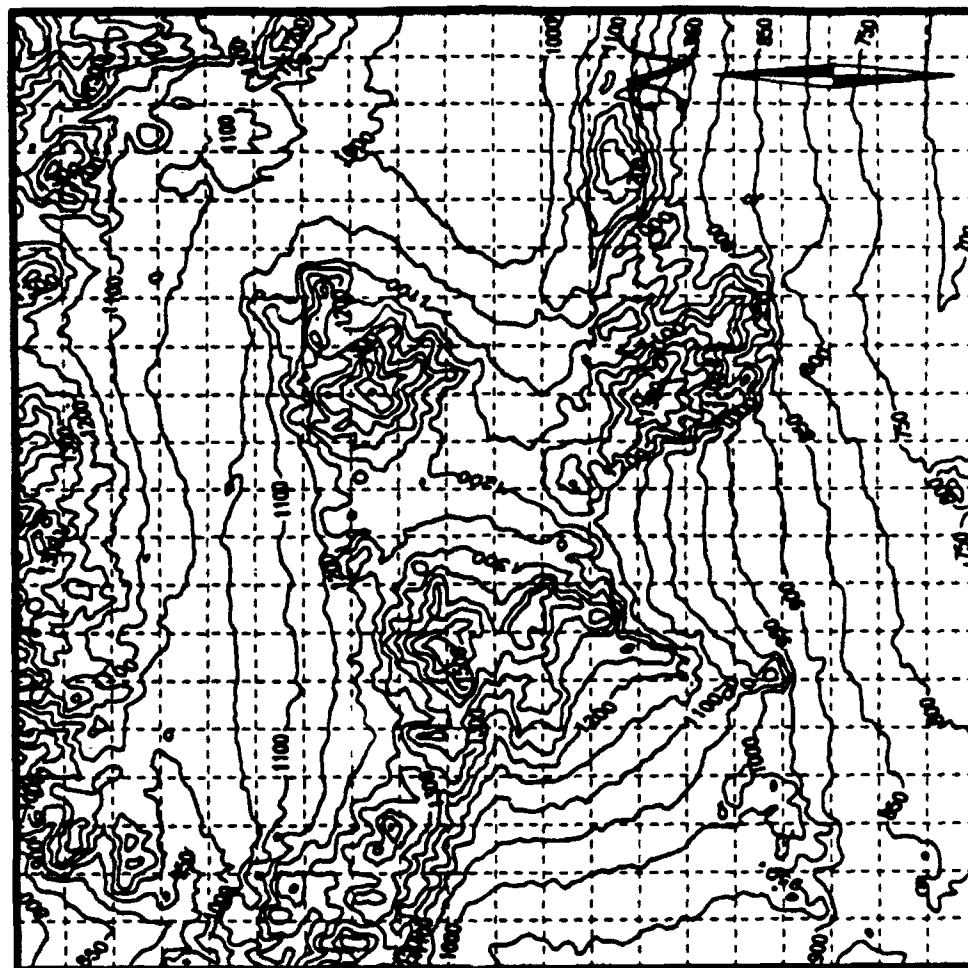
Figure 5. General location of the NTC site, marked by the small box in southeastern California (a); and a topographic map of the 20 X 20 km site area (b), where each grid cell represents a 1 X 1 km area, with a contour interval of 50 m.
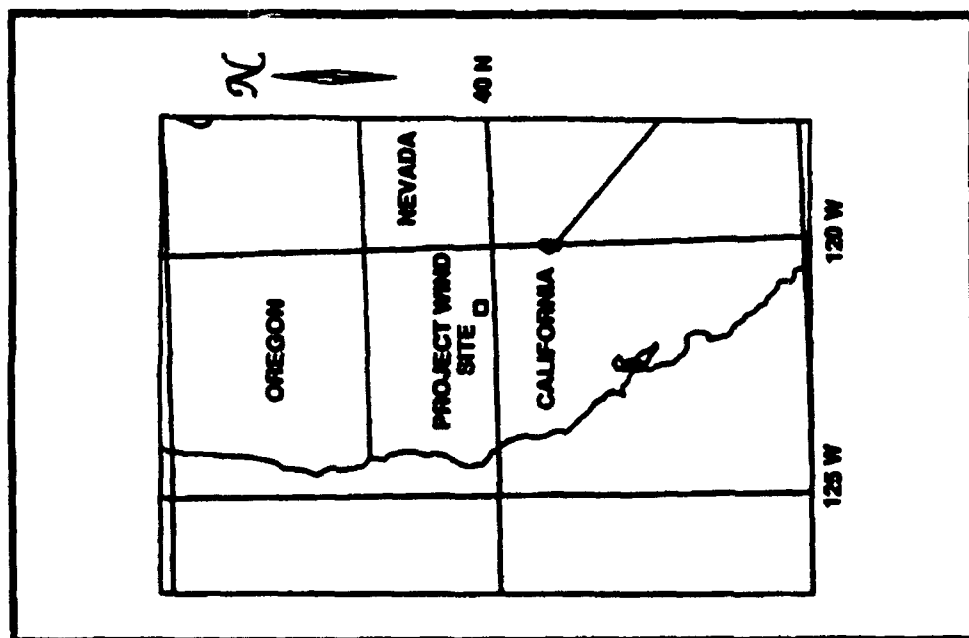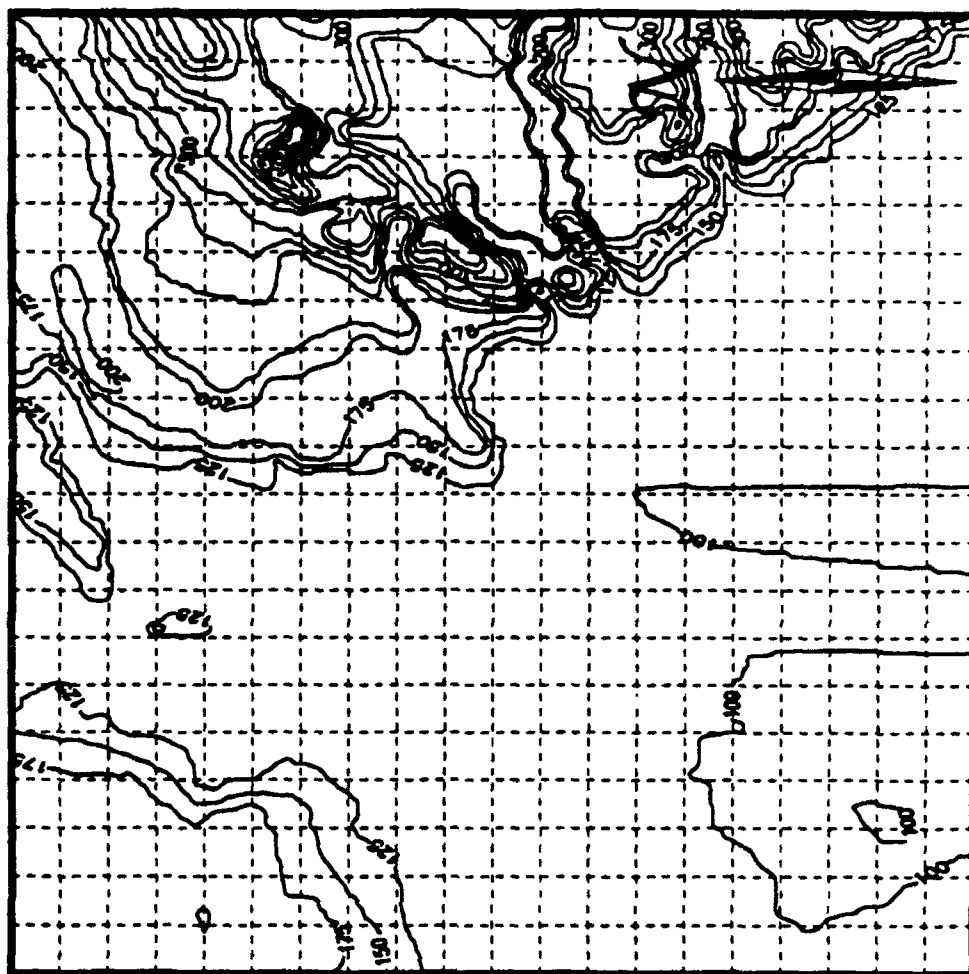
Figure 6. General location of the Project WIND site, marked by the small box in northeastern California (a); and a topographic map of the 20 X 20 km site area (b), where each grid cell represents a 1 X 1 km area, with a contour interval of 25 m.
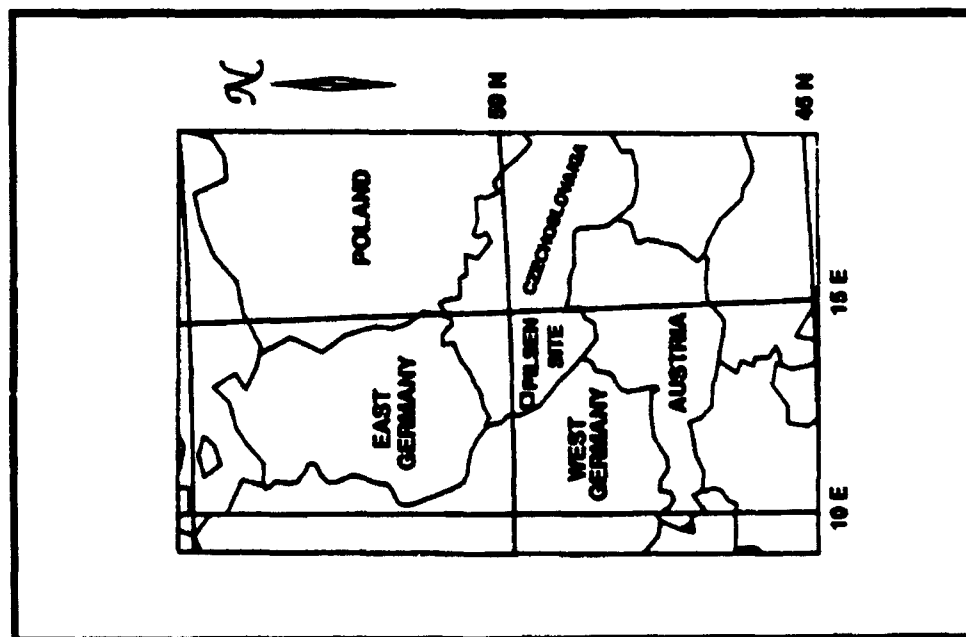
(a)
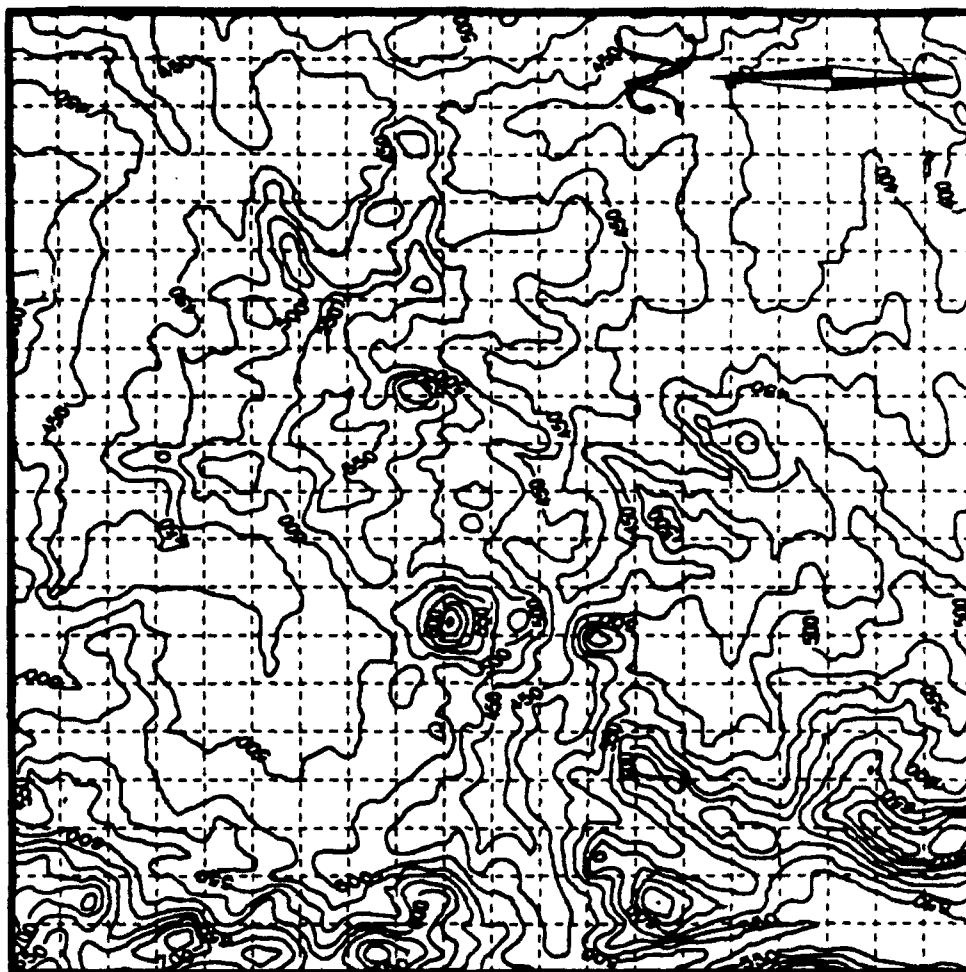
(b)

Figure 7. General location of the Czechoslovakian site, marked by the small box near the West German border (a); and a topographic map of the 20 X 20 km site area (b), each grid cell represents 1 X 1 km, with a 25 m contour interval.

Site 4 was selected, in contrast to the Project WIND site, as a remote, complex terrain area to test under sparse data conditions; no actual meteorological observation data was available for site 4 in this study. This exemplifies the circumstances under which the WOCSS model could be used for support purposes under extenuating field conditions.

Table 1. Approximate Latitude/Longitude of the southwest corner of the four selected 20 km × 20 km terrain sites.

Site No.	Site Name	Latitude	Longitude
1	WSMR, NM	32°19′ N	106°13′ W
2	NTC, CA	35°23′ N	116°39′ W
3	Project WIND, CA	40°8′ N	122°18′ W
4	Pilsen, Czech.	49°30′ N	12°40′ E

Digital terrain elevation - level 1 data (DTED) was acquired for sites 1-4 from the Defense Mapping Agency (DMA). The elevation data were relative to mean sea level (MSL), and for the purposes of this research work, only elevation data records were employed. DTED - level 1 elevation values are given in meters. The DTED data were provided in $1° \times 1°$ files that were identified by their southwest corner coordinates. The latitude/longitude, or $\Delta x, \Delta y$, grid spacing of DTED - level 1 elevation data is 3×3 arc seconds. Since there are $3600''$ in $1°$ of longitude or latitude and 111000 m $\approx 1°$ of latitude or longitude, both the $\Delta x, \Delta y$ interval is $\frac{3''}{3600''}(111000)$ m ≈ 92.50 m, which led to the establishment of 100 m as the highest resolution possible in the x, y terrain grid spaces.

One hundred-meter grid spacing is an unusually dense meteorological grid and will provide a degree of resolution in flow field simulations that has been difficult to attain in previous modeling work, basically due to hardware related computational limitations and meager availability of *mesoscale* meteorological data bases. Orlanski (1975) discussed several resolution planes, including 100 m, that can be used to identify gravity wave features[2] that can contribute significantly to ambient atmospheric properties, such as the degree of turbulence present at a particular location. Although the research work presented here is focused more on lateral, rather than on vertical gravity wave effects, the point is that 100-m grid spacing is expected to resolve meteorologically significant deviations (wavelengths $= \lambda$) in simulated flow fields.

Hansen and Flanigan (1989) developed a program to generate modified terrain elevation data in universal tranverse mercator coordinates from one to four $1°$ DTED-level 1 data cells, and this program was used to develop the 100-m grid systems, as well as two additional, gradually coarser, $\Delta x, \Delta y$ grids for use in this validation study (the selection was restricted to this number of cases because of time limitations).

The purpose in selecting more than one $\Delta x, \Delta y$ grid mesh was to examine the effect of varying grid spacing on the wind models' abilities to resolve terrain effects in their atmospheric flow structure solutions. Since the highest resolution limit was set by the DTED spacing format, the problem was to establish a reasonable low resolution $\Delta x, \Delta y$ limit, as well as an intermediate $\Delta x, \Delta y$ resolution. Several factors led to the selection of the low $\Delta x, \Delta y$ grid resolution limit.

---

[2]Hooke(1986) describes gravity waves as mesoscale, incompressible environment responses in the vertical. These features are coupled to the effects of local gravitational force and the degree of stable stratification in the local atmospheric column.

One of the primary factors in this selection was directly related to the 20.0 km × 20.0 km size of the terrain surfaces themselves. This lower limit, or coarse, resolution grid system should contain enough x, y data points to depict reasonable spatial averages of the associated wind flow field properties (Brown, 1991).

Smaller scale perturbations, u', induced by complex terrain in the basic flow field, u, would be of more interest at higher $\Delta x, \Delta y$ resolutions (Holton, 1979), such as at the $\Delta x = 100$-m resolution. Other factors leading to the selection of the coarse resolution grid spacing included a much more detailed consideration of perturbation properties in simulated flow structure solutions.

A minimum of 3 grid points are required to fully describe a complete sinusoidal wavelength feature (or perturbation); this is equivalent to a distance of $2\Delta x$, or $2\Delta y$ (see Fig. 9), and is referred to as the resolution limit, R, of an x, y grid (Riegel, 1974). R can be expressed as

$$R = \frac{\mu}{2\pi} sin(\frac{2\pi}{\mu}) \tag{1}$$

where $\mu = \frac{\lambda}{\Delta x}$. Here λ is the wavelength of the perturbation of interest, and Δx is the grid spacing in the x coordinate direction (Riegel, 1974).
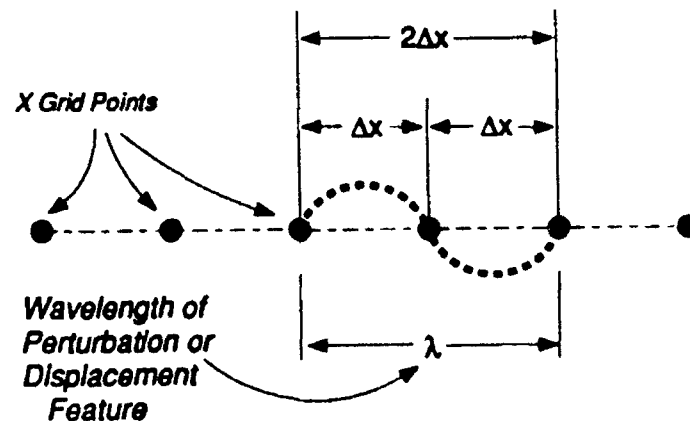
Figure 8. Minimum number of grid points required to resolve a displacement feature.

When $\lambda = 2\Delta x$, then $R = 0$, perturbation features with $\lambda < 2\Delta x$ will not be resolved by the grid. The error, in percent, that can be made by incorrectly phasing a perturbation $< \lambda$ through a grid can be expressed as $(1 - R) \cdot 100$.

Examination of elevated terrain features, on 1:250,000 scale maps, in the selected WSMR and NTC terrain areas revealed that significant terrain effects on atmospheric flow properties would probably begin to disappear at $\lambda \geq 2000$ m. A 2000 m λ represents 10% of the x or y linear limit (20 km). Since $2\Delta x$ is the perturbation resolution limit of a grid network, for a perturbation $\lambda = 2000$ m, Δx must ≤ 1000 m. Therefore, 1000 m was selected as the lowest resolution $\Delta x, \Delta y$ grid spacing.

Table 2. The $(1 - R) \cdot 100$ resolution limit error, in percent, that is possible in phasing perturbations $< \lambda$ through a grid with a given resolution of Δx.

Δx (meters)	perturbations $< \lambda$ (meters)					
	3000	2000	1000	500	250	100
3000	100	100	100	100	100	100
2000	100	100	100	100	100	100
1000	58.7	100	100	100	100	100
250	4.5	10.0	36.3	100	100	100
100	0.73	1.6	6.5	24.3	76.6	100

Note in Table 2 that for $\Delta x = 1000$ m, the resolution error (in percent) for all listed perturbations with a $\lambda < 2000$ m is always 100%, but at $\Delta x \leq 250$ m there are significant decreases in error as λ increases. For $\Delta x = 250$ m, error is only 10 % for $\lambda = 2000$ m and is futher reduced to less than 2% when $\Delta x = 100$ m. There are also other reasons to support the $\Delta x = 250$ m spacing other than the low 10% error threshold it has for $\lambda \leq 2000$ m.

Table 3 summarizes the basic properties of three 20 × 20 km grid systems with 1) 1000; 2) 250; and 3) 100 m $\Delta x, \Delta y$ grid point spacing, respectively. Note the exponential increase that occurs in the $\sum$ *of all points* column when $\Delta x, \Delta y$ spacing is changed from 1000, 250, and 100 m, respectively. This growth behavior is illustrated in Fig. 9(a). Figure 9(b) is a log-linear plot of the same information, but it is closer to a straight line trend – and, therefore, easier to describe. A straight linear projection, $y = mx + b$, from 100 to 1000 m produces a mean, intermediate spacing value of 550 m (see Fig. 9(c)), but a similar log-linear projection, $\log y = mx + b$, produces a mean, intermediate grid spacing value of 316.23 m (see Fig. 9(d)).

Table 3. The basic two dimensional grid properties of a 20 × 20 km area for Δx and Δy both, respectively, equal to 1000, 250, and 100 m.

Grid System	$\Delta x, \Delta y$	$x \times y$ points	$\sum$ of all points
1	1,000 m	21 × 21	441
2	250 m	81 × 81	6,561
3	100 m	201 × 201	40,401

The nearest multiple of the upper Δx spacing limit (1000 m) less than 316.23 m is 250 m. Reasons to select a multiple of 1000 m that is < 316.23 m include: 1) that it facilitates scaling of 1000 - 100 m Δx cross grid system results; and 2) Table 2 suggests the use of a smaller Δx to reduce error in λ resolution. Because of this, and the exponential nature of the $\sum$ *of all points* (see Table 3), $\Delta x = 250$ m was selected as the intermediate grid resolution. This final determination established the selected set of Δx resolutions (1000, 250, and 100 m) that were used in this study. Selection of this set of Δx spatial resolutions for use in this study required further precision to be employed in defining the meteorological scales of motion that would then be simulated by the WOCSS and OBWIND models.
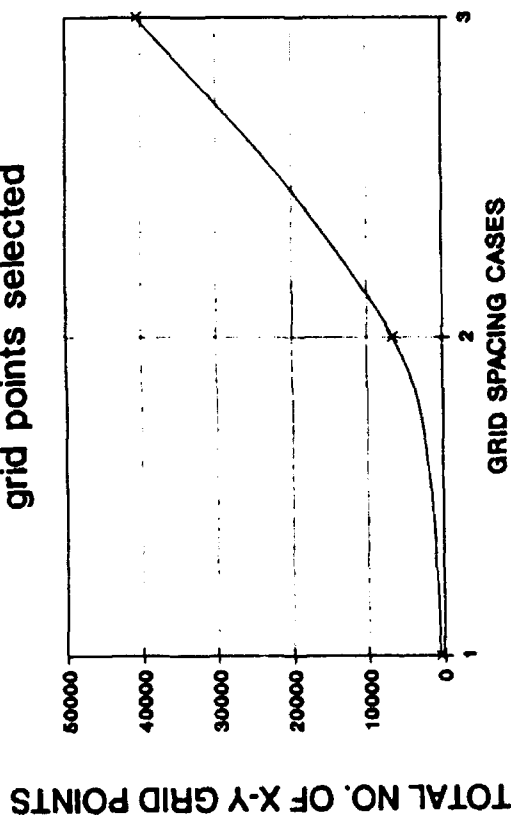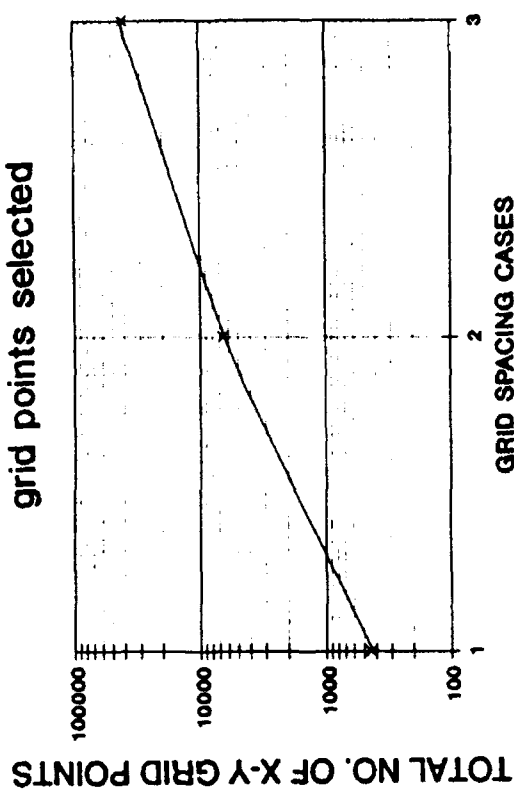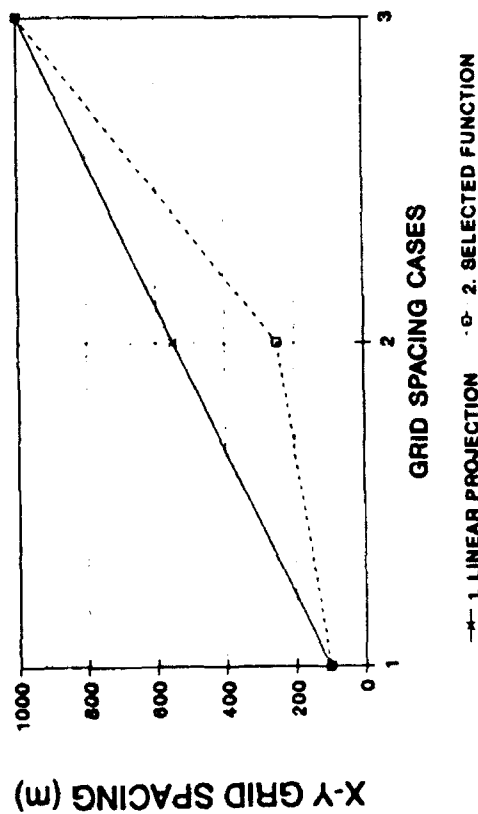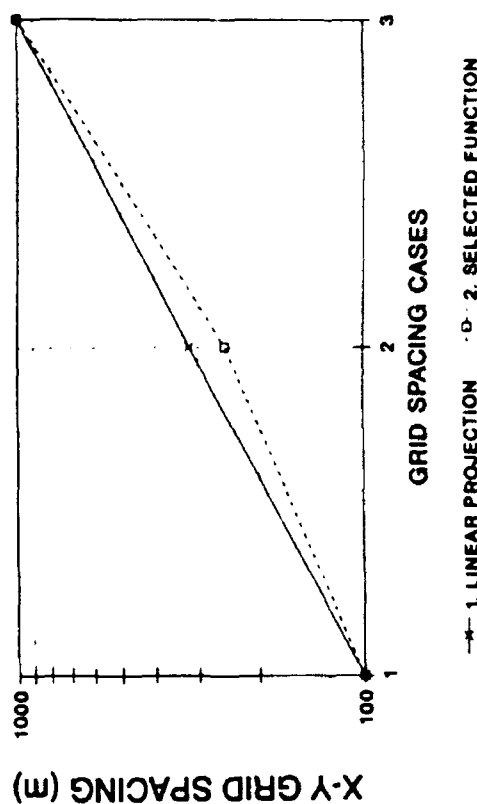
Figure 9. Exponential Behavior of grid point totals in linear (a) and log-linear (b) scales, as well as the contrast of the linear geometric mean of 550 (c), and the exponential mean of 316.23 (d), with respect to 250 m grid resolution.

Because the coarse, $\Delta x = 1000$ m, grid was established to resolve $\lambda \geq 2,000$ m, it qualifies as a mesoscale mesh (Pielke, 1984). However, Table 4 implies that the remaining two grid structures ($\Delta x = 250$, and 100 m) fall into a different scale – the microscale. All three selected Δx grid systems can be more precisely defined from the information provided in Table 4. For example, the $\Delta x = 1000$ m grid can be classified as a *meso* γ network, because its λ resolution limit is $2\Delta x = 2$ km. Similarly, the $\Delta x = 250$ and 100 m grids have the potential to resolve *micro* α scale systems, because their λ resolution limits are, respectively, 500 and 200 m.

Table 4. Selected meteorological spatial (Δx) scale definitions. [3]

Meteorological Scales	λ		
Macro α	$\lambda > 10,000$ km		
Macro β	2,000 km	$< \lambda \leq$	10,000 km
Meso α	200 km	$< \lambda \leq$	2,000 km
Meso β	20 km	$< \lambda \leq$	200 km
Meso γ	2 km	$< \lambda \leq$	20 km
Micro α	200 m	$< \lambda \leq$	2 km
Micro β	20 m	$< \lambda \leq$	200 m
Micro γ	$\lambda < 20$ m		

Table 5 lists statistics that further characterize the four terrain sites selected for use in this study. These terrain properties, even though they are extremely significant, are not really results themselves; but they establish the context within which to interpret the wind model test results. The percentage change between 250 - 100 m Δx elevation data bases were not significant, but some 1000 - 100 m changes were noteworthy; therefore, they were selected for inclusion in Table 5.

---

[3]Orlanski (1975).

The percentage change between all the 1000 - 100 m elevation data mean elevations was insignificant (less than 1%) and almost normally distributed (see Table 5). Minimum elevations and distribution frequencies, inferred from the ± 1.0 standard deviation comparisons, were also fairly stable between 1000 - 100 m (less than 1% and 3%, respectively). Both the mean elevation and the ± 1.0 standard deviation, at 100, 250, and 1000 m Δx grid spacing, for all the terrain data bases are illustrated in Fig. 10. Therefore, variation in grid spacing selection between 100 - 1000 m appears to have little relative effect in changing each site's mean elevation and distribution variance. The behavior of each site's mean elevation value and distribution behavior, therefore, appears stable, in relative terms, when the grid spacing is changed (see Fig. 10).

Table 5. Variations in the terrain elevation data bases (m above MSL), as a function of grid spacing, Δx (m), for the listed sites: 1) WSMR; 2) NTC; 3) Project WIND; and 4) Czechoslovakia. The variations are presented in terms of the 1000 m - 100 m Δx differences. These differences are then expressed as percentage change between the 1000 m - 100 m Δx terrain data bases.

SITE	Δx	Terrain Statistics (including 1000-100m Δ %)						
		MEAN		MIN		MAX		STD. DEV.	
1	1000	1266.21		1219.00		1570.00		47.09	
	100	1268.00	.1%	1218.00	-.1%	1588.00	1.2%	45.81	-2.7%
2	1000	1036.84		678.00		1511.00		175.59	
	100	1043.81	.7%	677.00	-.2%	1605.00	6.2%	172.57	-1.7%
3	1000	161.84		83.00		420.00		69.56	
	100	160.68	-.7%	83.00	0%	552.00	31.4%	68.95	-0.9%
4	1000	490.48		377.00		746.00		67.48	
	100	488.57	-.4%	374.00	-.8%	747.00	0.1%	65.76	-2.6%
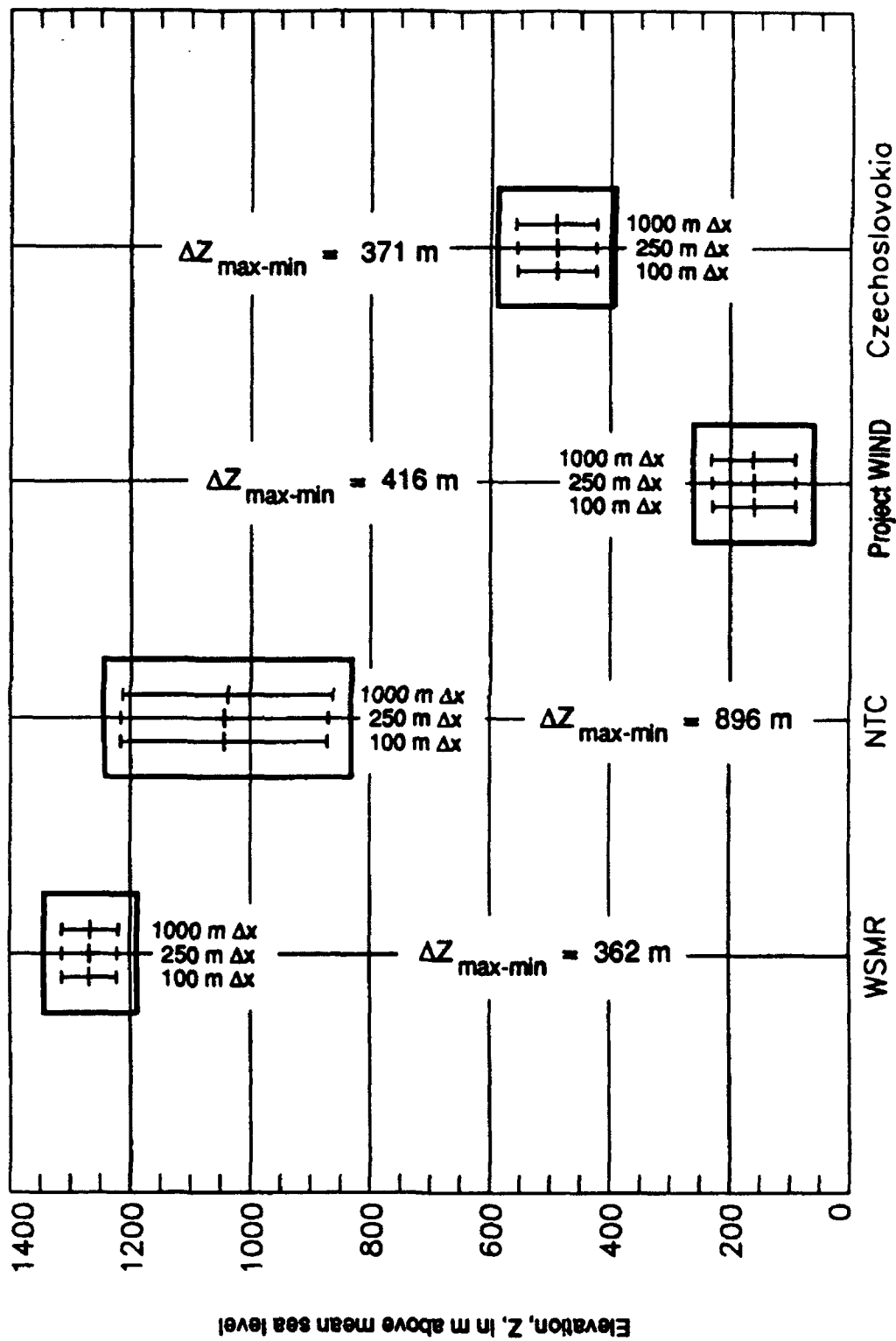
Figure 10. The mean and first standard deviation of each terrain data set for each site included in this study. Extreme ranges in elevation (Δz) are also listed.

21

However, comparisons of maximum elevation data revealed that maximum elevations could change as much as $+$ 31 % (Table 5, for the Project WIND site) when Δx grid resolution improved by a factor of $\times$ 10 (e.g., the 1000 - 100 m comparison); this results from the "smoothing" effect that occurs at lower resolutions. Figures 11-14 illustrate this "smoothing" effect when Δx resolution is decreased from 250 m to 1000 m for the WSMR, NTC, Project WIND, and Czechoslovakian DTED bases. The "smoothing" process detects fewer extreme elevation points, and this detection failure is not consistent - it depends on how the grid mesh is registered to a terrain surface and will also vary significantly between different terrain surfaces. From Figs. 11-14 it is evident that careful Δx selection, for the purposes of studying complex terrain effects, is critical. Note that the NTC site has the greatest variability and range in elevation, while the WSMR site elevation has the smallest extremes and variability. Also, the distribution of elevation data for the Project WIND Site produces standard deviations closely resembling those of the Czechoslovakian Site (see Table 5). The influence of these Δx grid variations on the WOCSS model will be discussed in the Results section.

2.2   Meteorological Data Bases

Project WIND was a cooperative field study designed to collect comprehensive meteorological data over complex terrain for meteorological model evaluation and improvement purposes (Cionco, 1989). Project WIND was designed to address mesoscale and microscale meteorological domains (see Table 4). The meteorological data collected during Project WIND included measurements of wind speed and direction, turbulence, temperature, humidy, pressure, solar radiation, soil heat flux, precipitation, upper air soundings, and satellite images. Observation sites were scattered over a 200 km $\times$ 200 km domain centered on the western slopes of the Sierra Nevada Mountains and along the eastern skirt of the Sacramento Valley, between Sacramento and Redding, California.
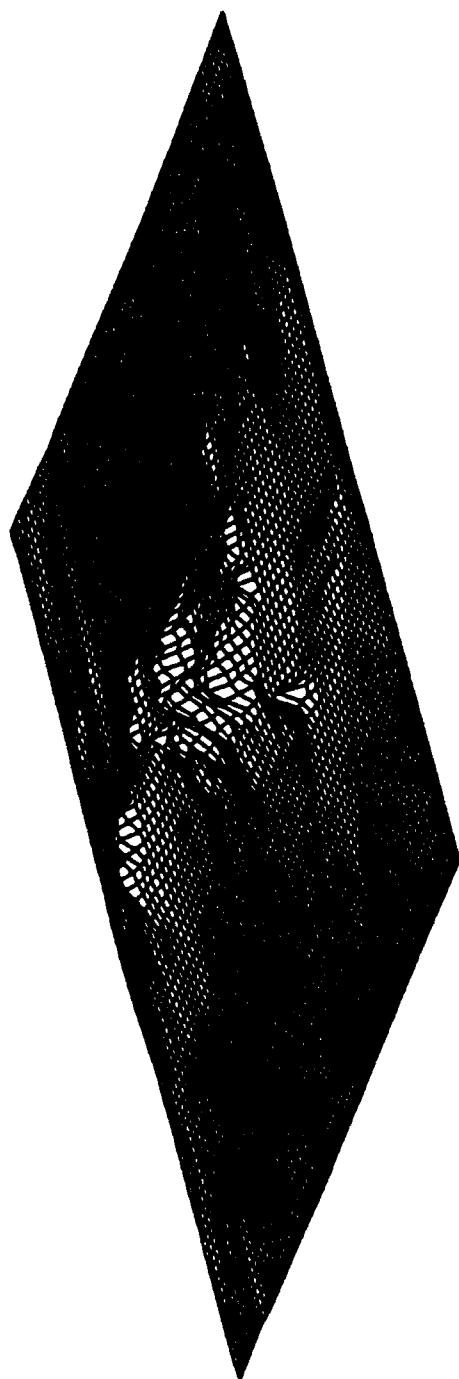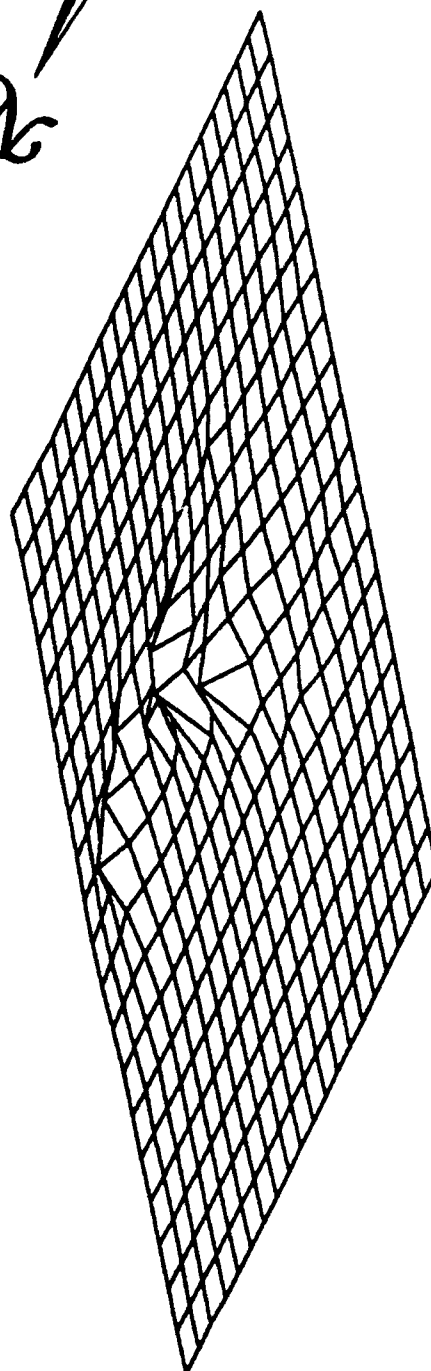
Figure 11. Illustrating the effect of varying the WSMR site DTED grid spacing from 250 m (a) to 1000 m (b).

23

(a)

(b)
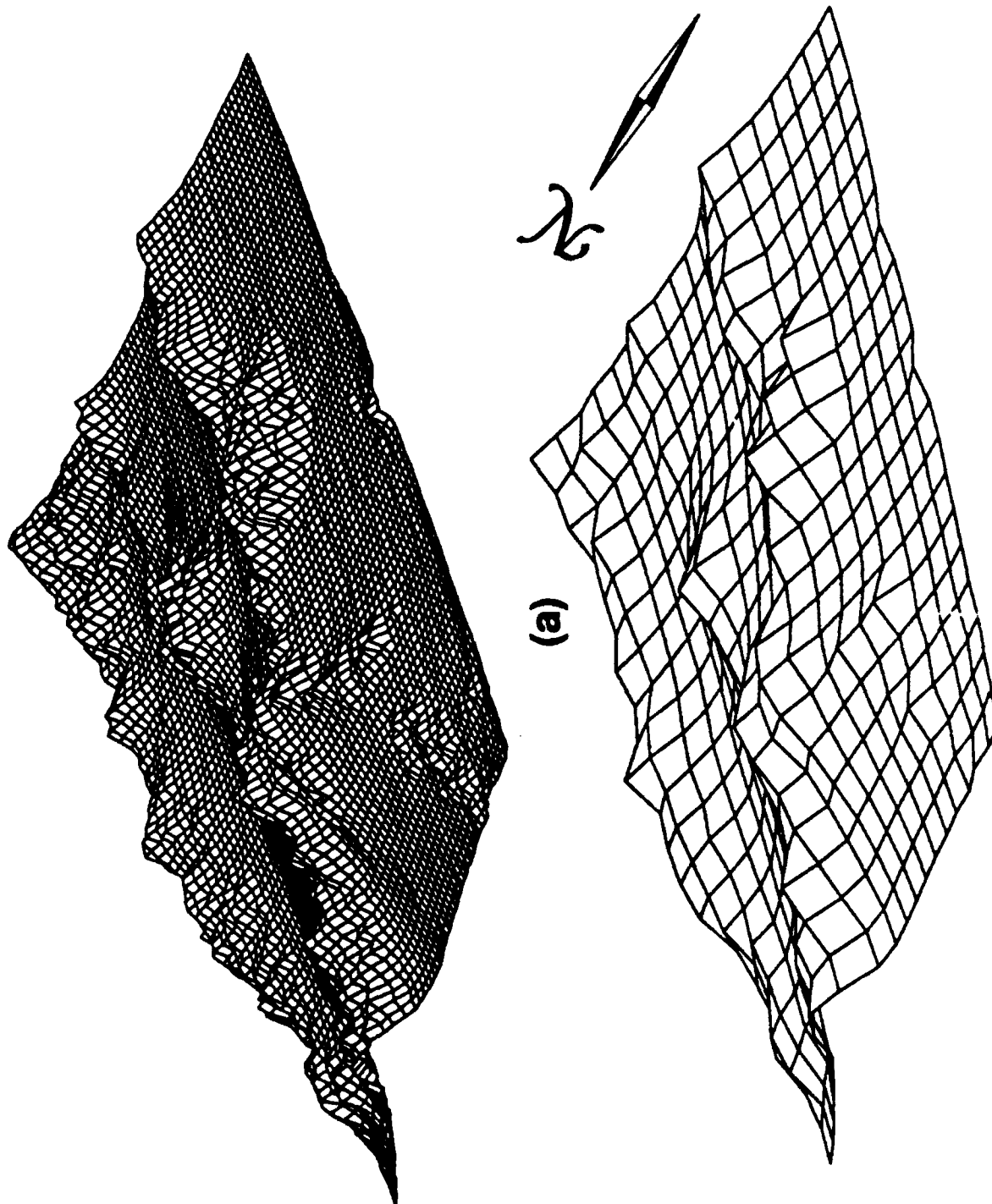
Figure 12. Illustrating the effect of varying the NTC site DTED grid spacing from 250 m (a) to 1000 m (b).

24

(a)

(b)
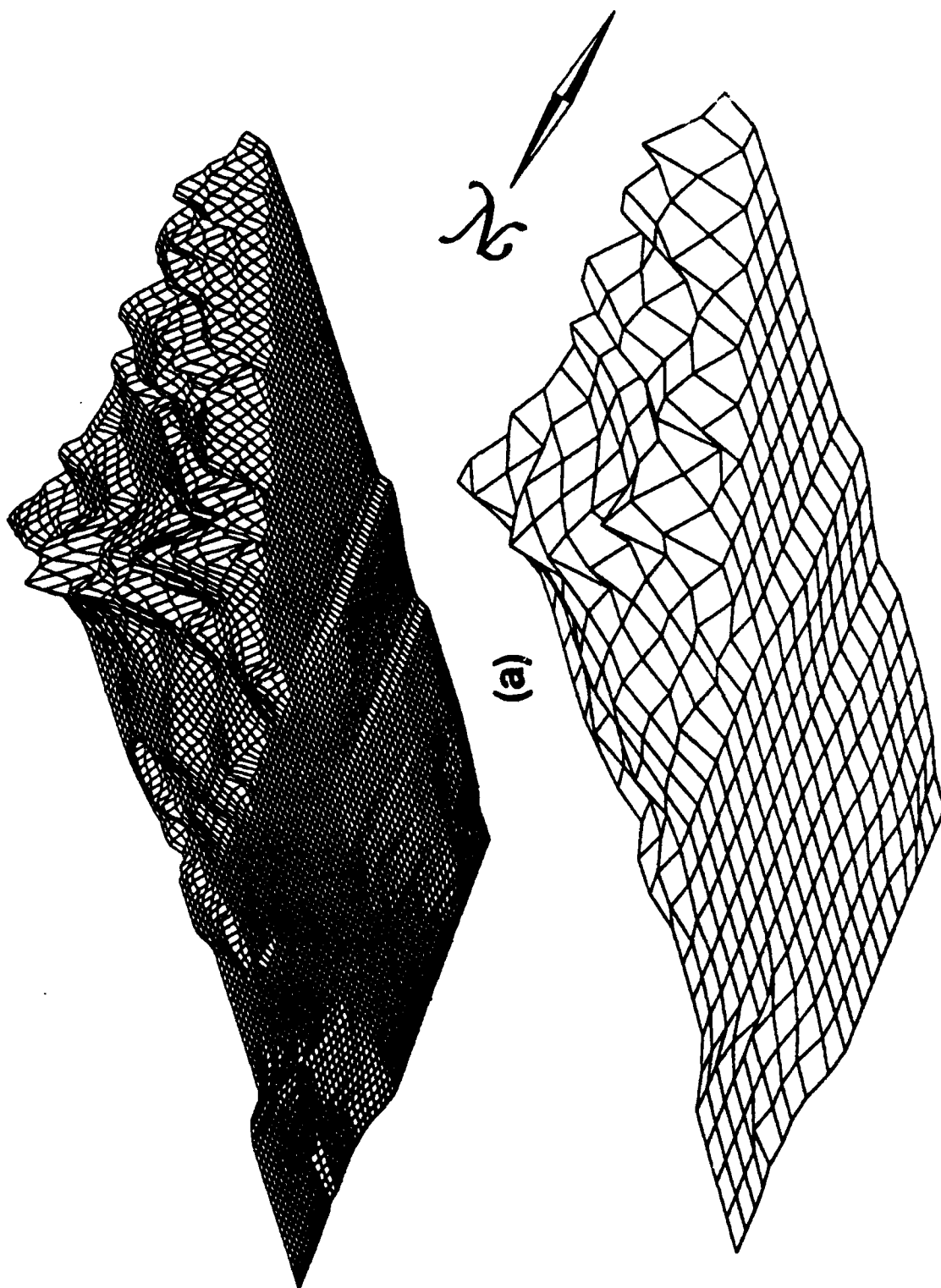
Figure 13. Illustrating the effect of varying the Project WIND site DTED grid spacing from 250 m (a) to 1000 m (b).

(a)

(b)
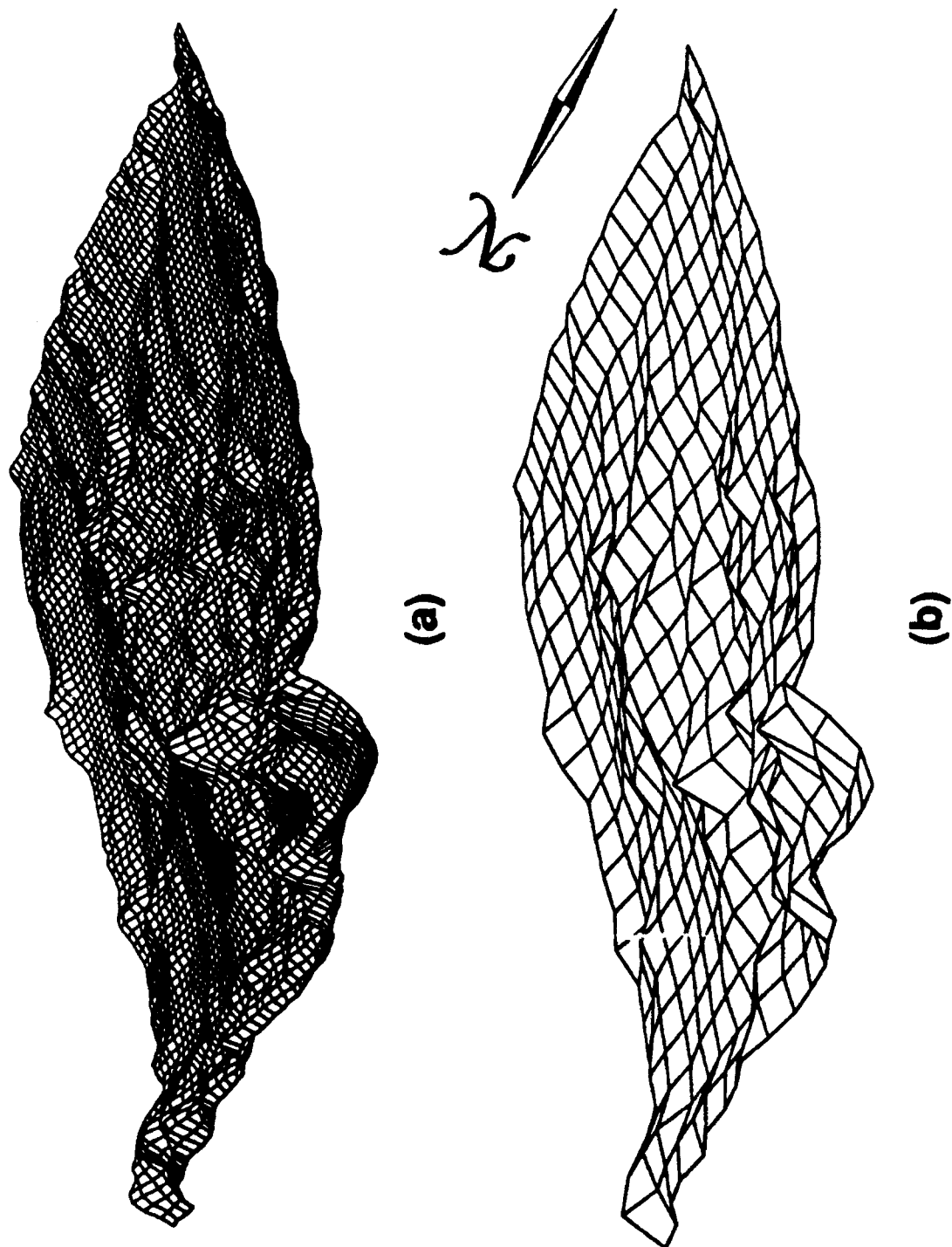
Figure 14. Illustrating the effect of varying the Czechoslovakian site DTED grid spacing from 250 m (a) to 1000 m (b).

For this research work, *meso γ* - *micro α* data was chosen from the Project WIND data base. These data was collected in the vicinity of Red Bluff, California (see Fig. 6). The data included wind speed and direction observations taken from sensors 10 m above the ground at 6 different sites (S5-S10); an upper air sounding was also taken every two hours at site S8. Samples of Project WIND surface and upper air data profiles used in this study are illustrated in Appendix A.

The surface and upper air data for the WSMR and NTC were similar in nature to the Project WIND data, except that they were not reported at the same frequency as in Project WIND and in some cases had to be estimated. The WSMR data were more in the *micro α* regime, and the NTC data were representative of *meso γ* domains. WSMR and NTC meteorological data are also described in more detail in Appendix A.

The sparse data scenario, for the terrain near Pilsen, Czechoslovakia, did not include field observation data. Instead, theoretical meteorological initialization data was developed to simulate remote, unsupported field exercise situations. For example, a single, user specified, 10 m surface wind speed and direction was coupled to an estimated upper air wind profile that was derived from a logarithmic velocity profile (Arya, 1988)

$$U = u^* \frac{1}{k} \ln \frac{z}{z_0} \qquad (2)$$

where U is the mean horizontal wind speed as a function of friction velocity, u^*, von Karman's constant, k, the roughness parameter, z_0, and height above a surface, z. The friction velocity term is defined as $u^* \equiv \sqrt{\frac{\tau_0}{\rho}}$, where τ_0 is surface shear stress, and ρ is the fluid density. More details on this sparse data initialization scheme for Pilsen, Czechoslovakia are located in Appendix A.

2.3 The WOCSS Model

The WOCSS model's approximations of wind velocity fields combines selected dynamic and kinematic fluid flow considerations. Kinematics centers on the development of solutions to flow problems without considering the actual forces at work (Hess, 1979), while dynamic meteorology considers a broader spectrum of problems, including the fluxes and conversions of mechanical, as well as thermal energy, and equilibrium states of the atmosphere (Riegel, 1974).

A fundamental kinematic design features in the WOCSS model address initial flow modeling problems such as mass consistency and nondivergence. For example, the WOCSS model assumes that flow takes place within the bounds of specified surfaces. These surfaces are somewhat different from *sigma* surfaces, which are solved for using the following equation (Pielke, 1984):

$$\sigma = s \frac{(z - z_G)}{(s - z_G)} \tag{3}$$

where σ is the normalized terrain following layer being solved for, s specifies the upper flow boundary height, z is the layer elevation above the terrain, and z_G is the terrain height above MSL. In the WOCSS model, wherever a flow surface intersects the terrain, wind velocity is set to zero (because the flow field cannot pass into the terrain obstacle), and mass conservation theoretically forces flow around the intersection with terrain.

The WOCSS coordinate system, therefore, is a flow-following, not a terrain-following system. A major assumption in the WOCSS flow-following system is that there are no perpendicular components of flow to the bounding flow layer surfaces (Ludwig and Endlich, 1988). These flow bounding, or critical streamline,

surfaces can be solved for using a variation of the following equation:

$$(z_{max} - z_o)_{flow\ layer\ n} = V_o \left\{ \frac{g}{T_o} \frac{\partial \theta}{\partial z_o} \right\}^{-1/2} \tag{4}$$

where z_{max} is the highest altitude limit of flow in layer n, z_o is the lowest altitude of the same flow layer, V_o is the mean flow velocity along the z_o surface, g is the acceleration due to gravity, T_o is the mean temperature along z_o, and $\frac{\partial \theta}{\partial z_o}$ is the vertical potential temperature gradient. Nondivergence is forced on all n flow layers by the following continuity equation approximation

$$\frac{\partial u_*}{\partial x} + \frac{\partial v_*}{\partial y} = 0 \tag{5}$$

where $u_* = u \Delta z$, and $v_* = v \Delta z$. The u_* and v_* terms are flux-related variables, where Δz is the average separation between z_o and z_{max}, the u term is the wind velocity component in the x-axis direction, and v is the wind velocity component along the y-axis direction.

Initial testing of the WOCSS model involved exercising default parameters in model subroutines. These sensitivity studies centered on identifying parameter settings that optimize the WOCSS's dynamic design feature (e.g., the ability to solve for lateral forcing effects). Therefore, this work concentrated largely on the subroutines that establish the relationship governing critical streamline height,

$$\frac{1}{2} U_c^2 = \frac{g}{\overline{T}} \int_{H_c}^{Z} (Z - z) \frac{\partial \theta}{\partial z} dz \tag{6}$$

where kinetic flow energy per unit mass is solved for on the left side, and potential flow energy per unit mass is solved for on the right side of the equation. U_c is the flow velocity at the critical streamline height, g is the acceleration due to gravity, $\overline{T}$ is the mean temperature (in °K) of the layer considered, Z is the height of the topographic obstacle, H_c is the height of the critical streamline, z is the height that air is lifted to in the layer, and $\frac{\partial \theta}{\partial z}$ is the vertical potential temperature gradient (Ludwig and Endlich, 1988).

2.4 The OBWIND Model

OBWIND is a basic three-dimensional, kinematic wind model (Henmi and Tabor, 1988), and does not consider dynamic, lateral forcing effects in its solutions to flow field approximations. It incorporates a terrain following σ type flow coordinate system. This model interpolates surface wind initialization data using the following equation:

$$U(i,j,1) = \sum_{m=1}^{n} \psi_m(r)U_m / \sum_{m=1}^{n} \psi_m(r) \qquad (7)$$

where $U(i,j,1)$ is the calculated value at the grid point $(i,j,1)$, U_m is the observed wind at site m, $\psi_m(r)$ is $\frac{1}{r^2}$, and r is the grid point to observation site distance. Upper level winds are interpolated using a similar equation:

$$U(i,j,k) = \frac{\sum_m \sum_n \psi_m(r) \cdot \psi_n(z)U_{m,n}}{\sum_m \sum_n \psi_m(r) \cdot \psi_n(z)} \qquad (8)$$

where $\psi_n(z)$ is the vertical weighting function, and z is the vertical distance between the radiosonde sounding point and layer k. The main attribute of this model is its mass consistency adjustment scheme, which closely resembles the approach taken by Endlich (1967). Endlich's method is based on several linear partial differential equations. The equation of central importance to Henmi's model is:

$$\frac{\partial u}{\partial x} + \frac{\partial v}{\partial y} = \phi(i,j) \qquad (9)$$

where u is the west-east wind component, v is the south-north wind component, and $\phi(i,j)$ is the divergence at each grid point. Divergence is iteratively reduced to a predefined threshold, which imposes mass consistency in the flow field.

2.5 Case Studies

Since the primary focus of this research work was centered on the WOCSS model, validation of the OBWIND model was not addressed. Henmi's OBWIND model was used strictly to develop a relative measure of the improvement that the WOCSS model contributes in simulating lateral transfer processes in wind flow fields.

To establish this comparison, the WOCSS model and the OBWIND model were run with exactly the same meteorological and terrain data for WSMR, NTC, Project WIND, and Czechoslovakia), at three different $\Delta x, \Delta y$ grid spacings (100, 250, and 1000 m). This comparison of the WOCSS and OBWIND models included selected measurements of execution times under equivalent initialization conditions. The WOCSS model was also tested against its own ability to resolve lateral transfer via a series of runs with each meteorological data set where observation initialization data was selectively restricted.

The terrain grid spacing selection scheme had a significant influence on the selection of vertical layers examined in this research work. The $\Delta x, \Delta y$ spacing scheme was used to establish similiarity in the vertical scales examined in this study; three elevated velocity field surfaces were produced in each wind model run 1) the lowest layer was coincident with the 10 m surface meteorological wind velocity observations; 2) the second layer, established at 25 m AGL, was a factor 2.5 × the first layer's elevation AGL (e.g., proportional to the 100-m to the 250 m grid space resolution change); and 3) the third layer was selected at a factor of 10 × the first layer, which meant the final layer was 100 m AGL (proportional to the 100-1000 m change in grid space resolution).

Two meteorological conditions, stable and unstable cases, were selected for each terrain site. Criteria used to select this data are discussed in Appendix A. This meteorological data, the terrain data bases, the WOCSS model, and the OBWIND model were then installed in a structured file directory system (see Fig. 15) on a Sun Microsystems SPARCstation IPC computer workstation, and Fig. 16 summarizes the plan for the case studies that were carried out using the OBWIND and WOCSS models.
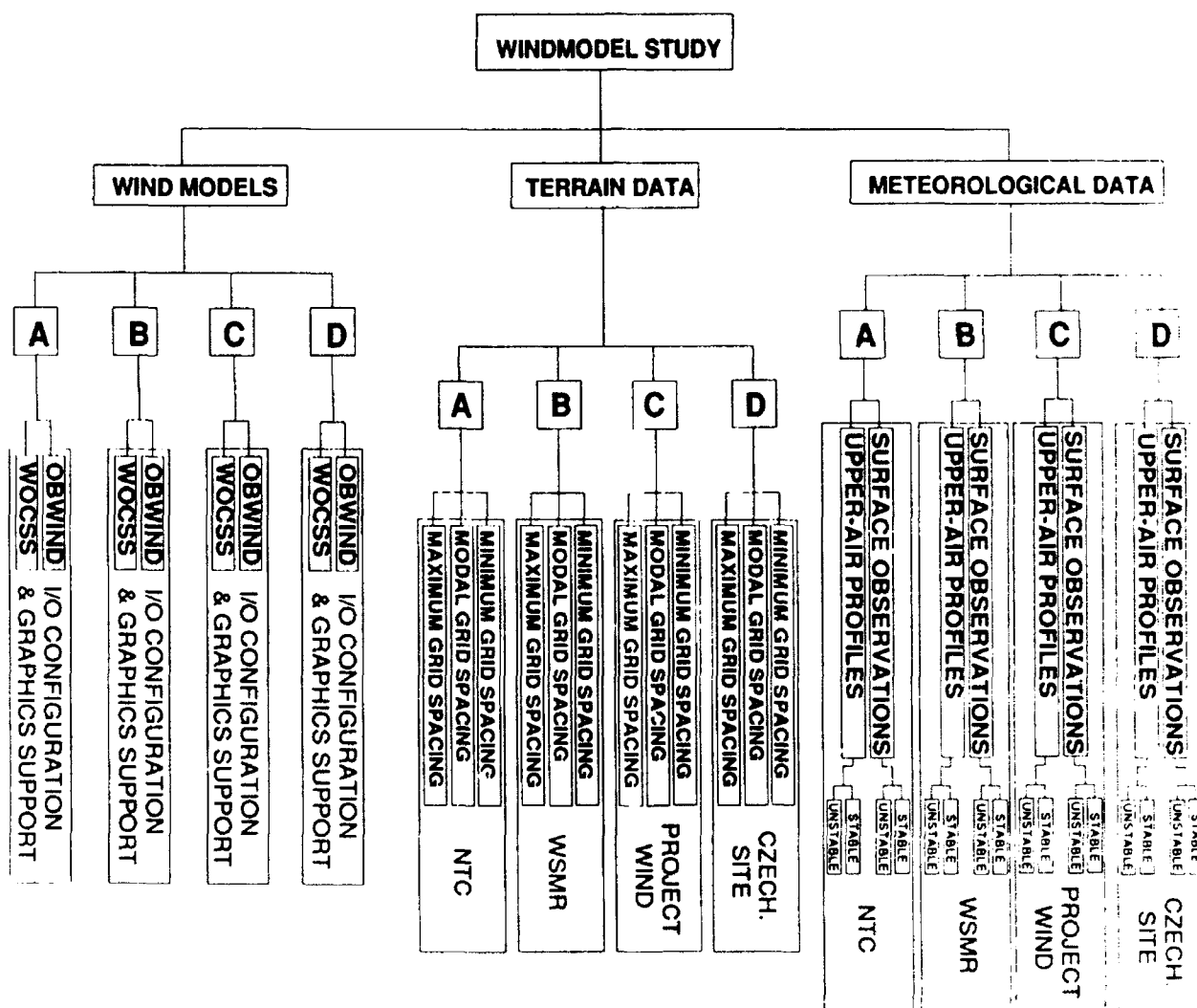
Figure 15. Mapping of the file directory scheme used to organize the research work in a manner that prevented the possibility of overlapping or contaminating individual sets of model results.

32
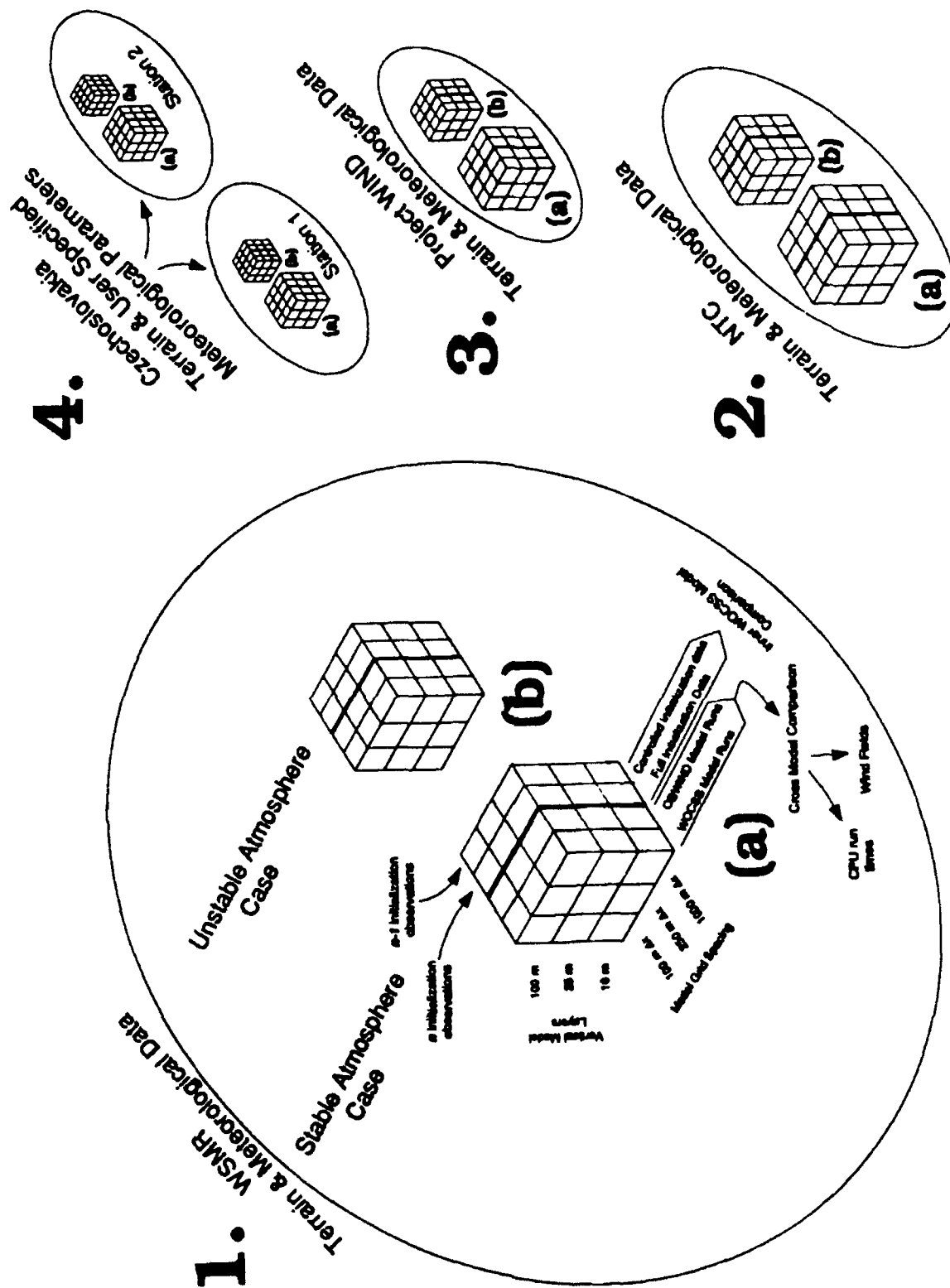
Figure 16. Overview of the detail involved in the implementation of individual case studies for sites 1-4, considering both stable (a) and unstable (b) atmospheric conditions.

2.6 Analysis Techniques

Tucker and Henmi (1990) reported that basic mass conserving, diagnostic models did not produce significantly better agreement with actual observation data than a simple interpolation of wind field data. As a result, the OBWIND model, which is a basic mass conserving model, was selected for use in this study as the base case test platform with which to compare WOCSS model results; the validity of the WOCSS model's ability to infer the effect of lateral mechanical forcing would be measured in terms of its comparison to the basic mass conserving OBWIND model, which does not consider the effects of topography on flow field distribution. Therefore, detailed, statistical comparisons of the WOCSS and OBWIND outputs had to carried out.

For example, the standard deviations of WOCSS **u** and **v** vector components, σ_m, were calculated using

$$\sigma_m = \left\{ \sum_i [W_m(i) - \overline{W}_m]^2 / n \right\}^{1/2} \tag{10}$$

where $W_m(k)$ is the value produced by the WOCSS model at point k (Henmi and Tabor, 1990). Then σ_m quantities were compared to the standard deviation of OBWIND values, σ_o, which are calculated using

$$\sigma_o = \left\{ \sum_i [W_o(i) - \overline{W}_o]^2 / n \right\}^{1/2} \tag{11}$$

where $W_o(k)$ is an OBWIND model value at point k.

Willmott et al.(1985) and Steyn and McKendry (1988) presented several statistical model evaluation measures – such as the root-mean-squared difference

(RMSD) and the index of agreement – which were also incorporated into the analysis of WOCSS and OBWIND model results. The root-mean-squared difference can be expressed as

$$RMSD = \sqrt{\frac{1}{n}\sum^{n}(W_m(i) - W_o(i))^2}$$ (12)

where n is the number of gridpoints, W_m and W_o are, respectively, the WOCSS case and OBWIND case values.

The index of agreement, d, is defined as:

$$d = 1 - \left[n(RMSD)^2 / \sum_{1}^{n}(|P_i'| + |O_i'|)^2\right]$$ (13)

where $P_i' = W_m(i) - \overline{W_o}$ and $O_i' = W_o(i) - \overline{W_o}$, with $\overline{W_o}$ being the mean OBWIND case value.

According to Steyn and McKendry (1988), this index of agreement, d, has a possible range between 1.0 (for 100 % agreement) to 0.0 (for 0 % agreement), thereby providing an objective, critical comparison measure. A computer program that implemented this agreement index test, as well as the other statistical tests discussed above, was developed and employed to automate the processing of all OBWIND-WOCSS model comparisons (Appendix B provides a descriptive outline of this computer program).

To obtain further measures of statistical significance of the study results, correlation coefficients, r, of WOCSS and OBWIND layer data were calculated using

$$r = \frac{\frac{1}{n}\sum_{i=1}^{n}(W_m(i) - \overline{W_m})(W_o(i) - \overline{W_o})}{\sqrt{\frac{1}{n}\sum_{i=1}^{n}(W_m(i) - \overline{W_m})^2} \cdot \sqrt{\frac{1}{n}\sum_{i=1}^{n}(W_o(i) - \overline{W_o})^2}}$$ (14)

where $W_m(n)$ and $W_m(n)$ are the respective WOCSS and OBWIND data u and v components being tested over the number of data elements in each set (containing n elements), and $\overline{W_m}$ and $\overline{W_o}$ are the respective means of the data sets being compared. This method was also used to study the WOCSS model's correlation with terrain elevation.

35

3 RESULTS

The WOCSS model was configured for use in this study, and all OBWIND and WOCSS model runs were executed and selectively analyzed (see Section 2.5). Appendix C provides a summary of technical details related to OBWIND and WOCSS software execution. The WSMR site terrain is fairly symmetric when compared to the other 3 selected sites, which facilitates preliminary interpretation of study results. Therefore, the most detailed discussion of study results focuses on the WSMR model runs; in particular, the stable case comparisons were the most interesting in terms of dynamic effects associated with terrain-atmosphere interaction predicted by the WOCSS model.

3.1 WSMR Results

3.1.1 WOCSS Model Configuration

As noted earlier, the WOCSS model first had to be properly configured before it could be executed, and an important detail of this configuration stage involved establishing the shape of the top flow layer boundary. The shape of this boundary can be modified by a Slope Factor (SLFAC) term in the WOCSS source code. Figure 17 illustrates a variety of SLFAC configurations, each of which was implemented in the WOCSS model (results from the WSMR stable 25 m AGL flow surface are summarized in Table 6).

The compressed boundary layer slope factor in Fig. 17 introduces a variable degree of resistance to vertical displacement as a function of terrain elevation, while the restricted boundary layer slope factor in Fig. 17 severely restricts vertical flow layer displacement (indicative of extremely stable conditions). Conversely, the relaxed boundary layer slope factor in Fig. 17 illustrates a condition in which there is no resistance to flow surface vertical displacement as a function of terrain elevation (more characteristic of neutral-unstable boundary layer conditions).
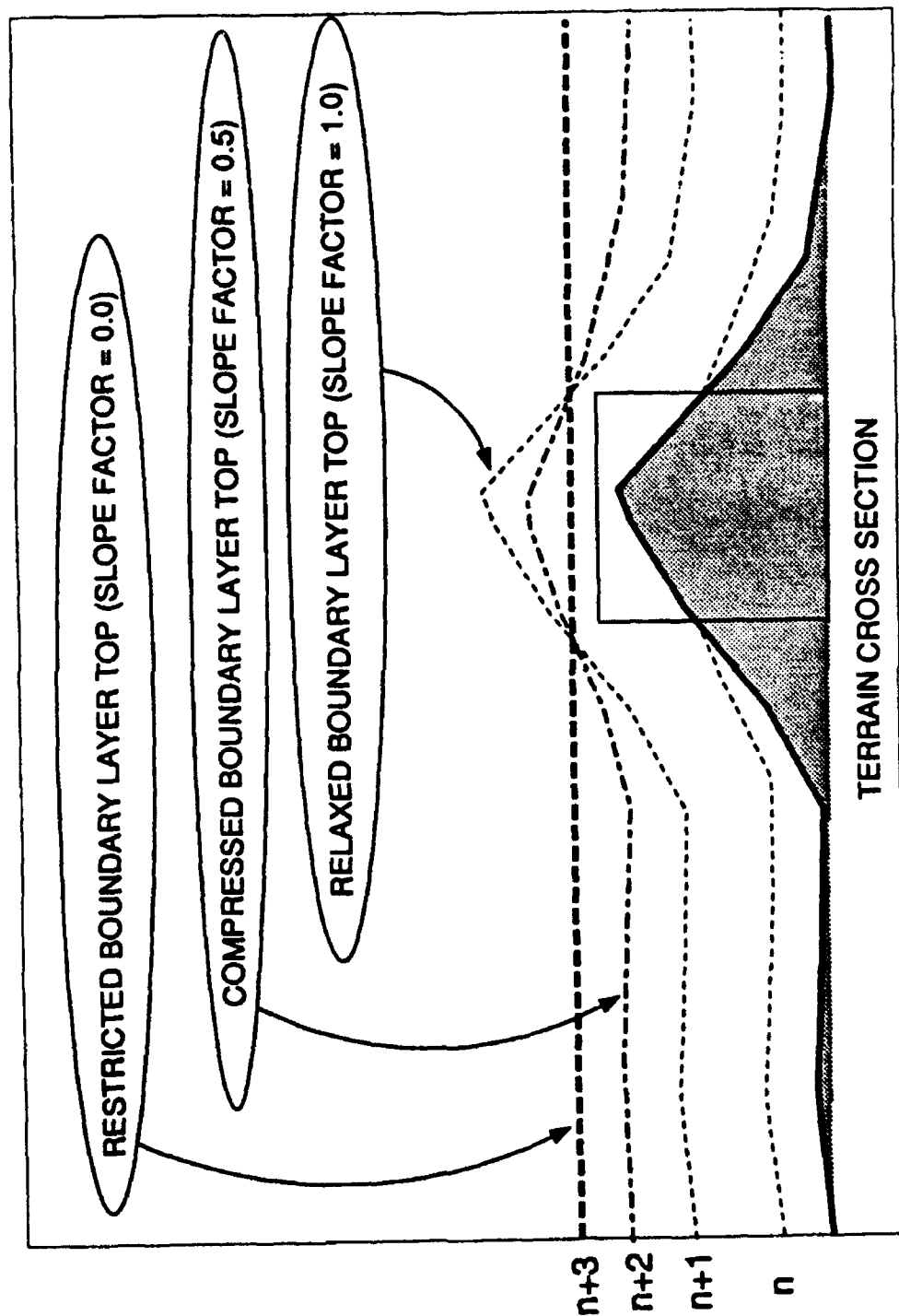
Figure 17. Vertical 2-d terrain cross-section illustrating variations in the slope of the boundary layer top that were examined when the WOCSS model was configured for use in this study. Flow restricted space for a lower layer, n, is boxed in (where surface n intersects the terrain - see Fig. 18).

Note in Fig. 17 that flow surfaces below the boundary top can intersect terrain (e.g., layer n), where kinetic flow energy is predicted to be insufficient in overcoming local terrain impediments along the z axis. Figure 18 illustrates the flow restricted space that results when a flow layer surface intersects the underlying terrain. The WOCSS model assigns zero wind speeds to all grid points in flow restricted spaces, which then requires the WOCSS mass conservation algorithm to force flow mass, on each modeled flow layer, around intersections with flow restricted spaces. WOCSS wind speeds are set to zero in flow restricted spaces because flow in the vicinity of flow restricted spaces is predicted to have insufficient kinetic energy to overcome the terrain obstacle in question.

In Table 6, the difference in flow restricted space between the relaxed (layer n+1 in Fig. 17) and compressed (layer n+2 in Fig. 17) slope factor in WOCSS model 25 m layer runs is equivalent to a $2.05 \times 2.05 \ km^2$ area, and the difference between the compressed and restricted slope (layer n+3 in Fig. 17) model runs is equivalent to a $2.96 \times 2.96 \ km^2$ area. The reduction in predicted flow restricted space at 25 m between compressed slope runs, after being re-initialized with wind speed data increased by a factor of 2×, is equivalent to a $3.07 \times 3.07 \ km^2$ area.

The differences in flow restricted space described in the previous paragraph are all noteworthy, especially in terms of urban scale problems, and the differences are reasonably consistent with the conditions that produced them. For example, as the slope of the boundary layer top became more restricted, the amount of restricted flow space decreased, because Bernoulli speed-up effects in the more compressed flow layers produced increases in available kinetic energy, improving local flow potential to overcome terrain obstacles; this also explains the resulting decrease in flow restricted space when the magnitude of wind speed used to initialize the WOCSS model was doubled.
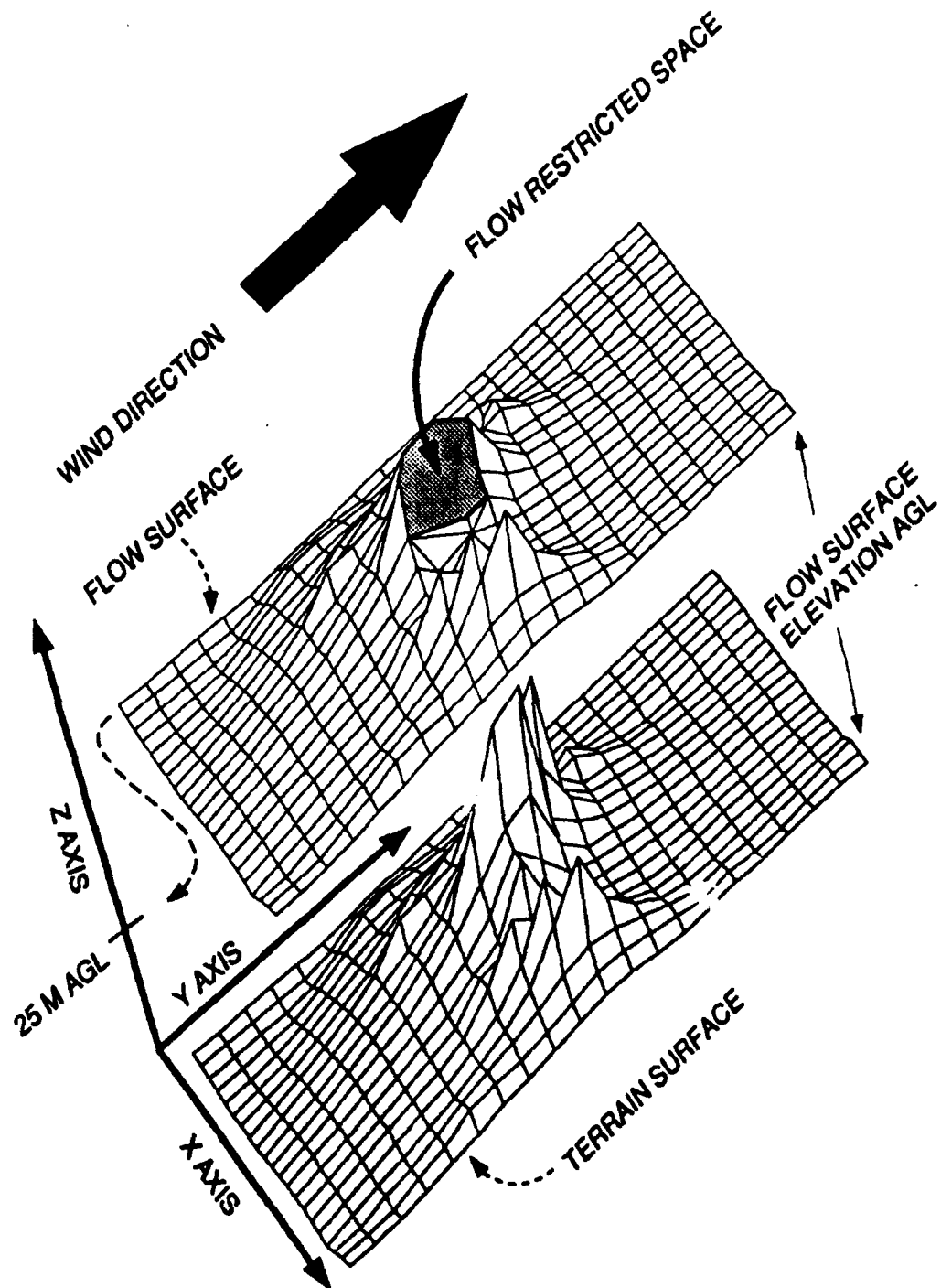
Figure 18. A 3-d illustration of the flow restricted space associated with layer n = 25 m AGL in Fig. 17. The perimeter of the flow restricted space actually intersects the underlying terrain surface. The WOCSS model does not allow mass transport through these flow restricted spaces.

Table 6. Cumulative area of flow restricted spaces (in m^2 and % of total plane area (410,062,500 m^2)), produced by the WOCSS model, at 25 m above ground level under stable conditions using the WSMR site terrain (see Figs. 19-21). Variations in the slope along the top of the modeled boundary layer produced significant changes in the area of flow restricted spaces; changing the speed of initialization data also produced significant variations in flow restricted spaces.

Slope Factor	Stable	Wind speeds doubled
Relaxed	31,437,500 m^2 (7.7%)	
Compressed	27,250,000 m^2 (6.7%)	17,812,500 m^2 (4.3%)
Restricted	22,687,500 m^2 (5.5%)	

Figures 19-21 illustrate the relative areas and changes in the 25-m flow restricted spaces under stable conditions noted in Table 6. Under the conditions examined in Table 6, unstable WOCSS model runs did not produce any flow restricted spaces at 10, 25, or 100 m above ground level, because the increased average speeds in the unstable case, only $\overline{2.45}$ m/s greater than in the stable case at 10 m AGL (see Appendix A), provided sufficient kinetic energy to selected flow surfaces to overcome all intervening WSMR site terrain obstables. This result, in conjunction with the stable case results, illustrates the sensitivity of the WOCSS model to atmospheric initialization conditions. Because this sensitivity is indicative of processes actually observed in nature, this WOCSS model responsiveness is a significant feature that will contribute positively to WOCSS model application potential.

25M OBWIND (SLFAC=1.0) FLOW OBSTRUCTION SPACES 250M GRID
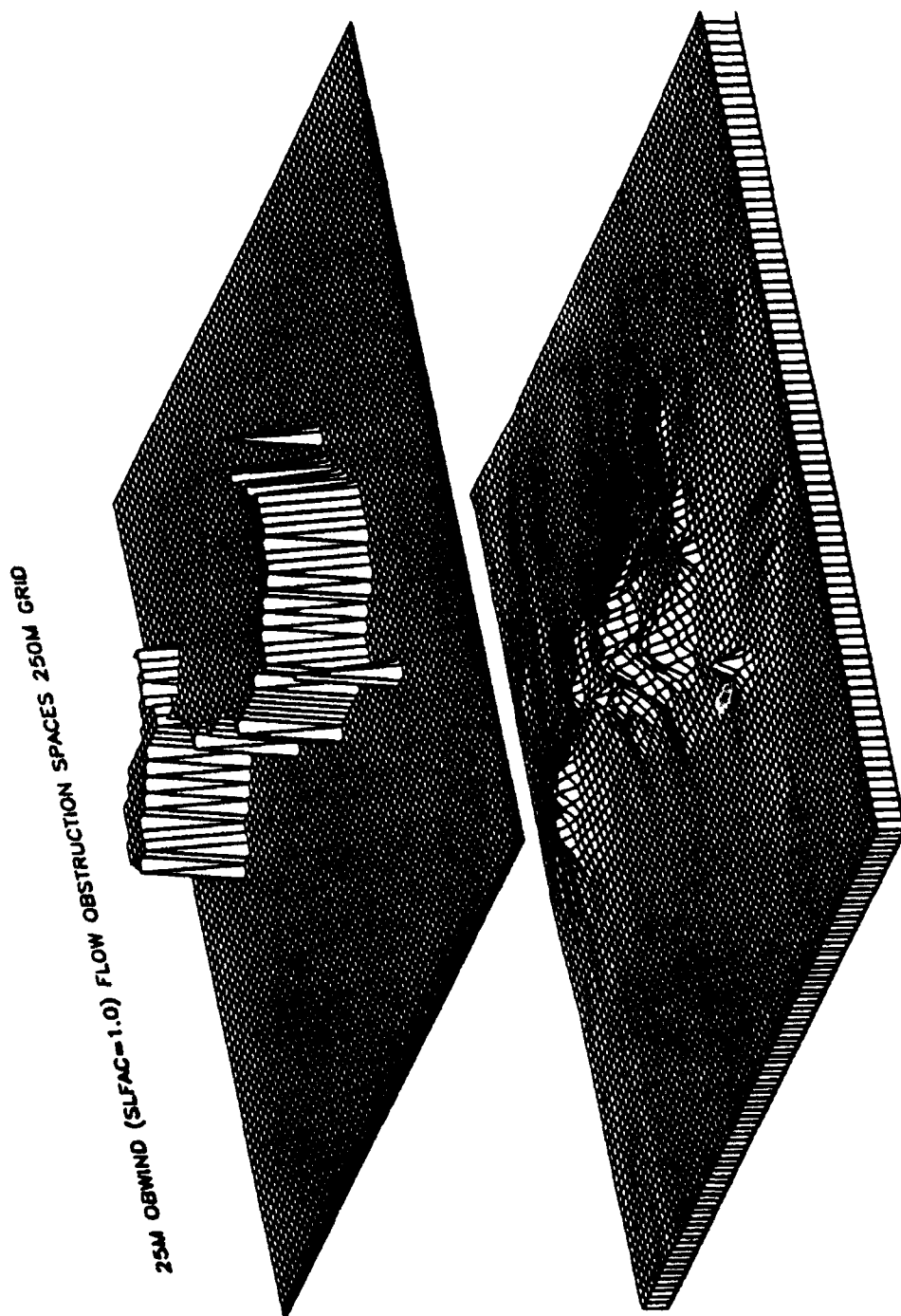
Figure 19. Stable WOCSS flow-restricted spaces at 25 m AGL plotted as elevated regions over the WSMR site terrain (north is located at the top labeled edge of the plotted regions). These flow-restricted regions were calculated using a relaxed top boundary slope factor (layer n+1 in Fig. 17).

25M OBWIND (SLFAC=0.5) FLOW OBSTRUCTION SPACES 250M GRID
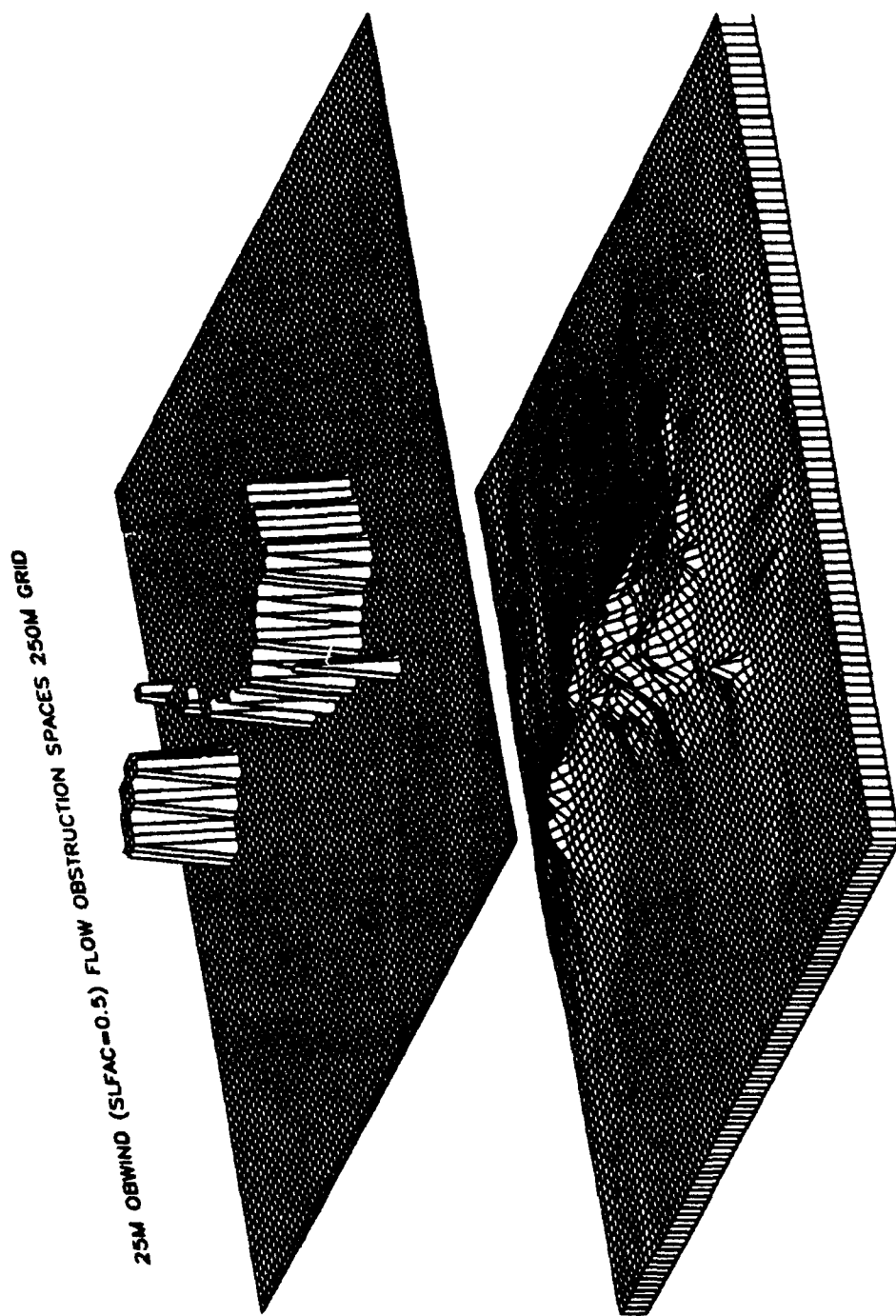
Figure 20. Same as Fig. 19, except that a compressed top boundary slope factor (layer n+2 in Fig. 17) was used to predict the illustrated flow-restricted regions.

25M OBWIND (SLFAC=0.5 & DOUBLED UV) FLOW OBSTRCNS 250M GRID
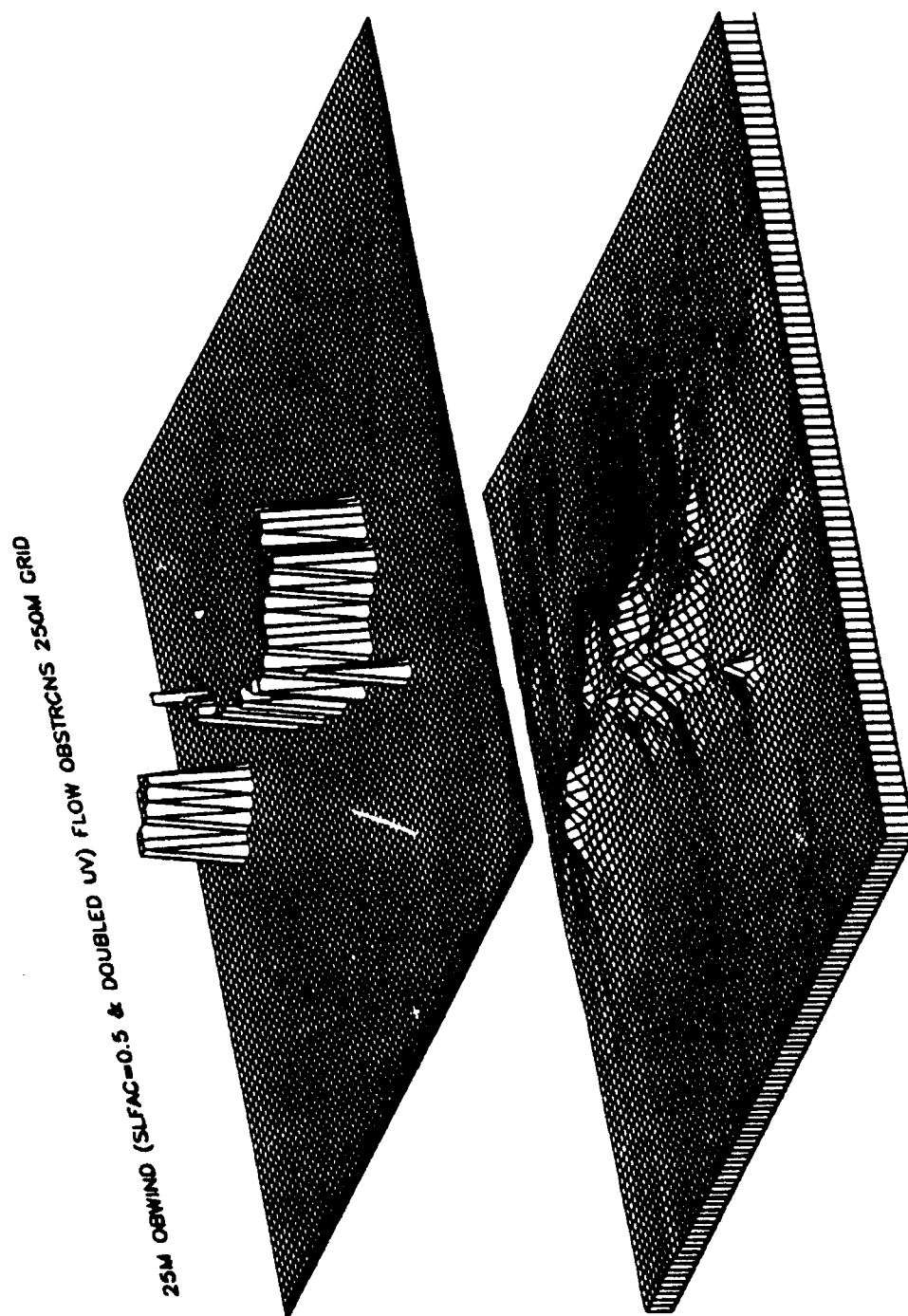
Figure 21. Same as Fig. 20, except that all surface and vertical wind initialization speeds were increased by a factor of 2X the original observed speed magnitudes listed in Appendix A.

For the purposes of this study a compressed slope factor (SLFAC=0.5) was selected for use in the stable case model runs, and a relaxed, boundary layer slope factor (SLFAC=1.0) was used in unstable model runs. Under stable conditions the atmosphere is more resistant to vertical displacement, and this effect is modeled along flow layers over elevated surfaces when the boundary layer top is compressed.

The compression referred to in the previous paragraph results in selective constriction of flow layer thickness in the vicinity of elevated surfaces, and thereby simulates Bernoulli speed-up effects over relative elevation maximums (layer n+2 in Fig. 17). Conversely, a relaxed boundary layer slope factor (layer n+1 in Fig. 17) was used in unstable WOCSS model runs to simulate the effect of reduced resistance to vertical displacement, which is consistent with unstable conditions observed in nature.

3.1.2   OBWIND-WOCSS Statistical Comparisons

The minimum, mean, maximum, and $\pm$ 1.0 standard deviation of each stable case WSMR model run are listed in Table 7 (u components) and Table 8 (v components). Summary statistics (e.g., the root mean square difference, agreement index, and correlation coefficient) are then listed in Table 9 (u components) and Table 10 (v components).

The u component represents approximately 60% of the mean flow vector over the WSMR site stable case model runs. Therefore, significant OBWIND-WOCSS comparison differences are more apparent in the u component statistics. Note the 0.0 WOCSS minimum u components in Table 7 at 10 and 25 m. These 0.0 minimums are associated with the flow restricted spaces discussed earlier (also see Figs. 19-21). Table 8 also lists 0.0 WOCSS v component minimums at 10 and 25 m.

Grid spacing selection does not appear to significantly affect minimum u **components**. For example, 75% of all OBWIND and WOCSS non-zero minimum u components consistently decreased an average of only 3.12% as grid resolution increased from 1000-100 m. However, large differences occurred between WOCSS and OBWIND non-zero minimums at 100m (288% change between 100 m grid OBWIND-WOCSS minimum u components, dropping only to a 260% change at the 1000 m grid stable runs, with OBWIND producing smaller non-zero u and v minimums).

Mean 10 m OBWIND u component magnitudes were 196%, 192%, and 157% greater than WOCSS means at 100, 250, and 1000 m grid spacing, respectively, but this completely reversed in the 25 and 100 m level outputs (for example, at 25 m WOCSS means were 114%, 115%, and 124% greater than OBWIND means over the same, respective grid spacing selection). At the 10 m level WOCSS means increased by 15.6% and 18.4%, respectively, as grid spacing resolution increased from 1000-250, and 1000-100 m.

Maximum 10 m OBWIND u components were also greater than WOCSS maximums by 50%, 42%, and 11%, respectively, at 100, 250, and 1000 m grid spacing, and as in the case of mean components, WOCSS maximums were greater than OBWIND maximums at the 25 and 100 m levels (by 179%, 205%, and 250% at 100, 250, and 1000 m grid spacing, respectively).

Maximum OBWIND u and v components were also always higher when the 100 m grid was employed; conversely, maximum WOCSS u components were always higher when the 1000 m grid was employed (v component maximums behaved erratically. These differences are attributed to variations in OBWIND and WOCSS interpolation algorithms and how these algorithms assign wind velocity values to individual grid points at different grid spacing scales.

Table 7. Basic u component windfield statistics for stable WSMR site OBWIND (u_o) and WOCSS (u_w) windfield outputs (min=Minimum, avg=Mean, max=Maximum, and σ =± 1 Standard Deviation).

Model Source	Statistic	100m grid	250m grid	1000m grid
u_o	min 10m	-0.702485	-0.704065	-0.716014
u_w	min 10m	0.000000	0.000000	0.000000
u_o	min 25m	-0.442709	-0.456276	-0.471527
u_w	min 25m	0.000000	0.000000	0.000000
u_o	min 100m	-0.462111	-0.472506	-0.487063
u_w	min 100m	-1.796830	-1.743190	-1.752220
u_o	avg 10m	-0.984218	-0.969837	-0.902576
u_w	avg 10m	-0.331429	-0.332445	-0.350988
u_o	avg 25m	-0.562656	-0.554448	-0.516859
u_w	avg 25m	-1.201638	-1.195562	-1.161671
u_o	avg 100m	-0.575035	-0.566657	-0.528225
u_w	avg 100m	-1.898141	-1.878264	-1.793024
u_o	max 10m	-1.675720	-1.602960	-1.400490
u_w	max 10m	-1.114420	-1.126640	-1.258820
u_o	max 25m	-0.790097	-0.746207	-0.708540
u_w	max 25m	-1.864310	-1.851610	-1.922880
u_o .	max 100m	-0.788063	-0.746405	-0.711103
u_w	max 100m	-2.202610	-2.278180	-2.486910
u_o	σ 10m	0.084747	0.087054	0.119891
u_w	σ 10m	0.458096	0.462548	0.486732
u_o	σ 25m	0.041628	0.038673	0.063885
u_w	σ 25m	0.332401	0.337656	0.391335
u_o	σ 100m	0.038507	0.036918	0.063807
u_w	σ 100m	0.024130	0.053976	0.184966

Table 8. Basic **v** component windfield statistics for stable WSMR site OBWIND (v_o) and WOCSS (v_w) windfield outputs (min=Minimum, avg=Mean, max=Maximum, and σ =± 1 Standard Deviation).

Model Source	Statistic	100m grid	250m grid	1000m grid
v_o	min 10m	-0.321498	-0.334635	-0.373928
v_w	min 10m	0.000000	0.000000	0.000000
v_o	min 25m	-0.248106	-0.288680	-0.334019
v_w	min 25m	0.000000	0.000000	0.000000
v_o	min 100m	-0.250070	-0.287582	-0.330255
v_w	min 100m	-1.264500	-1.231830	-1.275420
v_o	avg 10m	-0.625345	-0.615236	-0.567920
v_w	avg 10m	-0.238849	-0.236722	-0.243642
v_o	avg 25m	-0.379551	-0.373617	-0.346868
v_w	avg 25m	-0.867566	-0.855768	-0.813544
v_o	avg 100m	-0.373936	-0.368102	-0.341767
v_w	avg 100m	-1.377465	-1.359816	-1.287632
v_o	max 10m	-0.935505	-0.935421	-0.932253
v_w	max 10m	-0.806409	-0.809420	-0.845871
v_o	max 25m	-0.514950	-0.485605	-0.445452
v_w	max 25m	-1.626910	-1.493900	-1.543850
v_o	max 100m	-0.502560	-0.476896	-0.438018
v_w	max 100m	-1.687400	-1.723340	-1.679680
v_o	σ 10m	0.115050	0.114872	0.122096
v_w	σ 10m	0.330129	0.329335	0.336934
v_o	σ 25m	0.053658	0.045551	0.042943
v_w	σ 25m	0.240193	0.243583	0.283064
v_o	σ 100m	0.050773	0.043380	0.041844
v_w	σ 100m	0.018221	0.039398	0.130902

Table 9. Summary u component windfield statistics for WSMR site 10, 25, and 100 m stable case OBWIND (u_o) and WOCSS (u_w) windfield outputs (rms=Root Mean Square Difference, agi=Agreement Index, and r=Correlation Coefficient).

Component Sources	Statistic	100m grid	250m grid	1000m grid
u_o-u_w	rms 10m	0.809818	0.806546	0.781163
u_o-u_w	rms 25m	0.730285	0.741253	0.812019
u_o-u_w	rms 100m	1.337306	1.345582	1.395853
u_o-u_w	agi 10m	0.092185	0.074378	0.056239
u_o-u_w	agi 25m	0.085009	0.104984	0.209522
u_o-u_w	agi 100m	0.048872	0.060108	0.135892
u_o-u_w	r 10m	-0.068655	-0.059891	0.051799
u_o-u_w	r 25m	-0.113005	0.068513	0.346386
u_o-u_w	r 100m	0.009543	0.223450	0.742598

Table 10. Summary v component windfield statistics for WSMR site 10, 25, and 100 m stable case OBWIND (v_o) and WOCSS (v_w) windfield outputs (rms=Root Mean Square Difference, agi=Agreement Index, and r=Correlation Coefficient).

Component Sources	Statistic	100m grid	250m grid	1000m grid
v_o-v_w	rms 10m	0.506293	0.504318	0.487292
v_o-v_w	rms 25m	0.551708	0.555286	0.588299
v_o-v_w	rms 100m	1.014435	1.017097	1.041666
v_o-v_w	agi 10m	0.268167	0.248396	0.201858
v_o-v_w	agi 25m	0.147221	0.141707	0.195270
v_o-v_w	agi 100m	0.083071	0.083840	0.126815
v_o-v_w	r 10m	0.242422	0.242713	0.276910
v_o-v_w	r 25m	-0.015995	-0.064950	0.174258
v_o-v_w	r 100m	0.069937	0.204643	0.785983

Table 11. Summary u component windfield statistics for WSMR site 10, 25, and 100 m unstable case OBWIND (u_o) and WOCSS (u_w) windfield outputs (rms=Root Mean Square Difference, agi=Agreement Index, and r=Correlation Coefficient).

Component Sources	Statistic	100m grid	250m grid	1000m grid
u_o-u_w	rms 10m	2.094479	2.050216	2.138106
u_o-u_w	rms 25m	0.674350	0.613055	0.537859
u_o-u_w	rms 100m	0.245543	0.190512	0.183246
u_o-u_w	agi 10m	0.207519	0.135198	0.111055
u_o-u_w	agi 25m	0.273099	0.195771	0.126571
u_o-u_w	agi 100m	0.412048	0.312226	0.487617
u_o-u_w	r 10m	0.087668	0.067988	0.307092
u_o-u_w	r 25m	-0.026439	0.135907	0.471575
u_o-u_w	r 100m	0.012076	0.224244	0.613856

Table 12. Summary v component windfield statistics for WSMR site 10, 25, and 100 m unstable case OBWIND (v_o) and WOCSS (v_w) windfield outputs (rms=Root Mean Square Difference, agi=Agreement Index, and r=Correlation Coefficient).

Component Sources	Statistic	100m grid	250m grid	1000m grid
v_o-v_w	rms 10m	0.759228	1.230143	0.785934
v_o-v_w	rms 25m	1.266384	1.326321	1.216271
v_o-v_w	rms 100m	2.597788	2.740088	2.606363
v_o-v_w	agi 10m	0.134758	0.328341	0.212271
v_o-v_w	agi 25m	0.067452	0.258935	0.351719
v_o-v_w	agi 100m	0.033449	0.137587	0.196585
v_o-v_w	r 10m	0.058383	0.128353	0.403180
v_o-v_w	r 25m	0.406679	0.173538	0.943587
v_o-v_w	r 100m	0.435636	0.183103	0.955592

In general, the WOCSS model **v** components (Table 8) behaved in a similar manner to the **u** components, producing significantly greater winds than OB-WIND at 25 and 100 m levels (outside of flow restricted spaces); and the WOCSS ouput winds had significantly greater variance in distributions at 10 and 25 m (see the standard deviation data in Tables 7 and 8). Variance in mean WOCSS standard deviations also increased as the grid spacing increased (by 17.7% from 100-1000 m and 15.9% from 250-1000 m grid spacing). The increased variance at 10 and 25 m is exaggerated because of the effect of flow restricted space in the WOCSS model outputs at 10 and 25 m in the stable case scenario.

Comparison of the summary statistics in Tables 9-10 (stable case) and Tables 11-12 (unstable case) indicate very low agreement indices and correlation between OBWIND and WOCSS model results in 89% of all cases (e.g., average **u** and **v** component agreement indices were, respectively, 0.096353 and 0.198378 in the stable case, and 0.251234 and 0.191233 in the unstable case); unstable agreement was $\overline{50}$% better than stable case agreement.

Only the 100 m level **u** and **v** components with 1000 m grid spacing had consistently good correlation ($r > 0.5$), but this high correlation case was not associated with the largest agreement index. Therefore, agreement indices and correlation coefficients do not appear to produce proportionally equivalent results. However, agreement and correlation generally deteriorated as grid resolution increased.

Tables 9-12 imply that agreement indexes and correlation coefficients are generally higher for the unstable case, where more kinetic energy was available in the initialization data (winds at 10 m in the unstable case were approximately 104% greater in magnitude than in the stable case (see Appendix A for a listing of the stable and unstable initialization data)). Because of the availability of sufficient kinetic energy in the unstable case, no flow restricted space was predicted by the WOCSS model at 10, 25, and 100 m AGL, which largely explains the improved agreement and correlation with OBWIND model results compared to the WSMR stable case comparisons.

50

3.1.3 OBWIND-WOCSS Graphical Comparisons

Results presented up to this point have been in tabular form, and significant results have been referred to only through textual description (primarily to economize on the total number of graphical plots that would be necessary to display all the previously discussed relationships among the WSMR results). However, graphical presentation of selected model output fields becomes necessary at this point to illustrate the value of spatial analysis of model results, which in many cases provides more useful information about model performance than any of the previously discussed statistics.

For example, Fig. 22 is a wind vector field plot of the OBWIND 10 m stable output at 250 m grid spacing (81 × 81 grid points). The density of this data output nearly saturates the plot area and was therefore used as the useful upper threshold in producing plots of model outputs (e.g., vector plots of 100 m grid model outputs were illegible in many cases).

Figure 23 is a qualitative graphical representation of stable case OBWIND wind speeds, ($\sqrt{u^2 + v^2}$), associated with the 10 m layer wind vectors plotted in Fig. 22. Figures 24 and 25 are the 10 m WOCSS plots corresponding to the OBWIND plots in Figs. 22 and 23 respectively. Notice the zeroing effect of the flow restricted space predicted by the WOCSS model in the center of Fig. 24. This effect is more obvious in Fig. 25, where speed is plotted as a surface over the WSMR terrain.

Wind vector differences, $\vec{\Delta} = \vec{V}_{WOCSS} - \vec{V}_{OBWIND}$, were also calculated (see Fig. 26). Negative difference vectors are indicated in the center of the wind-field, which coincide with the WOCSS flow restricted space over higher terrain elevations (see Figs. 19-21). Outside of the flow restricted spaces direction agreement with OBWIND results are good, but WOCSS wind speeds are generally higher than OBWIND wind speeds over the entire unrestricted flow space (most noticable at 25 and 100 m AGL). This is attributed to WOCSS mass balancing

OBWIND 10M STABLE 250M GRID

Figure 22. OBWIND 10 m stable case wind vector field plot for the WSMR site using 250 X 250 square m grid cells (81 X 81). WSMR site terrain elevation contours are also included (north is located along the top, labeled edge of the plot). Magnitude of minimum, average, and maximum speed vectors are, respectively, 0.917, 1.154, and 1.638 m/s (vector plot size is proportional to the speed associated with each vector).

10M OBWIND U+V SPEED 250M GRID

Figure 23. OBWIND 10 m stable case wind speed plot for the WSMR site using 250 X 250 square m grid cells (81 X 81). WSMR site terrain elevation is plotted below the speed surface plot (north is located at the top labeled edge of the plotted regions). Minimum, average, and maximum speed values are, respectively, 0.917, 1.154, and 1.638 m/s, where speed increases upward along the vertical plot axis.

Figure 24. WOCSS 10 m stable case wind vector field plot for the WSMR site using 250 X 250 square m grid cells (81 X 81). WSMR site terrain elevation contours are also included (north is located at the top labeled edge of the plot). Minimum, average, and maximum vector speed magnitudes are, respectively, 0.000, 0.408, and 1.390 m/s (vector plot size is proportional to the speed associated with each vector).

WOCSS U+V SPEED

Figure 25. WOCSS 10 m stable case wind speed plot for the WSMR site using 250 X 250 square m grid cells (81 X 81). WSMR site terrain elevation is plotted below the speed surface plot (north is located at the top labeled edge of the plotted regions). Minimum, average, and maximum speed values are, respectively, 0.000, 0.408, and 1.386 m/s, where speed increases upward along the vertical plot axis.

Figure 26. WOCSS-OBWIND 10 m stable case wind vector difference field plot for the WSMR site using 250 X 250 square m grid cells (81 X 81). WSMR site terrain elevation contours are also included (north is located at the top labeled edge of the plot). Magnitude of the average vector difference = 0.790 m/s, and magnitude of the maximum vector difference = 1.638 m/s.

adjustments over the remaining flow space, which provides gross adjustment for the effect of flow restricted spaces on the windfield mass consistency via speed adjustments to all free flow grid volumes.

The result described in the previous paragraph is consistent with data listed in Tables 7 and 8; it is also reflected in the behavior of WOCSS wind speed-terrain correlation. For example, using 100 m grid spacing, at 10 and 25 m AGL the WOCSS wind speed correlation with underlying WSMR terrain under stable conditions is very poor (r=-0.034921 and -0.068222, respectively). However, at 100 m AGL under the same circumstances correlation is very strongly inversely related (r=-0.779617).

At 10 and 25 m AGL flow restricted space diminishes correlation of the WOCSS wind fields with terrain, but at 100 m AGL (where there was no predicted flow restricted space) the generally monotonic winds are more inversely related to the lower elevations than the higher elevations (primarily because a majority of the WSMR terrain was composed of a low basin plain, the inverse relationship of WOCSS 100 m winds with terrain was strong). This inverse correlation would not have been as significant at 100 m AGL if the WOCSS model predicted localized Bernoulli speed up effects in the vicinity of higher terrain.

The wind vector difference plots illustrate that the WOCSS mass balancing algorithm does not calculate dy/dx or dx/dy horizontal wind direction changes that would result in nature near flow restricted spaces, and the WOCSS model also does not calculate local horizontal Bernoulli speed up effects, unless these effects were incorporated in the initialization wind data. These are all significant limitations to the WOCSS model's potential to produce valid, realistic windfield outputs. However, these limitations could be compensated for to varying degrees by selectively coupling WOCSS output with other models (which will be discussed in Section 4).

Figure 27 is a plot of 25 m OBWIND stable case WSMR data at 1000 m × 1000 m grid spacing and is followed by a plot of the same data in Fig. 28, where grid spacing has been set to 250 m × 250 m; Figures 27-28 do not show significant differences in grid spacing effect because of the monotonic behavior of the general wind field resulting from initializing the model with only one vertical wind profile. However, when the OBWIND speed surface plots are compared (Figs. 29 and 30) using similar grid spacing selections, subtle speed maximums are apparent in the 250 m grid plot (Fig. 30) that are missed in the 1000 m grid plot (Fig. 29).

Figures 31-34 illustrate the same sequence of plots using 25 m WOCSS stable case outputs, which compare to Figs. 27-30 respectively. Note that flow restricted space at 25 m AGL is significantly smaller than that at 10 m AGL (refer to Figs. 24 and 32); WOCSS flow is less influenced by terrain effects as flow surface elevation above ground level increases, as observed in nature.

The 25 m level vector differences are also contrasted using 250 and 1000 m grid plots in Figs. 35 and 36, respectively. Comparison of the center region differences in the vicinity of the highest terrain illustrate a smoothing effect in the 1000 m grid plot (Fig. 35); the 250 m gridded model output would be significantly more accurate in performing high resolution flow trajectory operations (for example, in urban scale applications).

Figures 37-39 compare WSMR site 100 m stable case OBWIND and WOCSS model outputs using 250 m grid spacing. In this comparison the WOCSS model predicts no flow restricted spaces at 100 m AGL (Fig. 38), and WOCSS winds are all greater than those predicted by the OBWIND model (Fig. 39). These results are reflected in Tables 12 and 13 but are more obvious in graphical spatial presentations (e.g., Figs. 37-39).
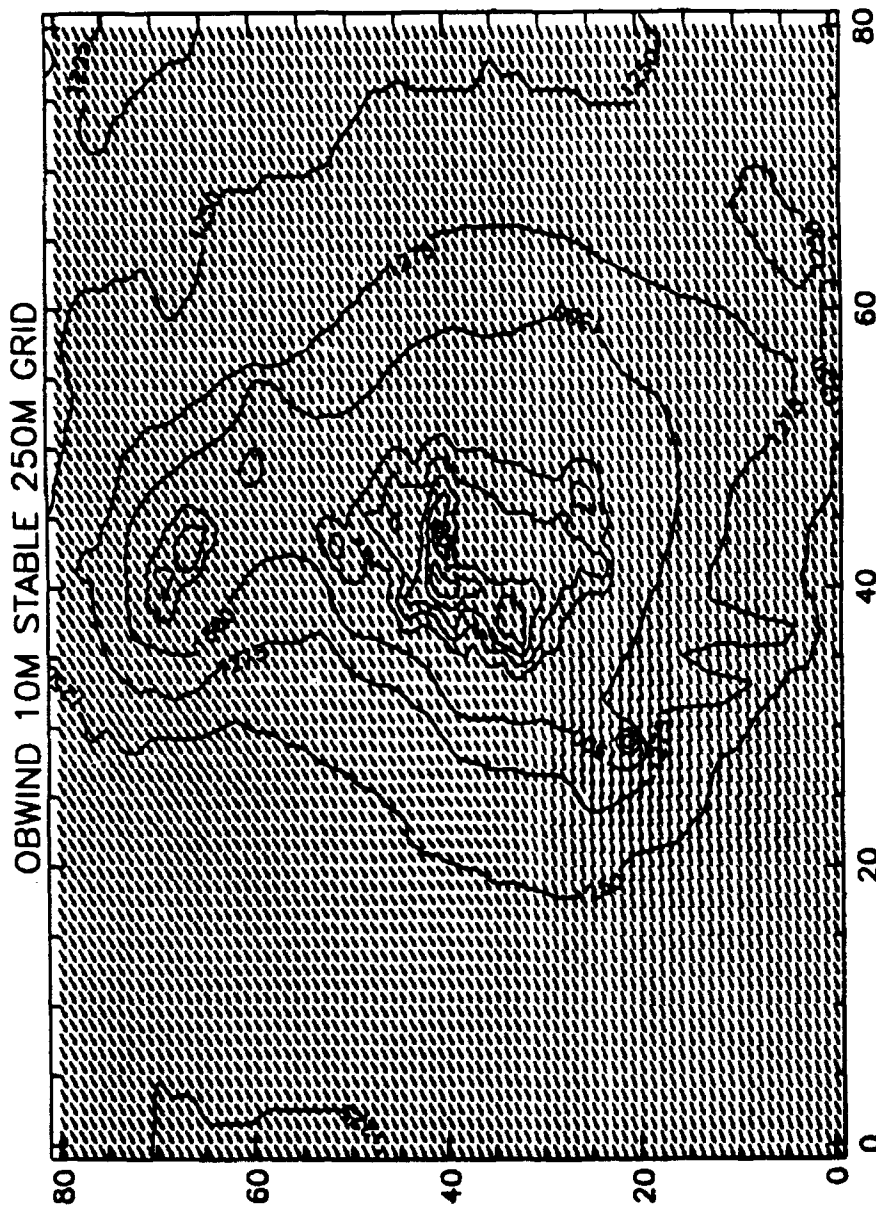
Figure 27. OBWIND 25 m stable case wind vector field plot for the WSMR site using 1000 X 1000 square m grid cells (21 X 21). WSMR site terrain elevation contours are also included (north is located at the top labeled edge of the plot). Magnitude of the average speed vector = 0.623 m/s, and magnitude of the maximum speed vector = 0.791 m/s.
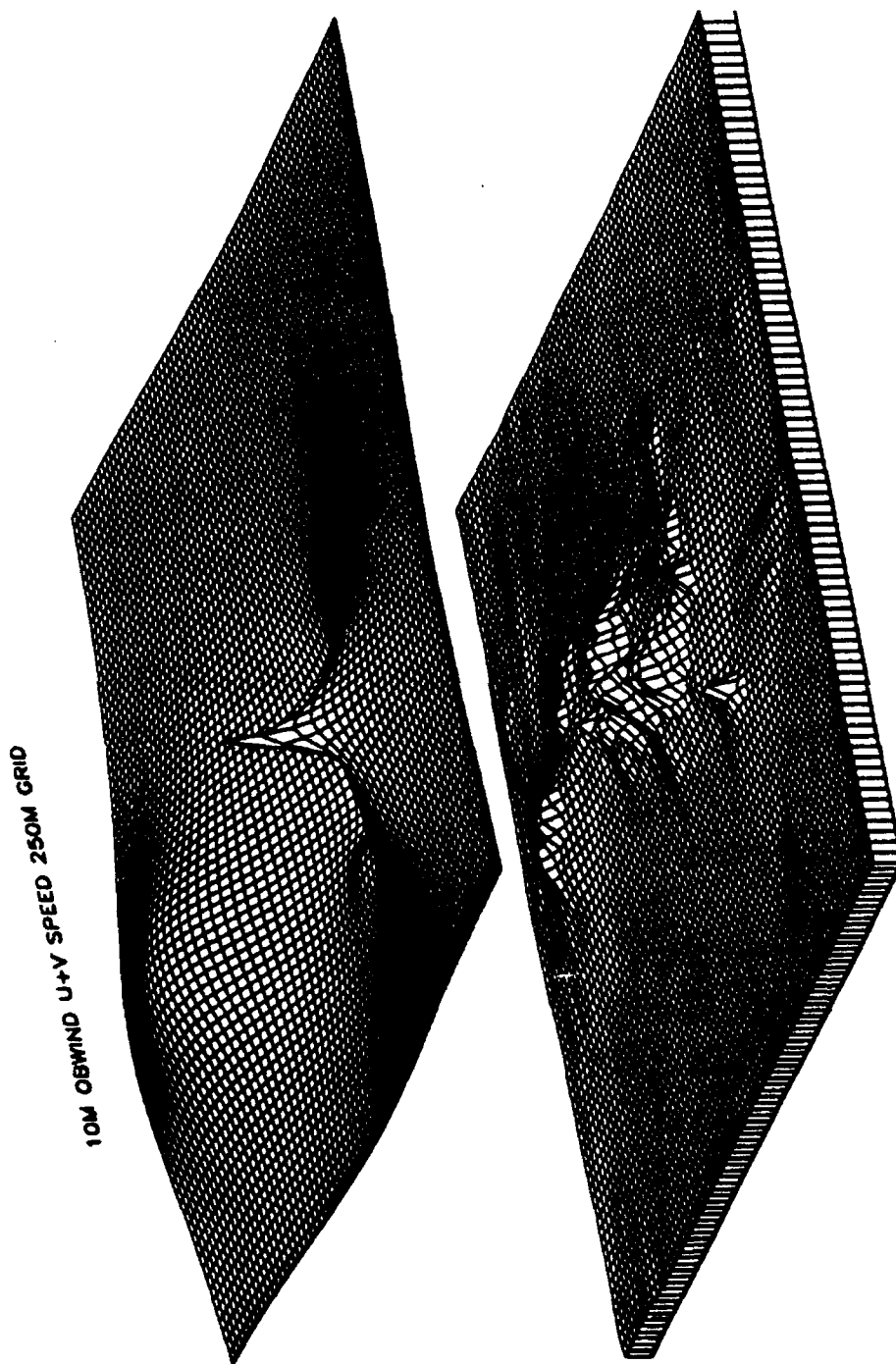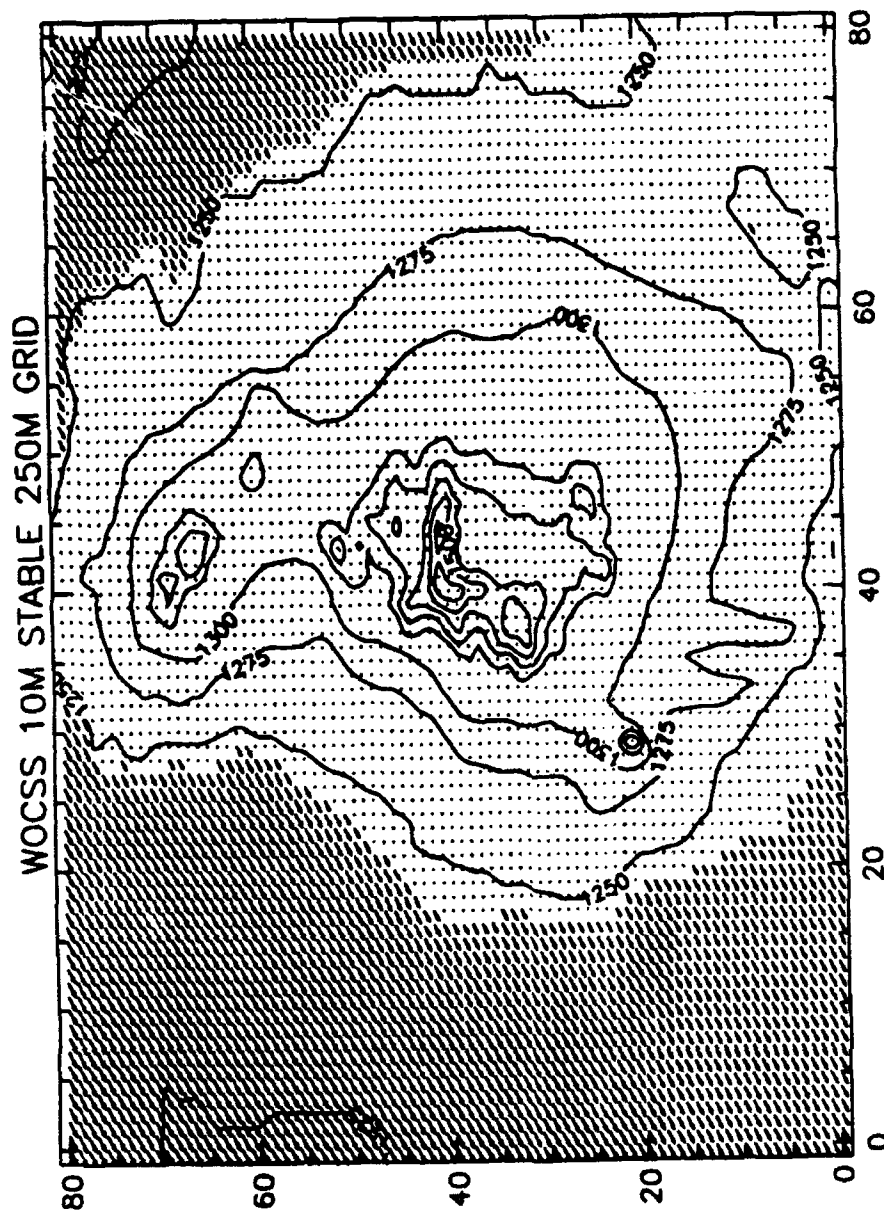
Figure 28. OBWIND 25 m stable case wind vector field plot for the WSMR site using 250 X 250 square m grid cells (81 X 81). WSMR site terrain elevation contours are also included (north is located at the top labeled edge of the plotted regions). Magnitude of the average speed vector = 0.670 m/s, and magnitude of the maximum speed vector = 0.821 m/s.

25M OBWIND WIND SPEED 1000M GRID
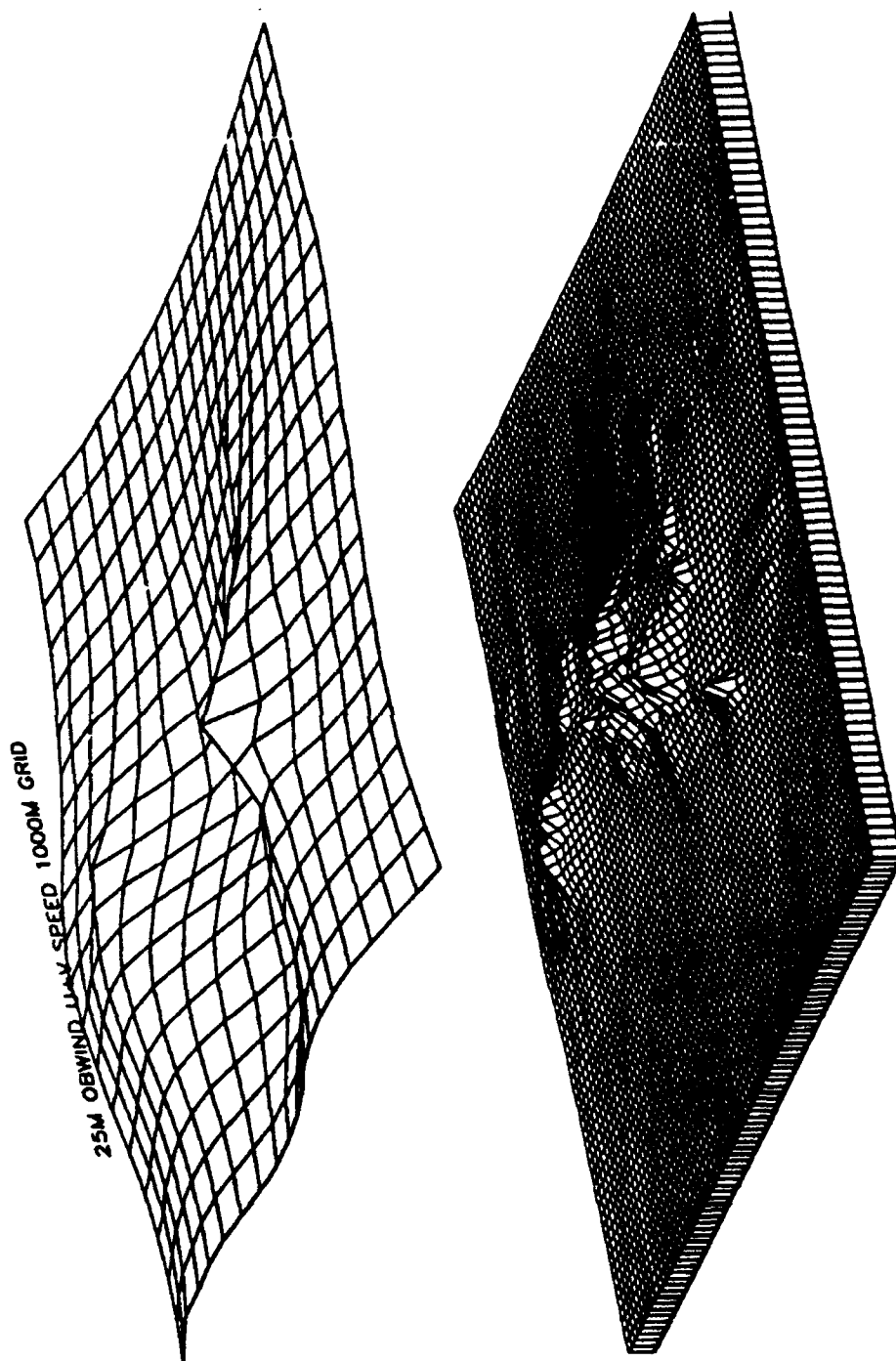
Figure 29. OBWIND 25 m stable case wind speed plot for the WSMR site using 1000 X 1000 square m grid cells (21 X 21). WSMR site terrain elevation is plotted below the speed surface plot (north is located at the top labeled edge of the plotted regions). Minimum, average, and maximum speed values are, respectively, 0.599, 0.623, and 0.791 m/s, where speed increases upward along the vertical plot axis.
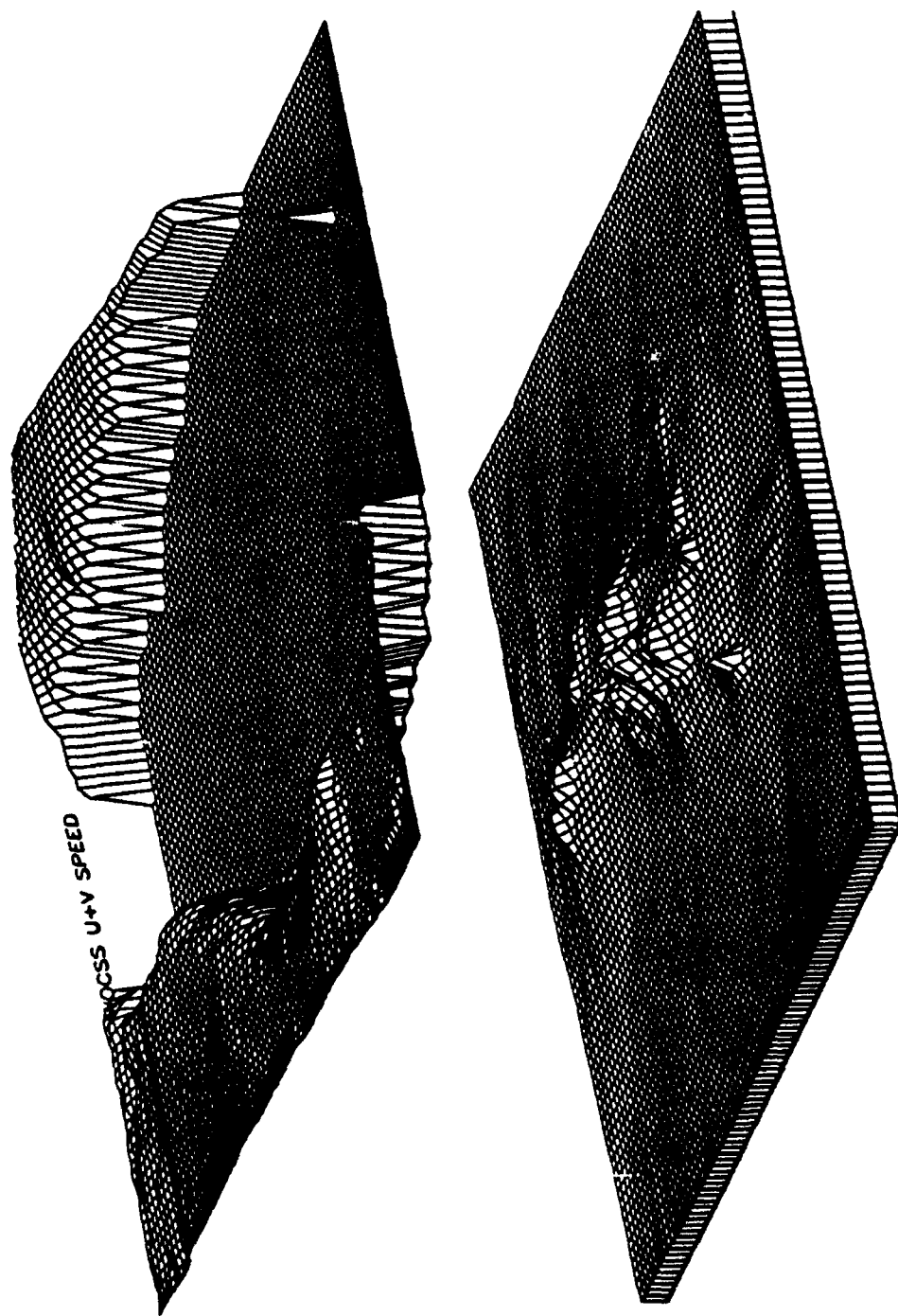
61

25M OBWIND MAX SPEED 250M GRID
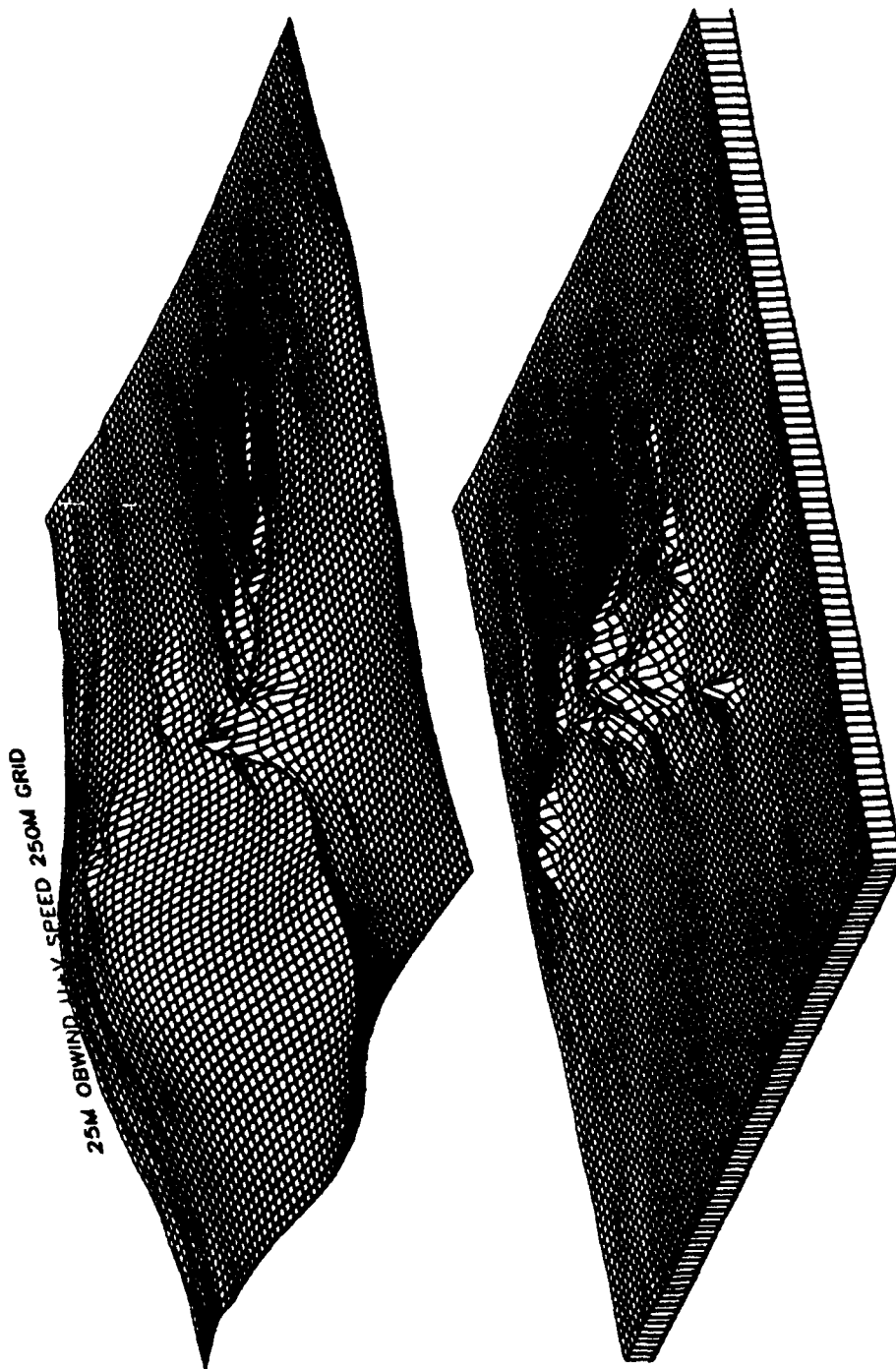
Figure 30. OBWIND 25 m stable case wind speed plot for the WSMR site using 250 X 250 square m grid cells (81 X 81). WSMR site terrain elevation is plotted below the speed surface plot (north is located at the top labeled edge of the plotted regions). Minimum, average, and maximum speed values are, respectively, 0.581, 0.670, and 0.821 m/s, where speed increases upward along the vertical plot axis.
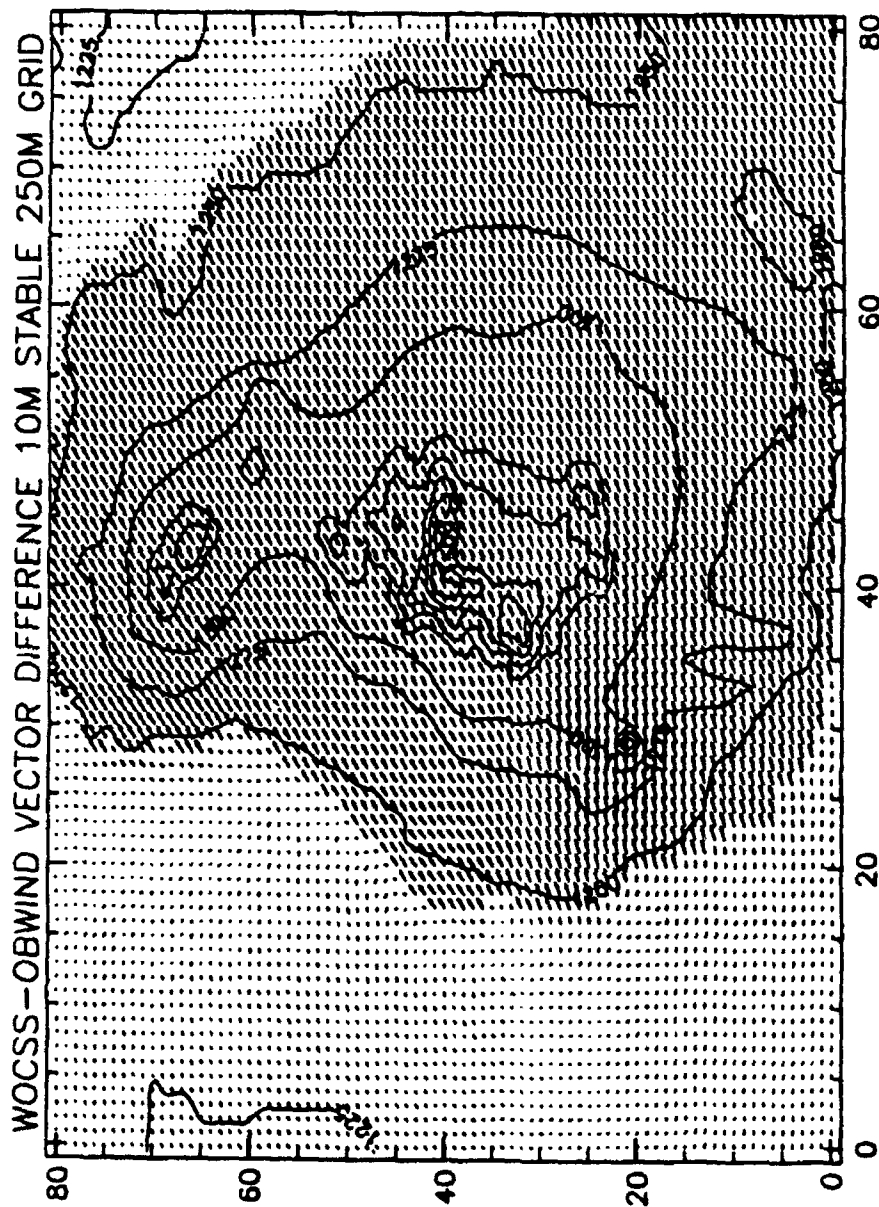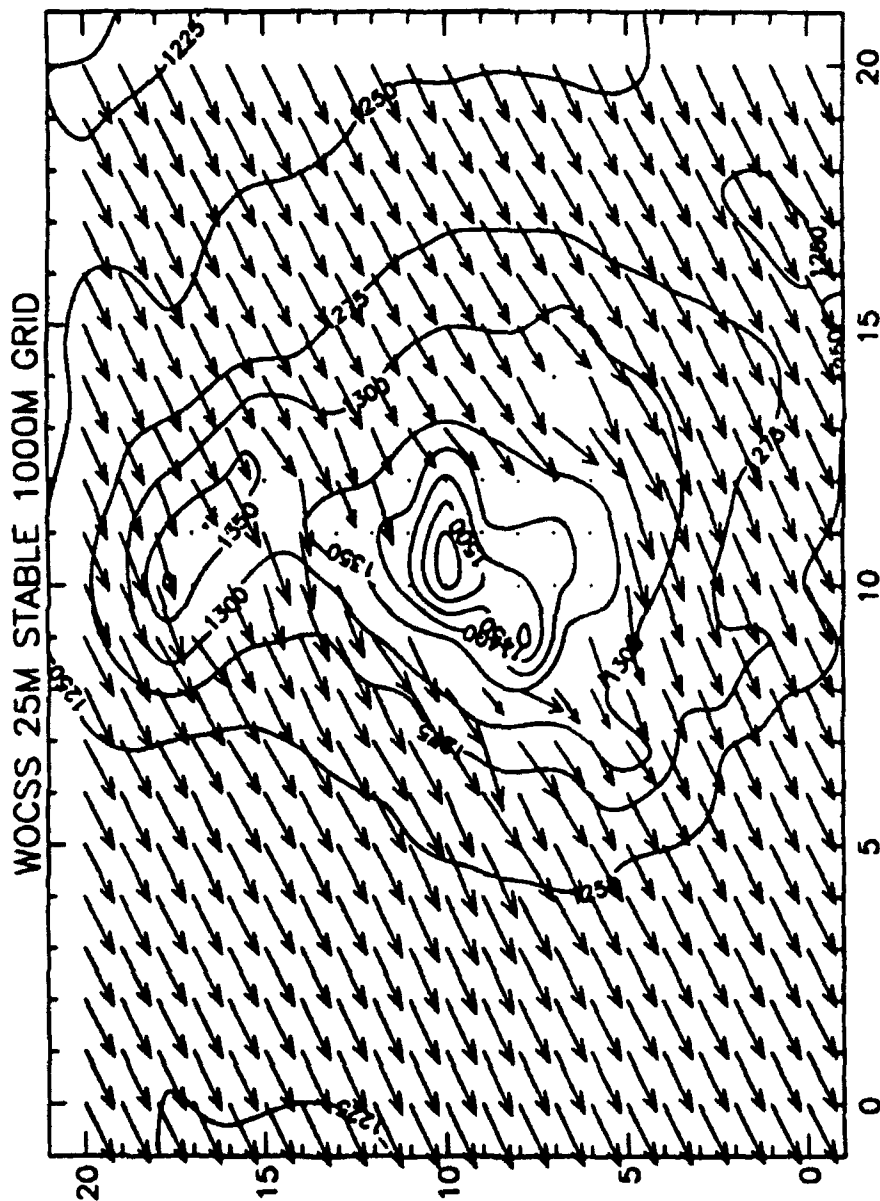
Figure 31. WOCSS 25 m stable case wind vector plot for the WSMR site using 1000 X 1000 square m grid cells (21 X 21). WSMR site terrain elevation contours are also included (north is located at the top labeled edge of the plot). Magnitude of the average speed vector = 1.423 m/s, and magnitude of the maximum speed vector = 2.139 m/s.

Figure 32. WOCSS 25 m stable case wind vector field plot for the WSMR site using 250 X 250 square m grid cells (81 X 81). WSMR site terrain elevation contours are also included (north is located at the top labeled edge of the plot). Magnitude of average speed vector = 1.472 m/s, and magnitude of the maximum speed vector = 2.070 m/s.

25M WOCSS S U+V SPEED
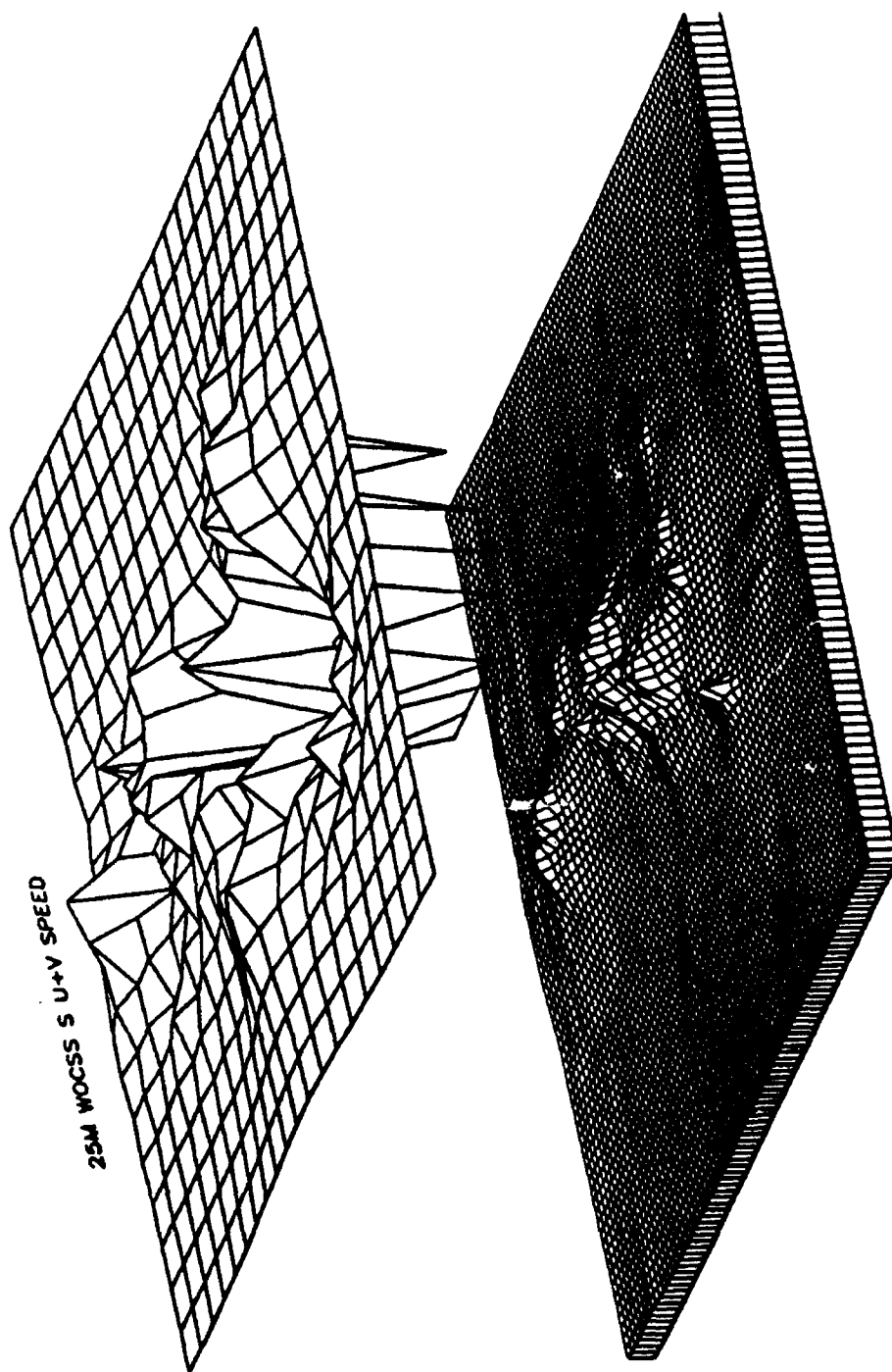
Figure 33. WOCSS 25 m stable case wind speed plot for the WSMR site using 1000 X 1000 square m grid cells (21 X 21). WSMR site terrain elevation is plotted below the speed surface plot (north is located at the top labeled edge of the plotted regions). Minimum, average, and maximum speed values are, respectively, 0.000, 1.423, and 2.139 m/s, where speed increases upward along the vertical plot axis.
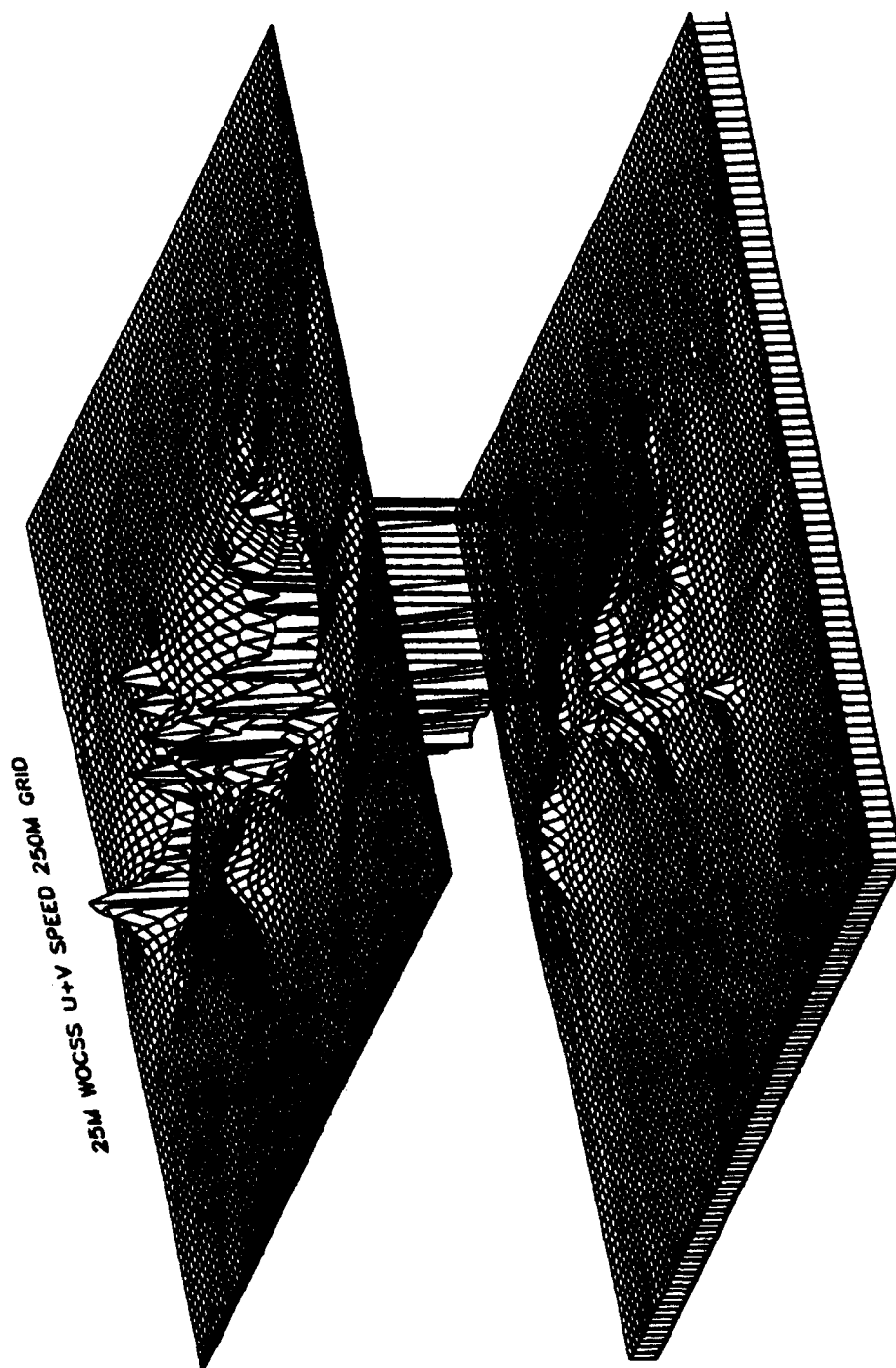
Figure 34. WSMR 25 m stable case wind speed plot for the WSMR site using 250 X 250 square m grid cells (81 X 81). WSMR site terrain elevation is plotted below the speed surface plot (north is located at the top labeled edge of the plotted regions). Minimum, average, and maximum speed values are, respectively, 0.000, 1.472, and 2.070 m/s, where speed increases upward along the vertical plot axis.

25M WOCSS U+V SPEED 250M GRID

66
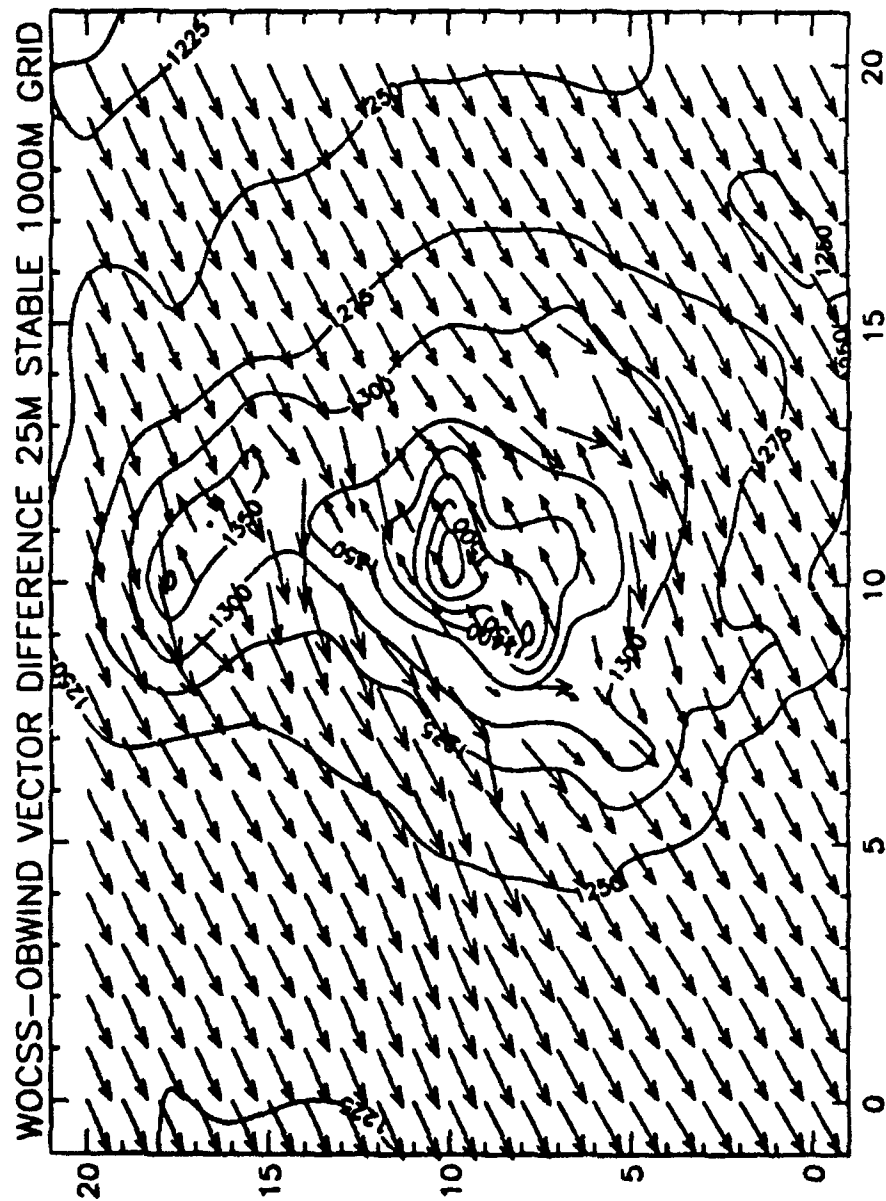
Figure 35. WOCSS-OBWIND 25 m stable case wind vector difference field plot for the WSMR site using 1000 X 1000 square m grid cells (21 X 21). WSMR site terrain elevation contours are also included (north is located at the top labeled edge of the plot). Magnitude of the average vector differences = 0.892 m/s, and magnitude of the maximum vector difference = 1.454 m/s.
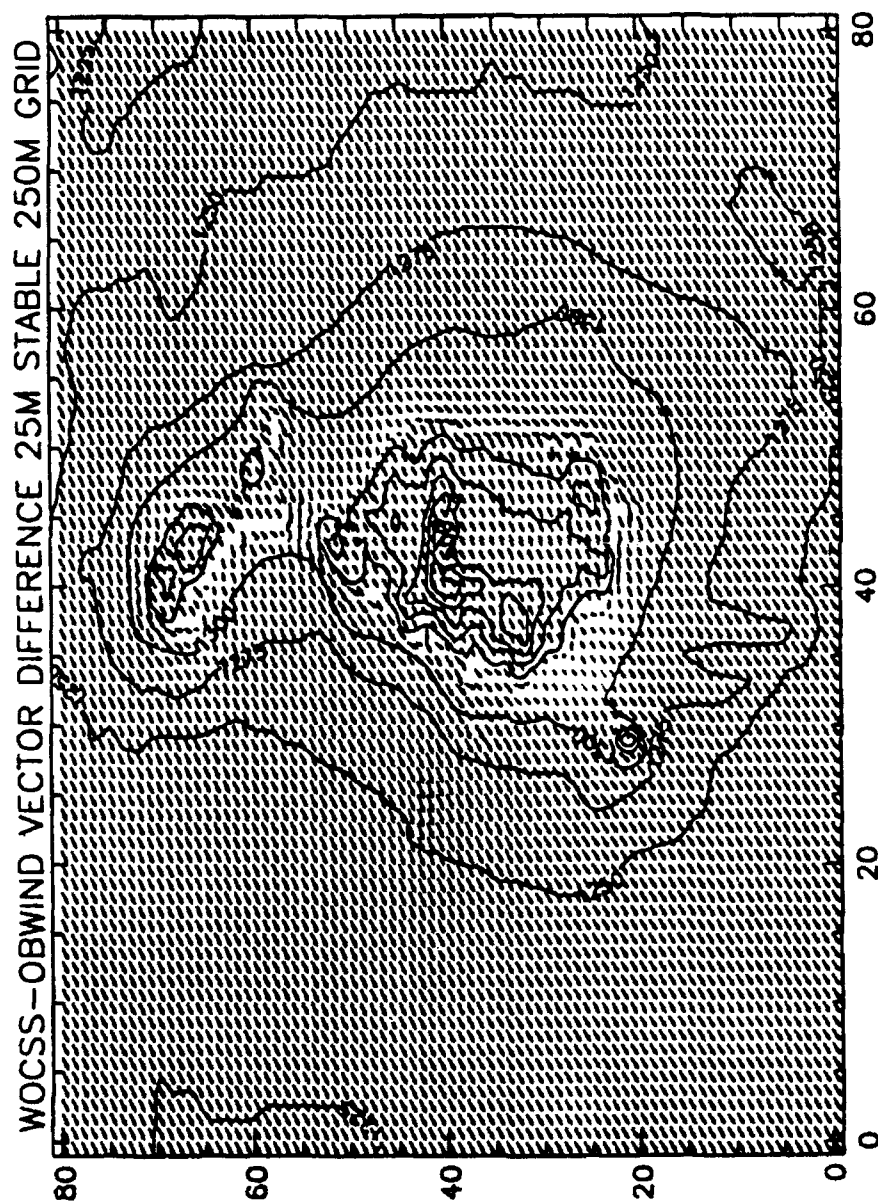
Figure 36. WOCSS-OBWIND 25 m stable case wind vector differences plot for the WSMR site using 250 X 250 square m grid cells (81 X 81). WSMR site terrain elevation contours are also included (north is located at the top labeled edge of the plot). Magnitude of average vector differences = 0.892 m/s, and magnitude of the maximum vector difference = 1.328 m/s.
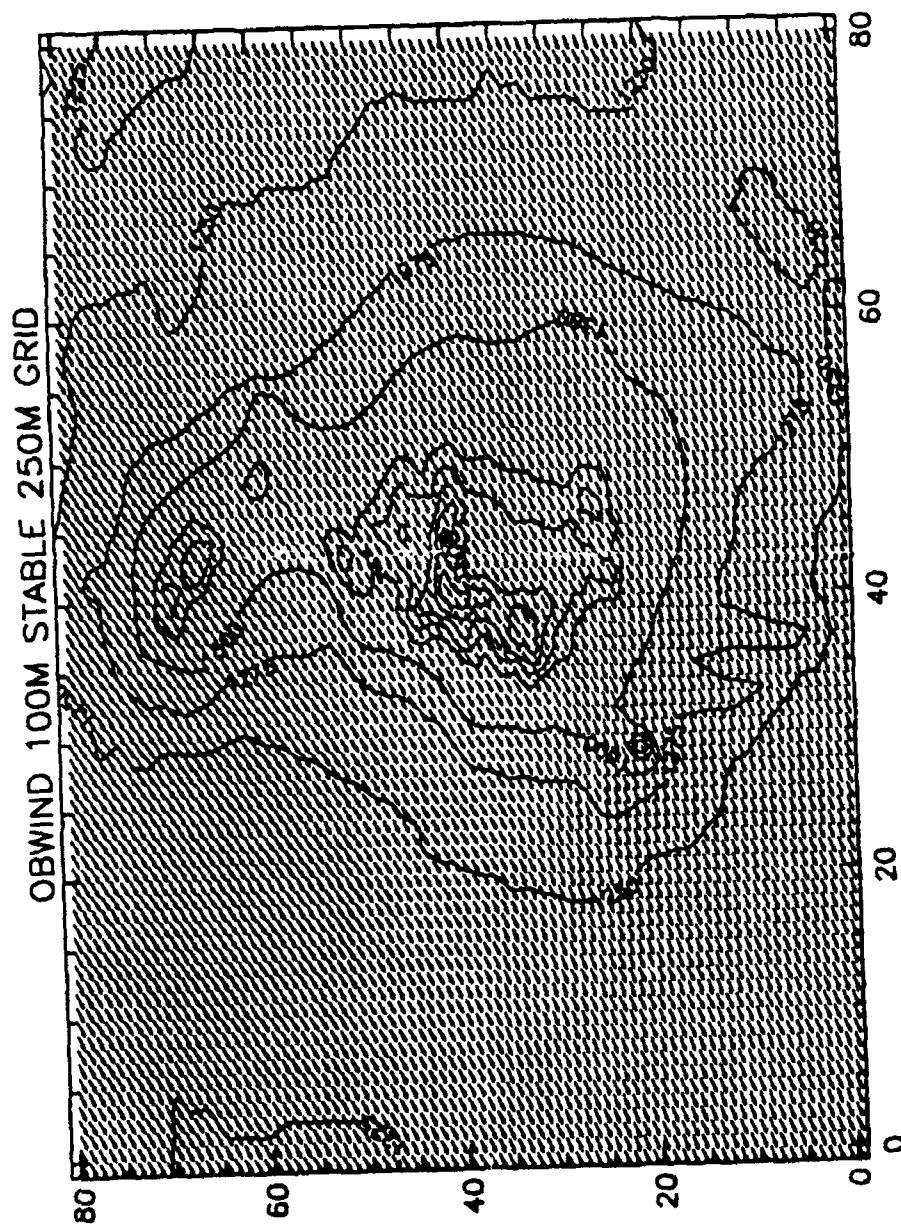
Figure 37. OBWIND 100 m stable case wind vector field plot for the WSMR site using 250 X 250 square m grid cells (81 X 81). WSMR site terrain elevation contours are also included (north is located at the top labeled edge of the plot). Magnitude of average speed vector = 0.677 m/s, and magnitude of the maximum speed vector = 0.819.
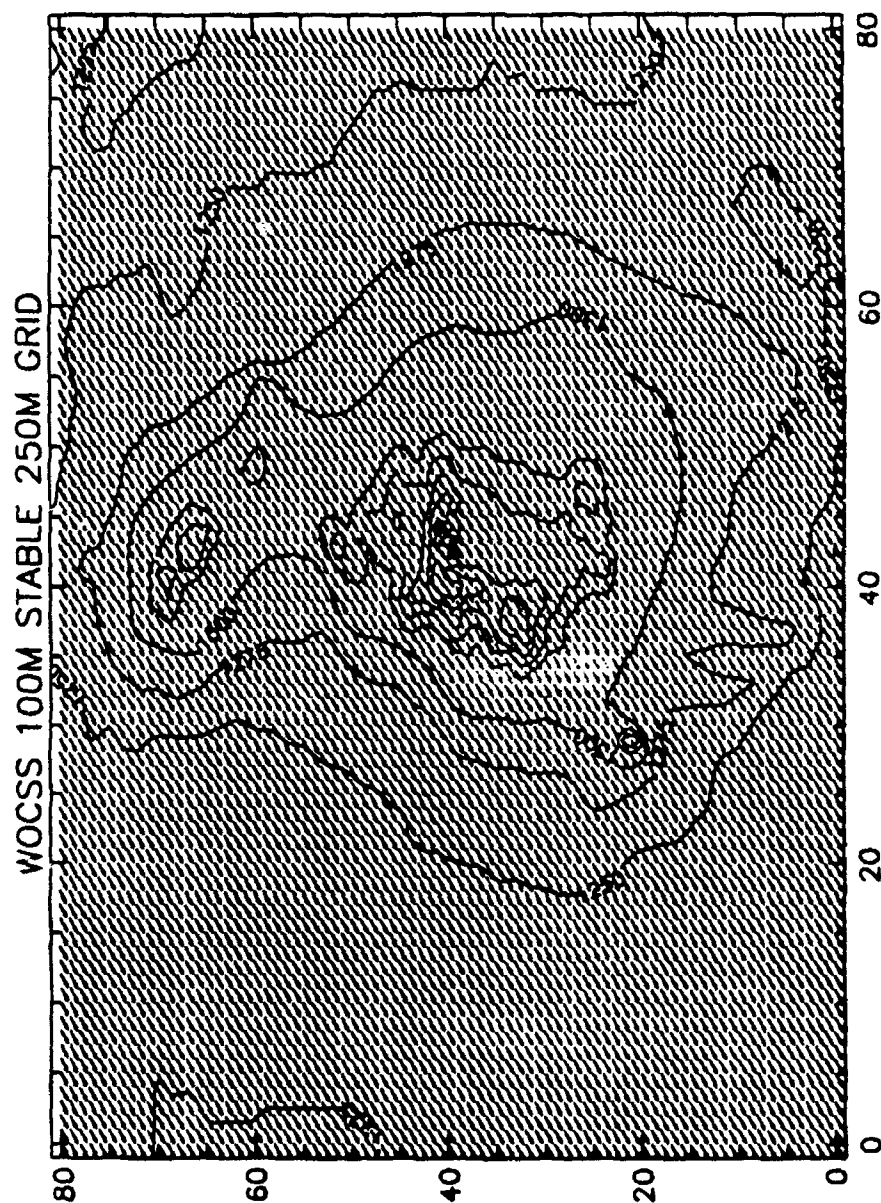
Figure 38. WOCSS 100 m stable case wind vector field plot for the WSMR site using 250 X 250 square m grid cells (81 X 81). WSMR site terrain elevation contours are also included (north is located at the top labeled edge of the plot). Magnitude of average speed vector = 2.319, and the maximum speed vector = 2.745 m/s.

WOCSS–OBWIND VECTOR DIFFERENCE 100M STABLE 250M GRID
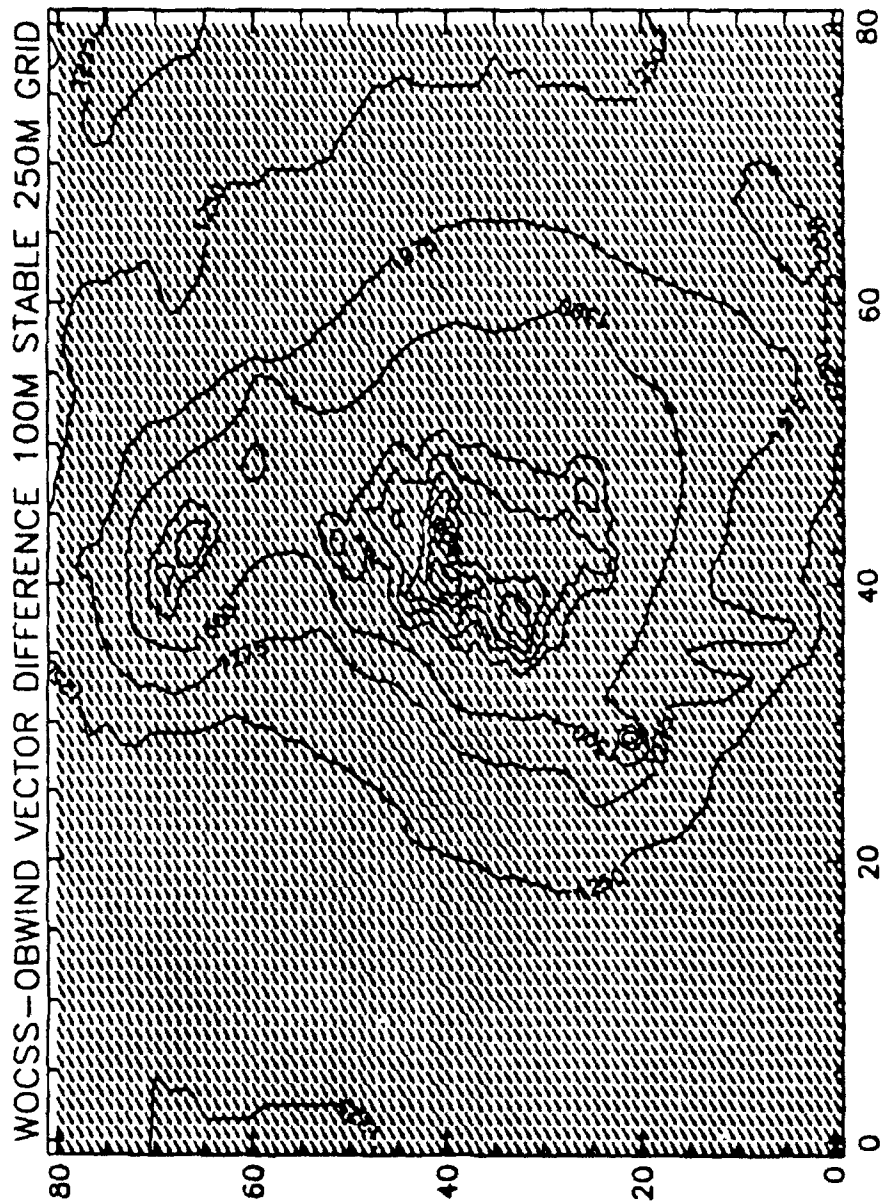
Figure 39. WOCSS–OBWIND 100 m stable case wind vector difference field plot for the WSMR site using 250 X 250 square m grid cells (81 X 81). WSMR site terrain elevation contours are also included (north is located at the top labeled edge of the plot). Magnitude of average vector differences = 1.642 m/s, and the magnitude of the maximum vector difference = 2.077 m/s.

Figure 40 illustrates the completely non-zero WOCSS unstable 10 m layer wind vector field. All unstable WOCSS layer outputs were completely non-zero, resulting from the increased availability of kinetic energy in each layer. Because of the completely free flow nature of the unstable case, graphical plots of results are generally very monotonic and, therefore, provide little additional analysis value over the summary statistics (Tables 16 and 17).

3.1.4 Initialization Data Correlation Test

The final test involved comparing WOCSS and OBWIND layer outputs with varying degrees of surface initialization data (e.g., with n_{max}, $n_{max} - 1$, $n_{max} - 2$, ... surface observations). Generally this testing produced insignificant differences in the WOCSS model outputs. For example, Table 13 indicates stable case WOCSS u component agreement index values were never below 1.0; WOCSS correlation coefficients (Table 14) also never fell below 1.0 in all 10 m stable cases (the level at which all surface observations were actually acquired).

The high WOCSS and OBWIND agreement index and correlation coefficient values produced in this testing served to illustrate the upper range reliability of both the agreement index and correlation coefficient algorithms listed in Appendix B (e.g., agreement index and correlation coefficient values must be ≤ 1.0). However, these results also imply that the version of the WOCSS model being evaluated does not consider supplemental surface based observation data during wind field interpolation operations; apparently only the vertical wind profile data is during these WOCSS operations, which also largely explains why the WOCSS model run-time is significantly less than for the OBWIND model (see Appendix C).
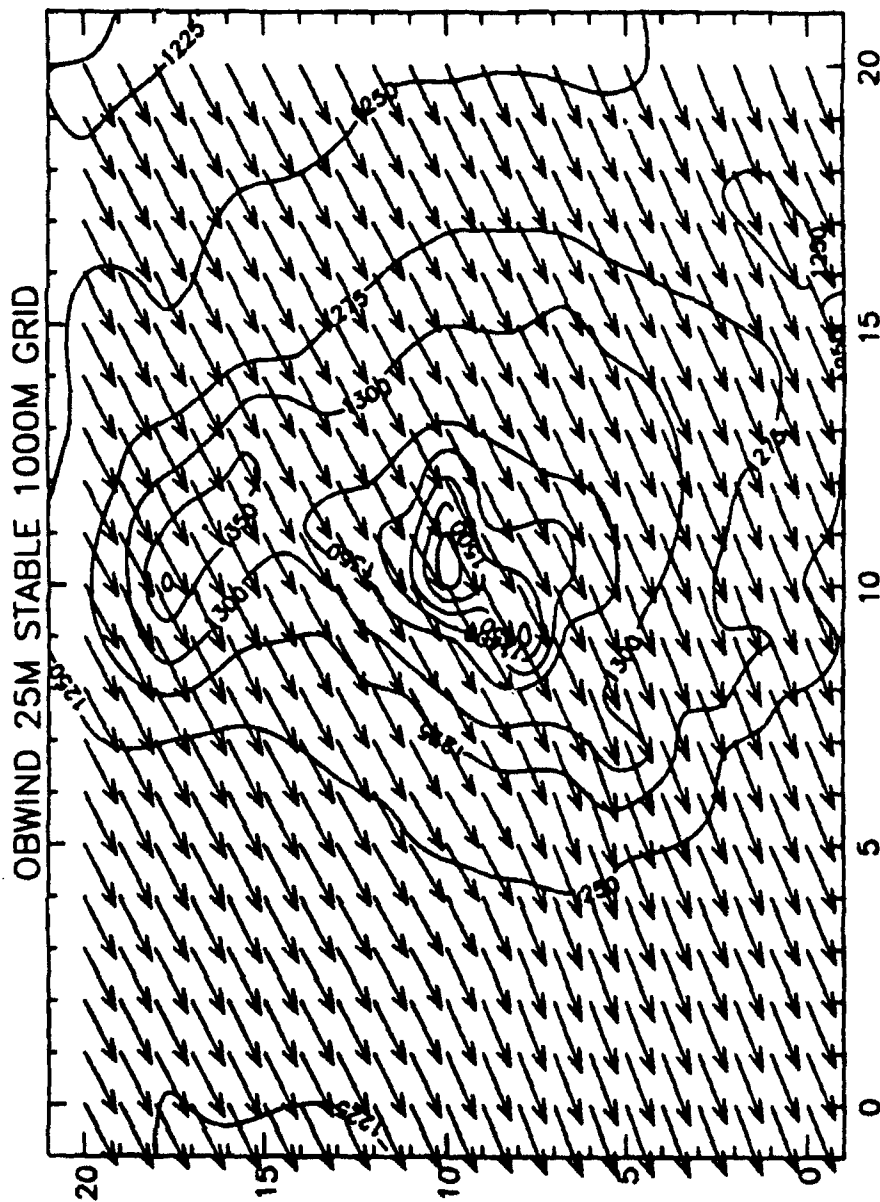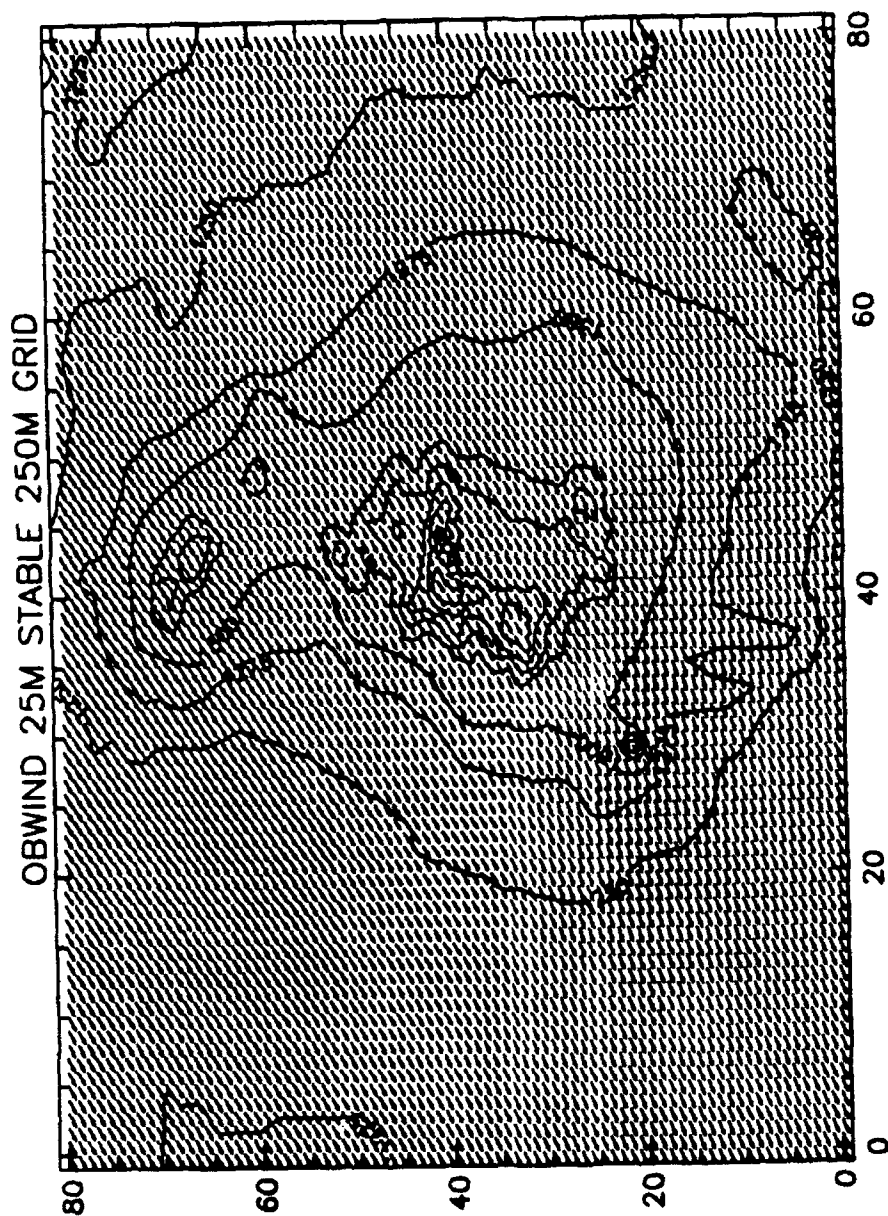
72

WOCSS 10M UNSTABLE 250M GRID

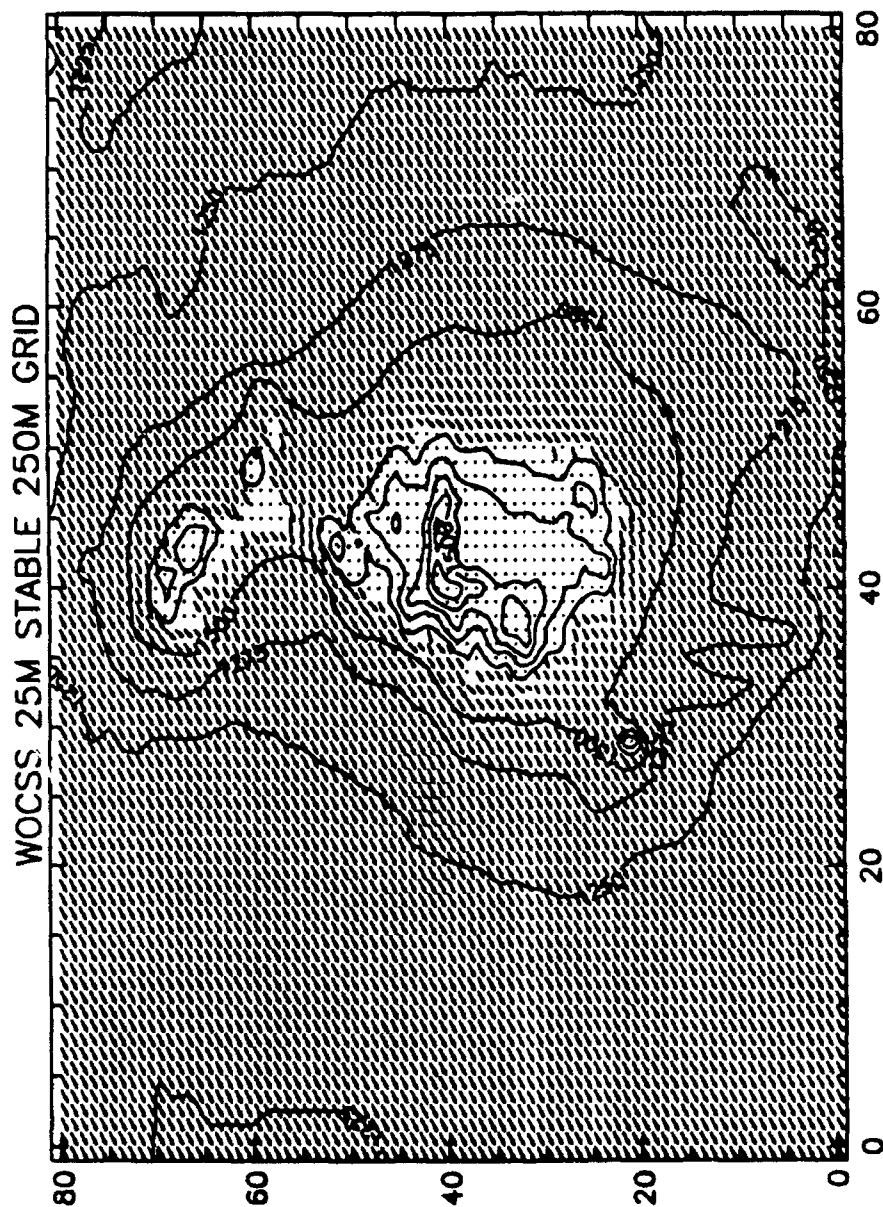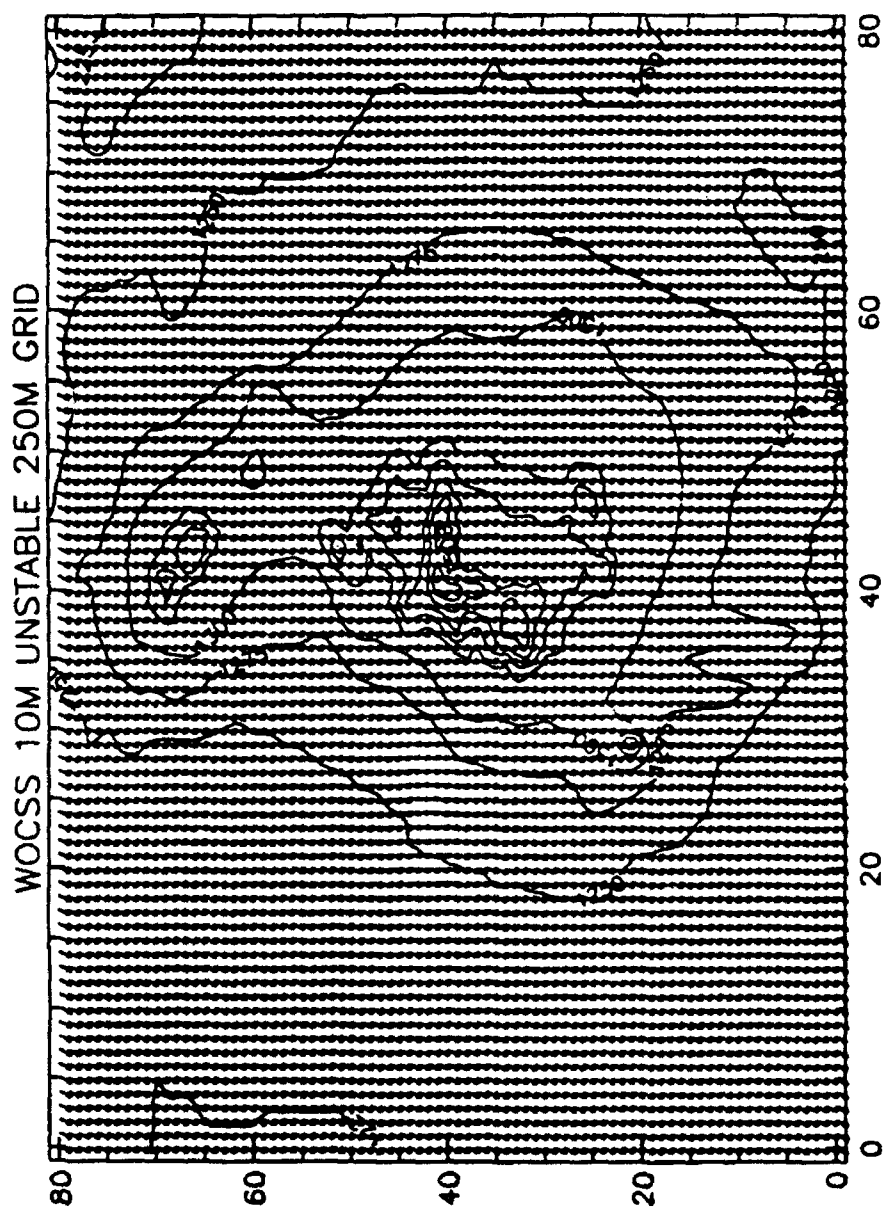Figure 40. WOCSS 10 m unstable case wind vector field plot for the WSMR site using 250 X 250 square m grid cells (81 X 81). WSMR site terrain elevation contours are also included (north is located at the top labeled edge of the plot). Observe that there are no flow restricted spaces at 10 m AGL. Magnitude of average speed vector = 1.160 m/s, and magnitude of maximum speed vector = 1.223 m/s. Mean wind direction is northeasterly.

The WOCSS model's emphasis on weighting upper air data is also largely responsible for the greater root mean square differences in the unstable WSMR cross-model comparisons listed in Tables 9-12 (e.g., in the unstable case, the WOCSS model did not consider the increased low level variability in surface conditions while the OBWIND model did (see Appendix A to contrast the WSMR stable and unstable surface observation variability)).

Variation in the OBWIND 10 m agreement index and correlation coefficient values illustrates several points. The most important point is that the OBWIND model is more responsive to surface initialization data than the WOCSS model. The second point involves the last 2 OBWIND values in Tables 13 and 14; in these 2 cases, agreement index and correlation coefficients are not consistent with each other. This result makes it clear that dependency on a single statistical evaluation would probably be misleading in certain cases.

The basic performance characteristics of both the OBWIND and WOCSS models are evident from review of WSMR results. Therefore, the remaining results will be expanded upon only when necessary and will primarily focus on performance characteristics of the WOCSS model, emphasizing details regarding the site portability aspects of the WOCSS model with respect to variation of terrain complexity.

Table 13. Summary of OBWIND and WOCSS model u component agreement index value (agi) comparisons for the WSMR site 10 m stable case u_n windfield outputs where n is the number of surface observations used to initialize model runs with a 250 m grid. Note that the results presented here were produced by testing each model against itself.

Component Sources	Statistic	OBWIND	WOCSS
u_5-u_5	agi	1.000000	1.000000
u_4-u_5	agi	0.437999	1.000000
u_3-u_5	agi	0.458919	1.000000
u_2-u_5	agi	0.509499	1.000000
u_1-u_5	agi	0.079589	1.000000

Table 14. Summary of u component correlation coefficient value (r) comparisons for the WSMR site 10 m stable case WOCSS and OB-WIND (u_n) windfield outputs where n is the number of surface observations used to initialize model runs with a 250 m grid.

Component Sources	Statistic	OBWIND	WOCSS
u_5-u_5	r	1.000000	1.000000
u_4-u_5	r	0.107765	1.000000
u_3-u_5	r	0.121012	1.000000
u_2-u_5	r	0.099265	1.000000
u_1-u_5	r	0.280620	1.000000

3.2 NTC Results

The NTC site terrain exhibited greater variance than any of the other 3 sites incorporated in this study (see Table 5 and Fig. 10). Therefore, NTC model results represent performance characteristics in the most complex terrain available, the opposite extreme of the WSMR site results.

The influence of change in terrain complexity is reflected in comparing some WSMR and NTC results. For example, under stable conditions 10% (u component) and 78% (v component) lower average correlation coefficients were observed in comparing stable WSMR and NTC results (Tables 9-10 and 15-16). Conversely, other WSMR-NTC result comparisons did not reflect expected responses to terrain complexity. For example, under stable conditions a combined -17% u and v component change in average root mean square differences resulted when respective WSMR root mean sqaure differences were compared to NTC root mean square differences. Also, a +52% combined (u and v component average agreement index value change between the WSMR and NTC results was unexpected. This example is more reaffirmation that studies should not rely on single statistical indices to characterize complex associations.

The influence of change in terrain complexity was more consistently reflected in comparisons between the WSMR and NTC unstable results. For example, under unstable conditions Table 17 and 18 indicate a +44% change took place in the combined u and v component average root mean square differences between respective WSMR and NTC results (Tables 11-12 and 17-18); lower average combined agreement index values (-75%), as well as -50% lower combined average correlation coefficients, were also observed in comparing WSMR and NTC unstable case results.

Significant differences also exist between the NTC stable and unstable results. For example, average combined stable case agreement index values were 29%

higher than the unstable case agreement index values (see Tables 15-16 and 17-18 for respective listings of u and v component agreement index values). Combined u and v component average stable case root mean square differences and correlation coefficients were also, respectively, 169% and 326% lower than in the NTC unstable case, which suggests that it is important to consider both stable and unstable case scenarios in high resolution simulation applications.

As in the WSMR results, often more tangible insight into study results was obtained from analysis of graphical spatial depictions of model outputs. For example, Fig. 41 illustrates the basically monotonic OBWIND model wind speed surface output under stable conditions at 25 m AGL. Figure 42 illustrates WOCSS model results at the same elevation AGL and under the same atmospheric conditions. Note that the majority of the WOCSS 25 m level solution is flow restricted space, which is a dramatic change from the WOCSS response to WSMR terrain at 25 m AGL (see Fig. 34). Figure 43 illustrates the vector differences between the 25 m AGL stable case OBWIND and WOCSS model outputs presented in Figs. 41 and 42 respectively.

Figure 44 demonstrates that, unlike the WSMR unstable case results, the WOCSS model produces significant unstable case flow restricted spaces at 100 m AGL using NTC site terrain. In conjunction with Figs. 41-43, Fig. 44 also demonstrates the WOCSS model's dramatic response to increases in terrain complexity (when compared to the WSMR Fig. 34 results).

Table 15. Summary u component windfield statistics for NTC site 10, 25, and 100 m stable case OBWIND (u_o) and WOCSS (u_w) windfield outputs (rms=Root Mean Square Difference, agi=Agreement Index, and r=Correlation Coefficient).

Component Sources	Statistic	100m grid	250m grid	1000m grid
u_o-u_w	rms 10m	0.565917	0.568957	0.581670
u_o-u_w	rms 25m	0.313170	0.315009	0.353918
u_o-u_w	rms 100m	0.698934	0.702900	0.765826
u_o-u_w	agi 10m	0.406613	0.384603	0.281691
u_o-u_w	agi 25m	0.323927	0.301601	0.221548
u_o-u_w	agi 100m	0.198802	0.187169	0.129889
u_o-u_w	r 10m	0.011039	0.011241	-0.004228
u_o-u_w	r 25m	0.139170	0.160142	0.206624
u_o-u_w	r 100m	0.134276	0.211968	0.206624

Table 16. Summary v component windfield statistics for NTC site 10, 25, and 100 m stable case OBWIND (v_o) and WOCSS (v_w) windfield outputs (rms=Root Mean Square Difference, agi=Agreement Index, and r=Correlation Coefficient).

Component Sources	Statistic	100m grid	250m grid	1000m grid
v_o-v_w	rms 10m	0.583754	0.586630	0.592768
v_o-v_w	rms 25m	0.782561	0.799898	0.817913
v_o-v_w	rms 100m	1.096843	1.118825	1.185041
v_o-v_w	agi 10m	0.075915	0.049379	0.015383
v_o-v_w	agi 25m	0.028634	0.018969	0.018897
v_o-v_w	agi 100m	0.033146	0.044610	0.116267
v_o-v_w	r 10m	-0.010592	-0.008645	0.025160
v_o-v_w	r 25m	0.016418	-0.183402	-0.183583
v_o-v_w	r 100m	0.095321	-0.074198	-0.093201

Table 17. Summary u component windfield statistics for NTC site 10, 25, and 100 m unstable case OBWIND (u_o) and WOCSS (u_w) windfield outputs (rms=Root Mean Square Difference, agi=Agreement Index, and r=Correlation Coefficient).

Component Sources	Statistic	100m grid	250m grid	1000m grid
u_o-u_w	rms 10m	0.548071	0.558534	0.572248
u_o-u_w	rms 25m	0.681466	0.702550	0.733199
u_o-u_w	rms 100m	2.114018	2.150267	2.755057
u_o-u_w	agi 10m	0.324205	0.296959	0.198717
u_o-u_w	agi 25m	0.147062	0.144025	0.157402
u_o-u_w	agi 100m	0.061410	0.060150	0.052337
u_o-u_w	r 10m	0.008774	0.009522	-0.008320
u_o-u_w	r 25m	0.201323	0.237528	0.331363
u_o-u_w	r 100m	0.072375	0.160770	0.014375

Table 18. Summary v component windfield statistics for NTC site 10, 25, and 100 m unstable case OBWIND (v_o) and WOCSS (v_w) windfield outputs (rms=Root Mean Square Difference, agi=Agreement Index, and r=Correlation Coefficient).

Component Sources	Statistic	100m grid	250m grid	1000m grid
v_o-v_w	rms 10m	1.507580	1.515548	1.514612
v_o-v_w	rms 25m	2.218328	2.252696	2.228796
v_o-v_w	rms 100m	3.510933	3.563609	4.278866
v_o-v_w	agi 10m	0.067367	0.054279	0.019853
v_o-v_w	agi 25m	0.035105	0.024261	0.051423
v_o-v_w	agi 100m	0.034248	0.049633	0.162873
v_o-v_w	r 10m	0.009106	0.011506	0.027654
v_o-v_w	r 25m	0.364159	0.170301	0.019495
v_o-v_w	r 100m	0.262189	0.171201	0.752704

25M OBWIND S U+V SPEED 250M GRID
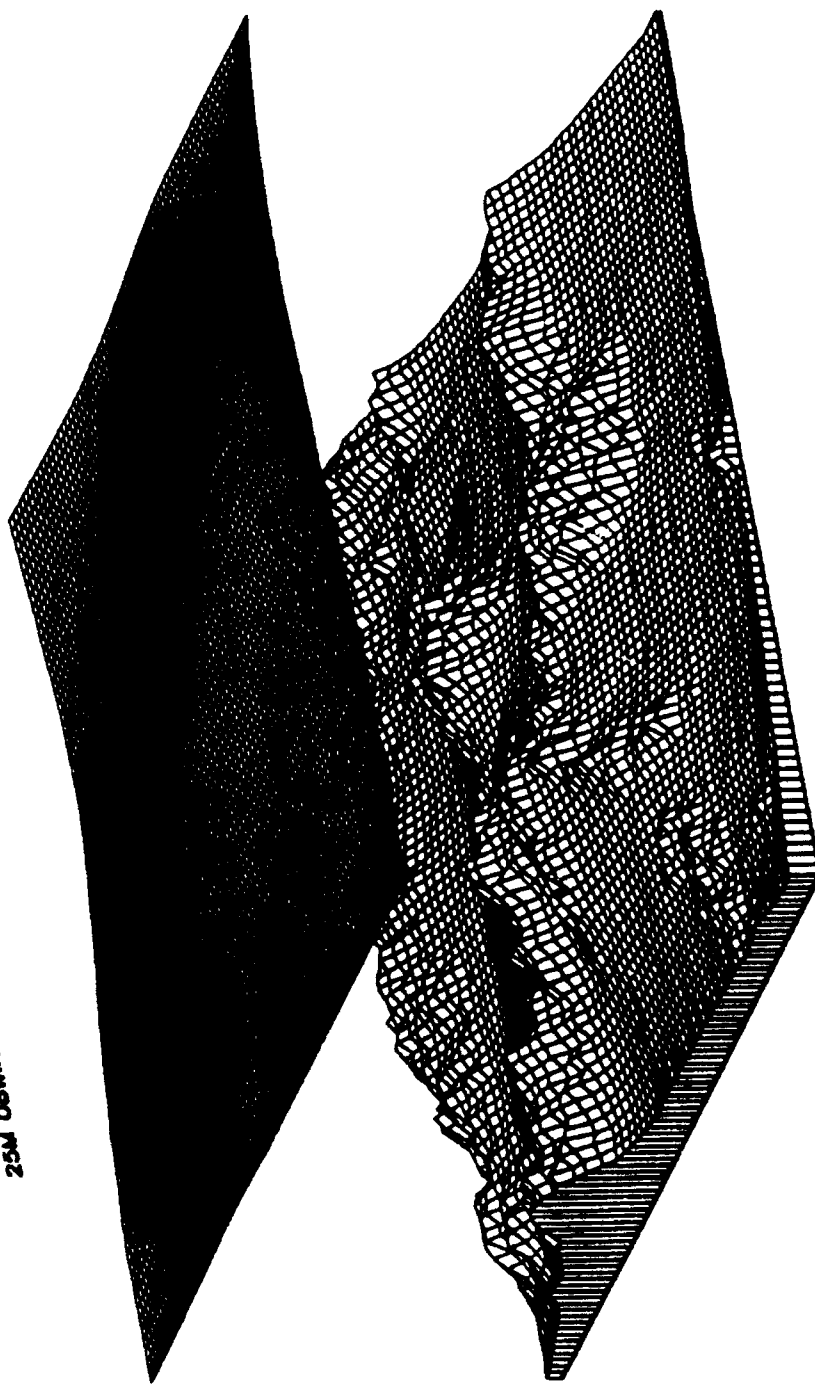
Figure 41. OBWIND 25 m stable case wind speed plot for the NTC site using 250 X 250 square m grid cells (81 X 81). NTC site terrain elevation is plotted below the speed surface plot (north is located at the top labeled edge of the plotted regions). Minimum, average, and maximum speed values are, respectively, 0.705, 0.754, and 0.942 m/s, where speed increases along the vertical plot axis.

80

25M WOCSS S U+V SPEED 250M GRID
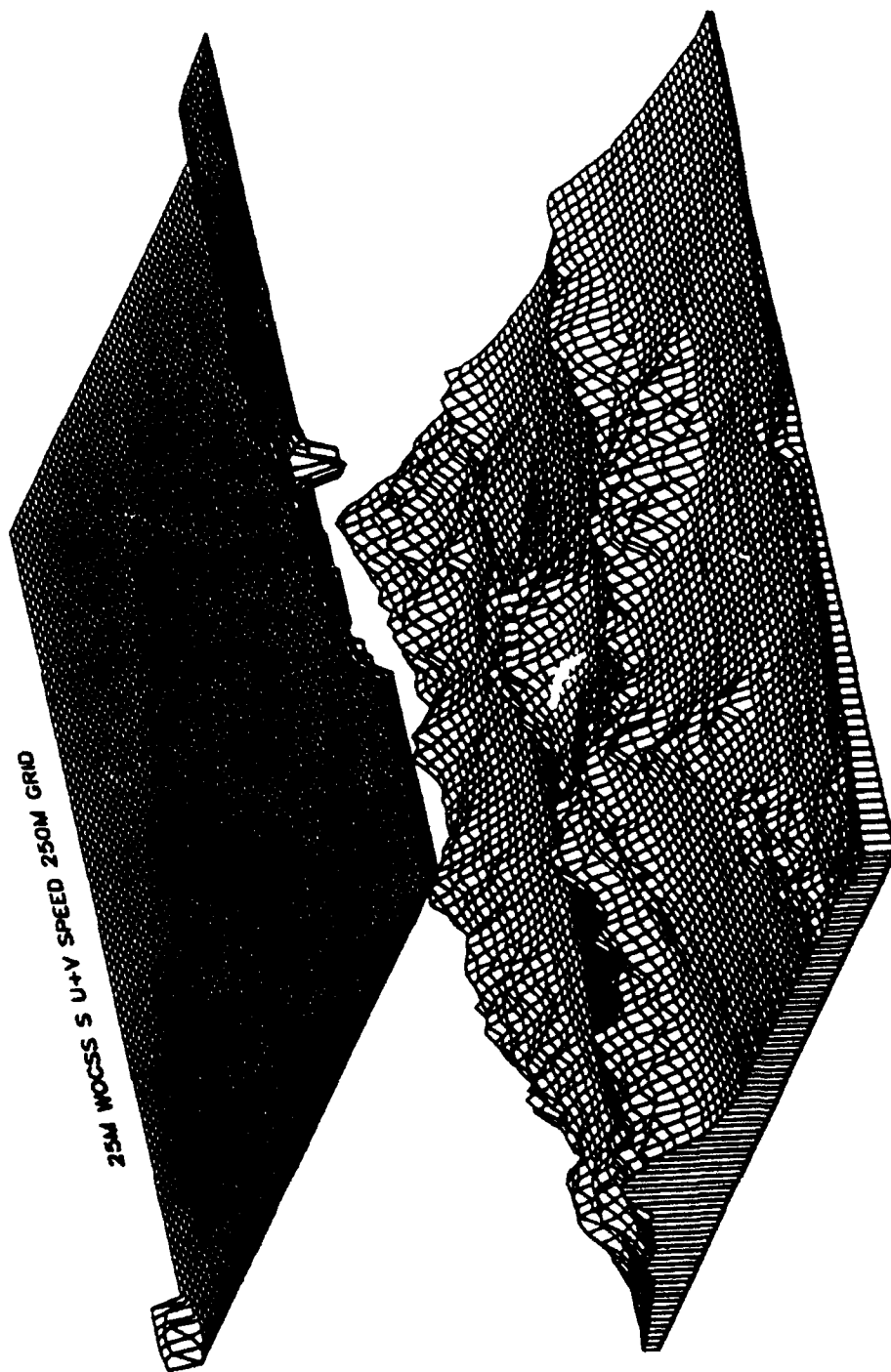
Figure 42. WOCSS 25 m stable case wind speed plot for the NTC site using 250 X 250 square m grid cells (81 X 81). NTC site terrain elevation is plotted below the speed surface plot (north is located at the top labeled edge of the plotted regions). Minimum, average, and maximum speed values are, respectively, 0.000, 0.195, and 2.197 m/s, where speed increases along the vertical plot axis.
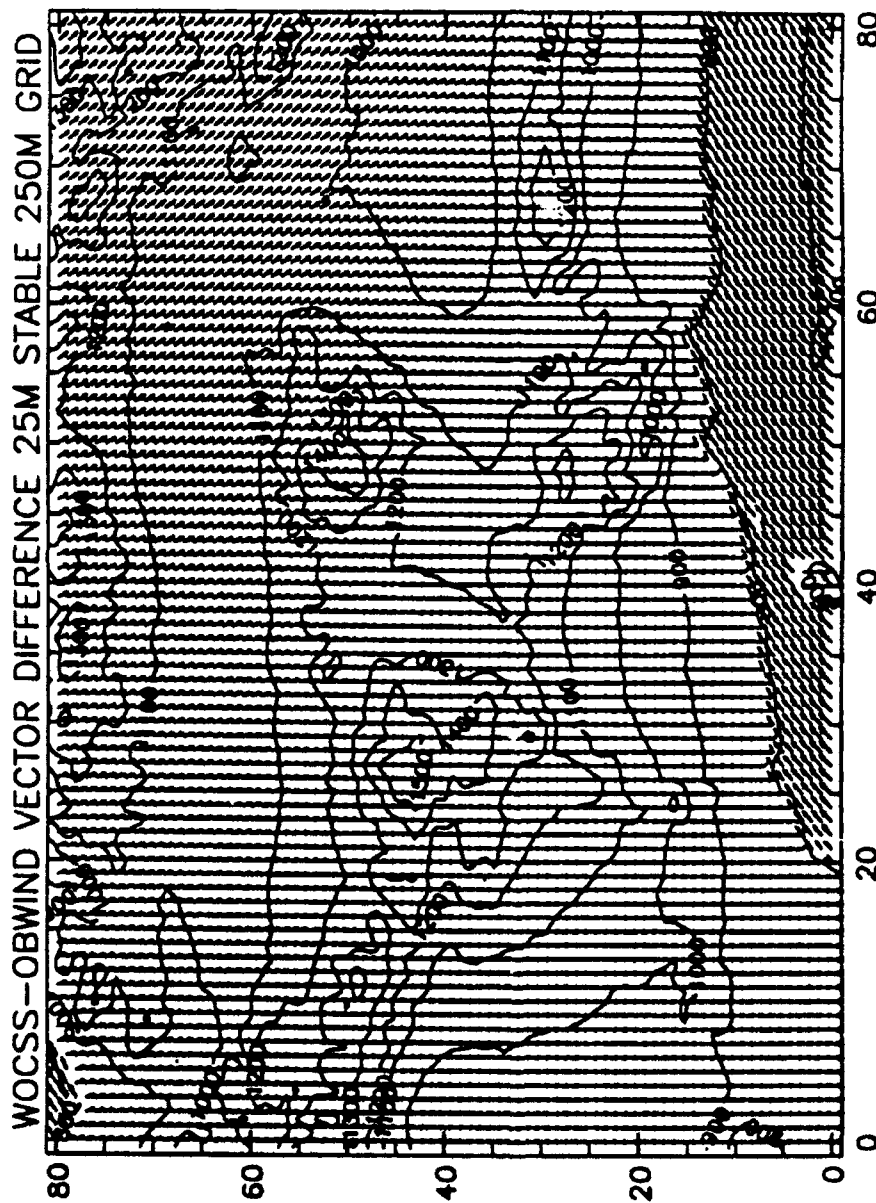
Figure 43. WOCSS-OBWIND 25 m stable case wind vector differences plot for the NTC site using 250 X 250 square m grid cells (81 X 81). NTC site terrain elevation contours are also included (north is located at the top labelled edge of the plot). Magnitude of average vector differences = 0.802 m/s, and magnitude of maximum vector difference = 1.469 m/s.

WOCSS U U+V SPEED 250M GRID

Figure 44. WOCSS 100 m stable case wind speed plot for the NTC site using 250 X 250 square m grid cells (81 X 81). NTC site terrain elevation is plotted below the speed surface plot (north is located at the top labeled edge of the plotted regions). Minimum, average, and maximum speed values are, respectively, 0.000, 1.141, and 3.344 m/s, where speed increases along the vertical plot axis.

83

3.3 Project WIND Results

The Project WIND site terrain exhibited intermediate variance compared to the NTC and WSMR sites (see Table 5 and Fig. 10). Therefore, Project WIND model results represent performance characteristics of intermediate terrain complexity, and the influence of change in terrain complexity is reflected in comparing some WSMR and Project WIND results. For example, under stable conditions a -47% combined **u** and **v** component change in average correlation coefficients was observed in comparing stable WSMR and Project WIND results (Tables 9-10 and 19-20).

However, as in the WSMR-NTC stable case comparisons, other results did not reflect expected responses to terrain complexity. For example, under stable conditions a combined -28% **u** and **v** component change in average root mean square differences resulted when respective WSMR root mean square differences were compared to corresponding Project WIND root mean square differences. Also, a +81% combined (**u** and **v**) component average agreement index value change between the WSMR and Project WIND results was unexpected, and not well correlated with changes in terrain.

Mixed results were also obtained in WSMR-Project WIND unstable case comparisons. For example, under unstable conditions Table 19 and 20 indicates that average combined root mean square differences between WSMR (Tables 11-12) and Project WIND results decreased by 22%, average combined agreement index values also increased by 62%, and average combined correlation coefficients decreased by 20%.

Noteworthy differences also exist between Project WIND stable and unstable results. For example, combined average Project WIND agreement index values were 50% higher in unstable case (Tables 19-20 and 21-22). Combined average u and v component unstable case root mean square differences and correlation coefficients were also respectively 67% and 169% greater than in the Project WIND stable case.

The improved agreement index and correlation coefficient values in the Project WIND unstable cases are attributed largely to the decrease in flow restricted space predicted by the WOCSS model under unstable conditions (e.g., in the WSMR unstable case there was no predicted flow restriction at 10, 25, or 100 m AGL (see Fig. 40)). This response is largely due to the increased amount of kinetic energy available in unstable case initialization data (see Tables A5-A8 in Appendix A).

As in the WSMR and NTC cases, graphical spatial depictions revealed many other interesting results. For example, Fig. 45 illustrates a 10 m AGL stable case OBWIND speed surface output. Note the speed maximum in the southeast corner of the plot; it is associated with higher velocity initialization data located in the vicinity of station S-4 (see Table A7.1 in Appendix A). Conversely, Fig. 46 illustrates the WOCSS model output at the same elevation AGL and under the same conditions. Most of the WOCSS solution at this level is flow restricted space, except for several regions largely concentrated in the southwest corner of the Project WIND study area, which is associated with a low level plane region.

Figure 47 depicts the 25 m AGL OBWIND stable case output, and it emphasizes a speed maximum region in the northeast portion of the Project WIND study area. However, the corresponding WOCSS model output (Fig. 48) presents a very different prediction solution: the OBWIND speed maximum area is largely predicted to be a flow restricted space by the WOCSS model (also illustrated in the 25 m vector difference plot, Fig, 49).

Table 19. Summary u component windfield statistics for Project WIND site 10, 25, and 100 m stable case OBWIND (u_o) and WOCSS (u_w) windfield outputs (rms=Root Mean Square Difference, agi=Agreement Index, and r=Correlation Coefficient).

Component Sources	Statistic	100m grid	250m grid	1000m grid
u_o-u_w	rms 10m	0.646944	0.646271	0.641437
u_o-u_w	rms 25m	0.443715	0.438451	0.412346
u_o-u_w	rms 100m	0.531459	0.438451	0.522843
u_o-u_w	agi 10m	0.299979	0.284134	0.211191
u_o-u_w	agi 25m	0.241593	0.230301	0.192204
u_o-u_w	agi 100m	0.217753	0.208817	0.178661
u_o-u_w	r 10m	-0.059478	-0.061459	-0.082292
u_o-u_w	r 25m	-0.141748	-0.064517	0.048671
u_o-u_w	r 100m	-0.051521	-0.014800	0.038804

Table 20. Summary v component windfield statistics for Project WIND site 10, 25, and 100 m stable case OBWIND (v_o) and WOCSS (v_w) windfield outputs (rms=Root Mean Square Difference, agi=Agreement Index, and r=Correlation Coefficient).

Component Sources	Statistic	100m grid	250m grid	1000m grid
v_o-v_w	rms 10m	0.709004	0.708661	0.705502
v_o-v_w	rms 25m	0.500635	0.499107	0.490054
v_o-v_w	rms 100m	0.839217	0.844008	0.853185
v_o-v_w	agi 10m	0.291156	0.279760	0.232102
v_o-v_w	agi 25m	0.202086	0.222518	0.339326
v_o-v_w	agi 100m	0.151989	0.179358	0.322698
v_o-v_w	r 10m	0.114776	0.113705	0.098359
v_o-v_w	r 25m	0.219427	0.269325	0.278671
v_o-v_w	r 100m	0.152517	0.198306	0.600944

Table 21. Summary u component windfield statistics for Project WIND site 10, 25, and 100 m unstable case OBWIND (u_o) and WOCSS (u_w) windfield outputs (rms=Root Mean Square Difference, agi=Agreement Index, and r=Correlation Coefficient).

Component Sources	Statistic	100m grid	250m grid	1000m grid
u_o-u_w	rms 10m	0.529500	0.528440	0.525441
u_o-u_w	rms 25m	0.525855	0.520805	0.515802
u_o-u_w	rms 100m	1.020713	1.022311	1.041712
u_o-u_w	agi 10m	0.399459	0.408845	0.437897
u_o-u_w	agi 25m	0.417741	0.425086	0.474907
u_o-u_w	agi 100m	0.271813	0.270955	0.310996
u_o-u_w	r 10m	0.210885	0.175854	0.090427
u_o-u_w	r 25m	0.147367	0.224680	0.361363
u_o-u_w	r 100m	0.097640	0.186825	0.444199

Table 22. Summary v component windfield statistics for Project WIND site 10, 25, and 100 m unstable case OBWIND (v_o) and WOCSS (v_w) windfield outputs (rms=Root Mean Square Difference, agi=Agreement Index, and r=Correlation Coefficient).

Component Sources	Statistic	100m grid	250m grid	1000m grid
v_o-v_w	rms 10m	0.864071	0.877027	0.928930
v_o-v_w	rms 25m	0.890080	0.876337	0.763384
v_o-v_w	rms 100m	2.160367	2.182069	2.204209
v_o-v_w	agi 10m	0.395331	0.358020	0.198166
v_o-v_w	agi 25m	0.380815	0.425353	0.630086
v_o-v_w	agi 100m	0.134768	0.169963	0.334250
v_o-v_w	r 10m	0.280300	-0.029332	0.299044
v_o-v_w	r 25m	-0.011086	0.132761	0.488362
v_o-v_w	r 100m	0.031702	0.477423	0.848978
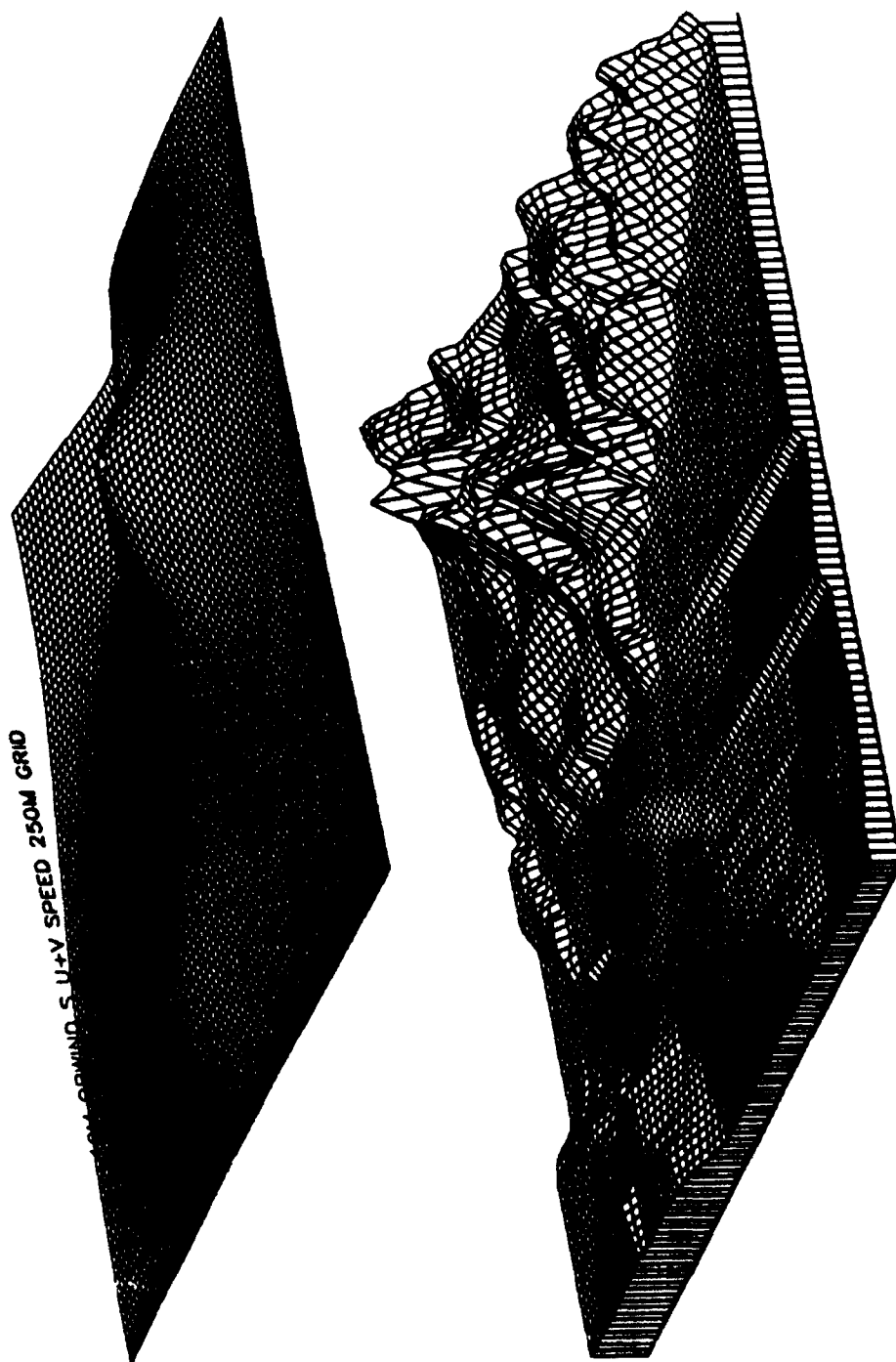
Figure 45. OBWIND 10 m stable case wind speed plot for the Project WIND site using 250 X 250 square m grid cells (81 X 81). Project WIND site terrain elevation is plotted below the speed surface plot (north is located at the top labeled edge of the plotted regions). Minimum, average, and maximum speed values are, respectively, 0.415, 0.950, and 1.355 m/s, where speed increases along the vertical plot axis.
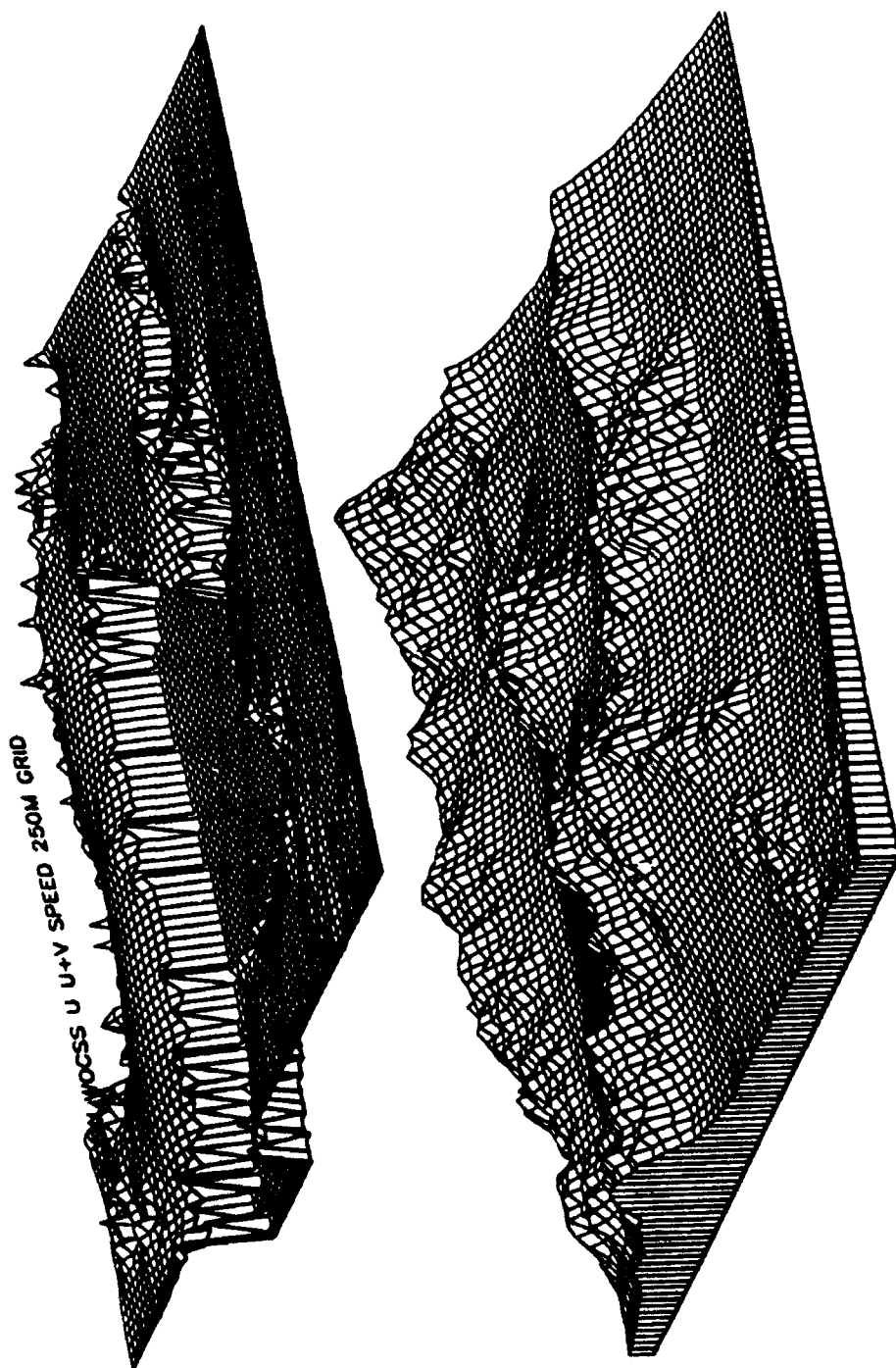
10M WOCSS S U+V SPEED 250M GRID
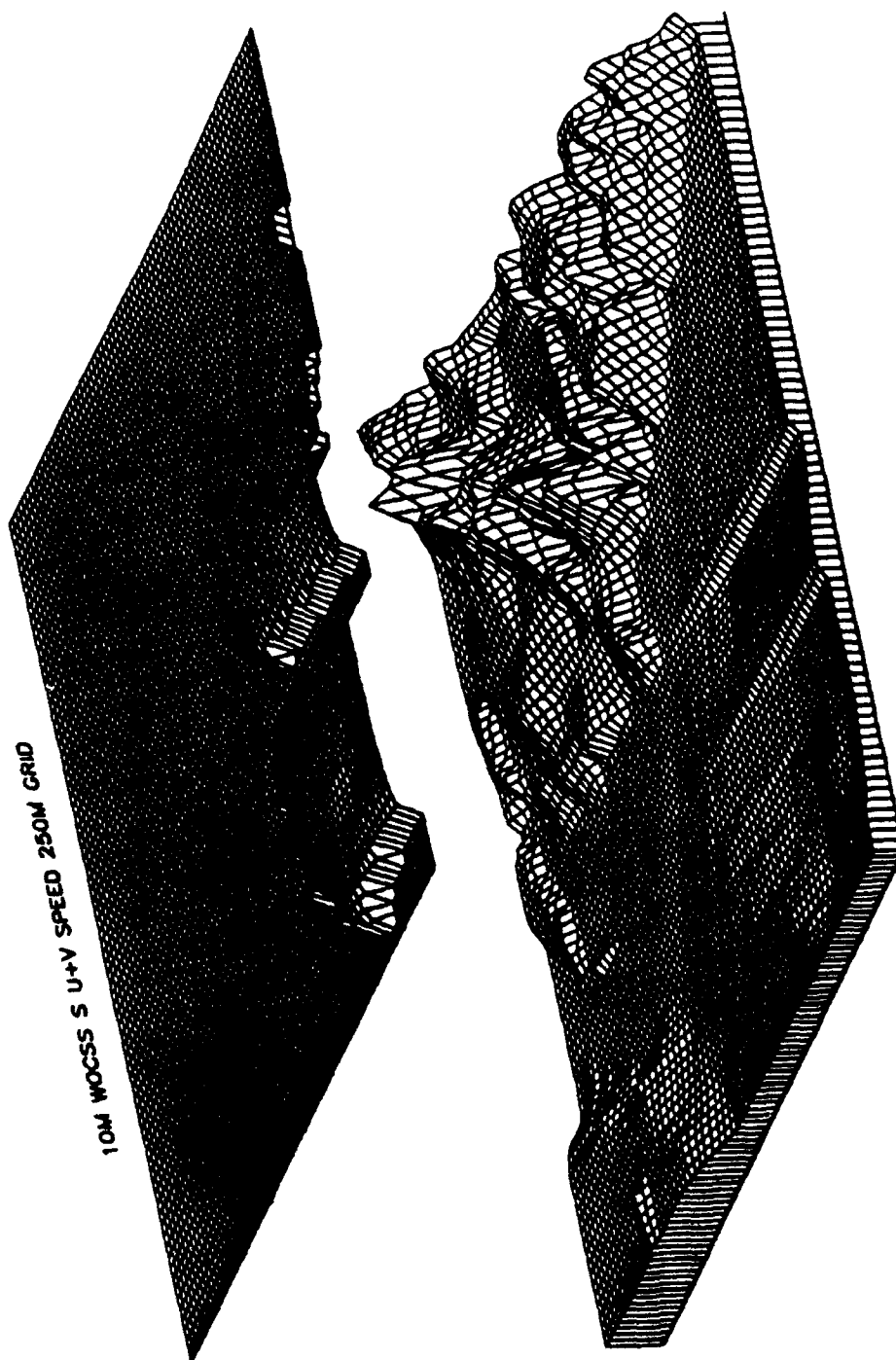
Figure 46. WOCSS 10 m stable case wind speed plot for the Project WIND site using 250 X 250 square m grid cells (81 X 81). Project WIND site terrain elevation is plotted below the speed surface plot (north is located at the top labeled edge of the plotted regions). Minimum, average, and maximum speed values are, respectively, 0.000, 0.125, and 1.066 m/s, where speed increases along the vertical plot axis.

25M OBWIND S U+V SPEED 250M GRID
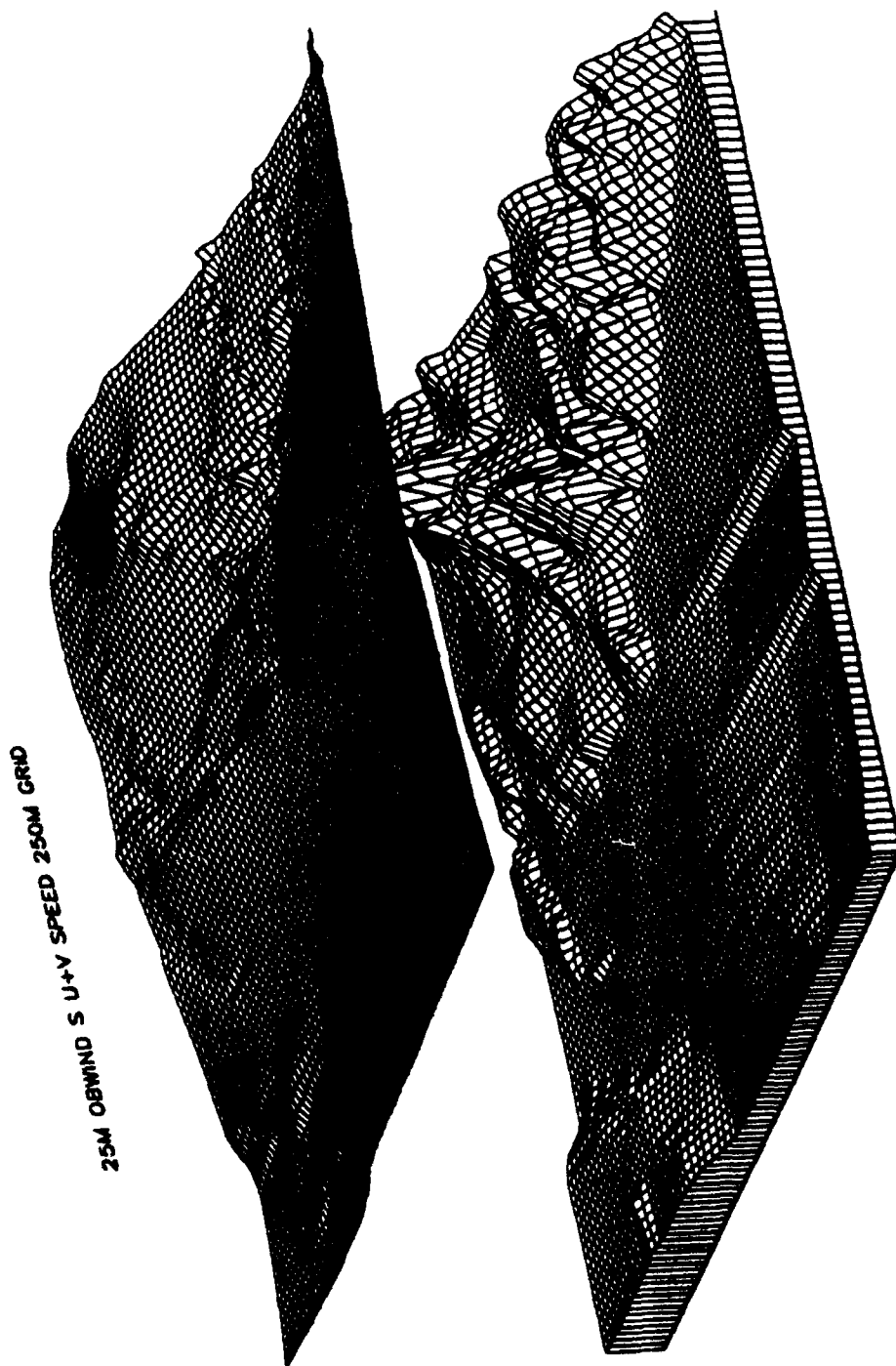
Figure 47. OBWIND 25 m stable case wind speed plot for the Project WIND site using 250 X 250 square m grid cells (81 X 81). Project WIND site terrain elevation is plotted below the speed surface plot (north is located at the top labeled edge of the plotted regions). Minimum, average, and maximum speed values are, respectively, 0.719, 0.883, and 1.061 m/s, where speed increases along the vertical plot axis.
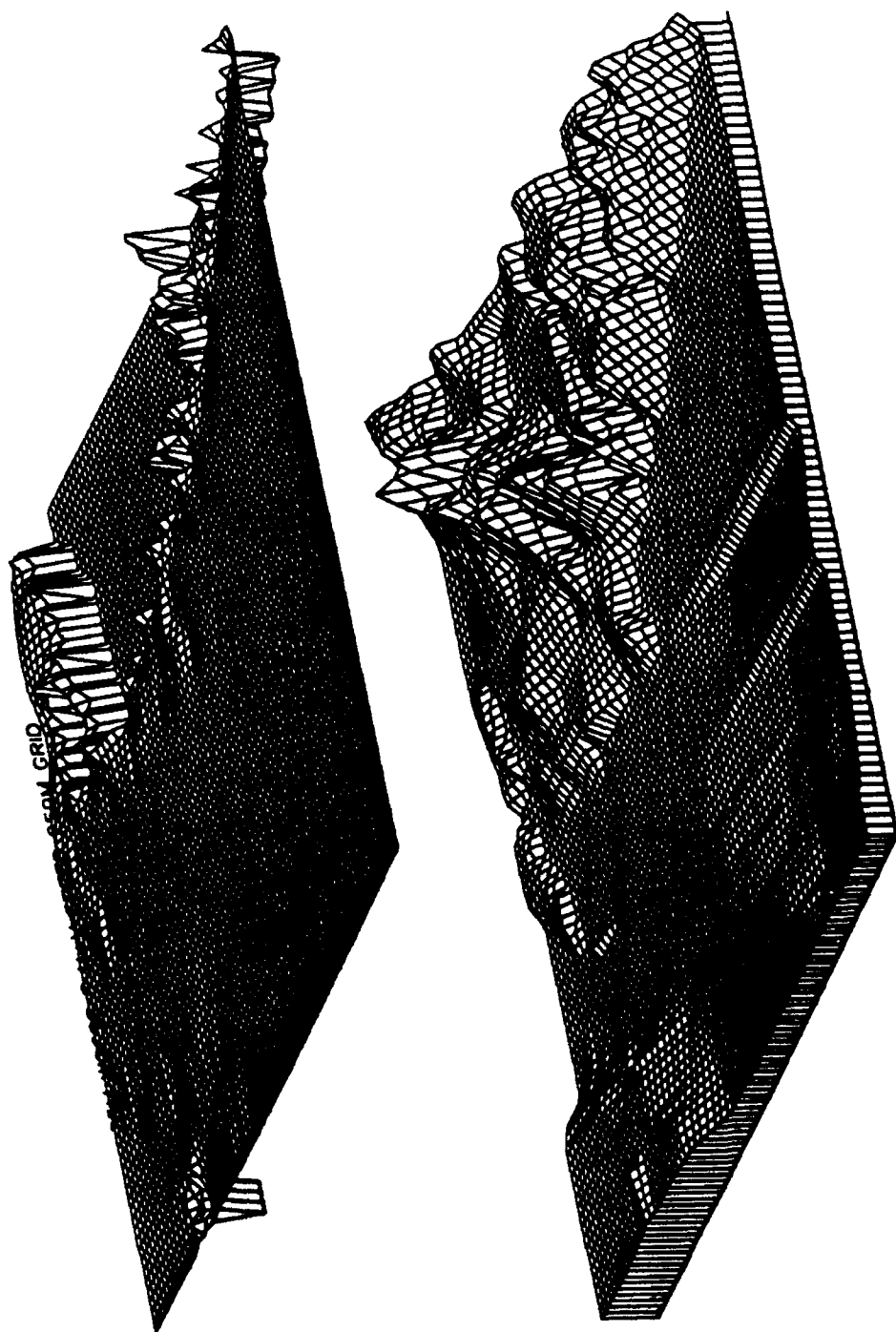
Figure 48. WOCSS 25 m stable case wind speed plot for the Project WIND site using 250 X 250 square m grid cells (81 X 81). Project WIND site terrain elevation is plotted below the speed surface plot (north is located at the top labeled edge of the plotted regions). Minimum, average, and maximum speed values are, respectively, 0.000, 0.941, and 1.560 m/s, where speed increases along the vertical axis.
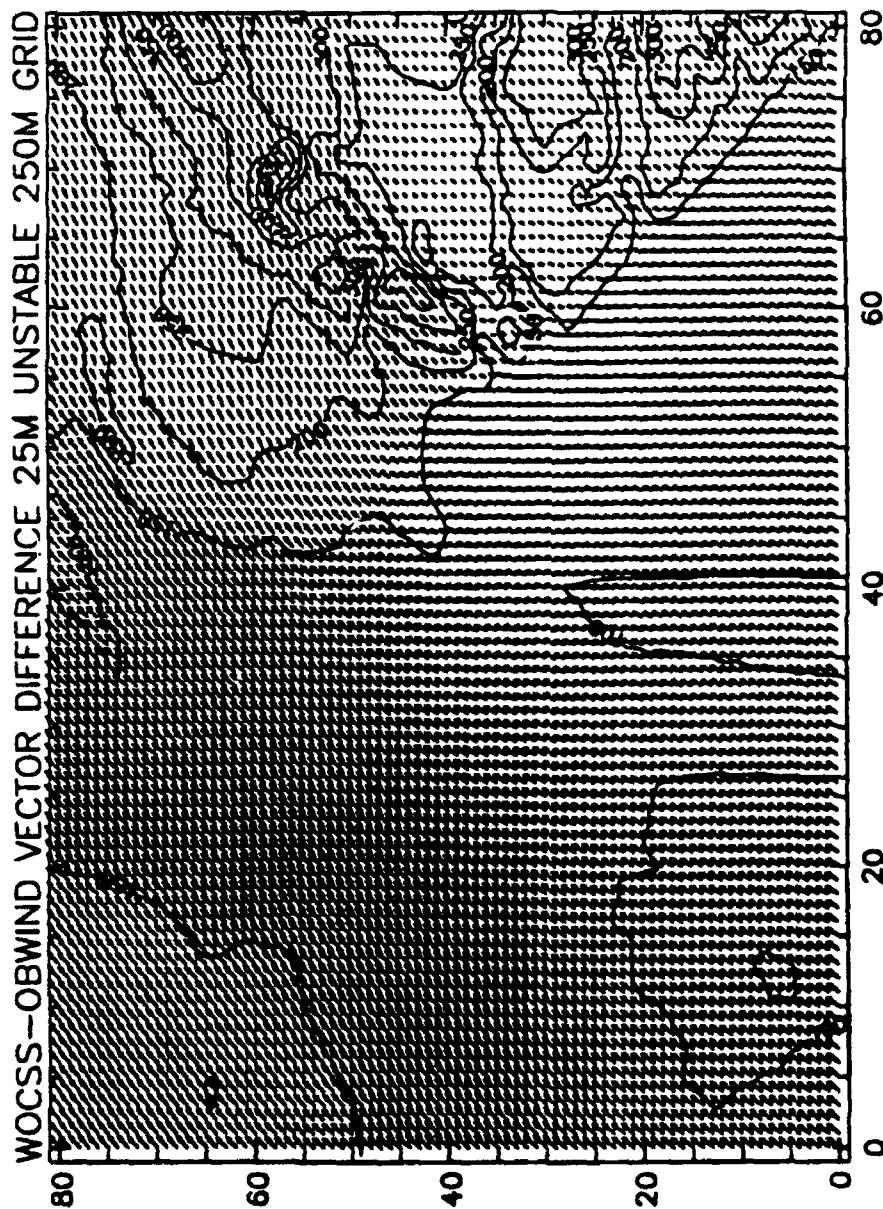
Figure 49. WOCSS-OBWIND 25 m stable case wind vector differences plot for the Project WIND site using 250 X 250 square m grid cells (81 X 81). Project WIND site terrain elevation contours are also included (north is located at the top labeled edge of the plot). Magnitude of average vector differences = 0.429 m/s, and magnitude of maximum vector difference = 1.040 m/s..

3.4 Czechoslovakian Results

The Czechoslovakian site terrain had intermediate variance compared to the NTC and WSMR sites (see Table 5 and Fig. 10). Therefore, the Czechoslovakian model results, similiar to Project WIND Results, also represent performance characteristics in transitional terrain complexity. However, the Czechoslovakian results represent a completely different set of initialization conditions: these results were produced under sparse (single point), user specified initialization conditions, where no actual observation data was available. This exercise was primarily implemented to study sparse initialization behavior of the WOCSS model; therefore, the following results only address WOCSS model performance.

An extreme condition of sparse data initialization, typical of the oversimplified conditions presently used to initialize various atmospheric transport processes in a number of U.S. Army applications, was employed to initialize Czech. WOCSS model runs: only one wind speed and direction profile was used to initialize each WOCSS model run. The same wind speed and direction profile was used to initialize the WOCSS model from 2 separate locations having the same elevation (see Appendix A). A WOCSS model run was executed for each separate location (stations S-1 and S-2) under exactly the same stable and unstable conditions, which produced the following inner WOCSS model comparison results.

For example, Tables 23-24 and 25-26 are the respective u and v component summary statistics for the stable and unstable case comparisons of stations S-1 and S-2 (see Appendix A) WOCSS model results. Results presented in Tables 23-26 are significantly different from the OBWIND-WOCSS summary statistics for the WSMR, NTC, and Project WIND sites (Tables 9-12, 15-18, and 19-22, respectively). Yet root mean square differences are significantly lower for the Czech. inner WOCSS model comparisons, suggesting little difference exists between S-1 and S-2 results; this result is complemented by relatively high agreement index and correlation coefficient values (consistently at 25 and 100 m AGL).

However, despite the significant level of agreement indicated by the S-1/S-2 WOCSS results in Tables 23-26, agreement and correlation is not consistent (e.g., see Table 26) and suggests that important, layer selective differences can result when initializing a complex terrain wind model with exactly the same data from different points over the simulated terrain space. This result demonstrates one of the flaws in assuming a single mean wind speed and direction over a complex terrain space; in other words, assumptions of oversimplified mean wind speed and direction over a complex terrain space are functionally dependent on the initialization location within the terrain space.

Further analysis of these results suggest that even when consideration of the functional dependence on initialization location is made, the assumption of using a mean wind speed and direction over a complex terrain space is unrealistic. For example, Figs. 50 and 51 represent the spatial variation in 10 and 25 m AGL WOCSS speed surfaces for station S-1 (see Appendix A) under stable conditions. Notice the dramatic variation in flow restricted space between the 10 and 25 m flow surfaces in Figs. 50 and 51.

Figure 52 illustrates the WOCSS vector differences between stations S-1 and S-2 under stable conditions; significant vector differences are observed over a widely distributed area, not just at initialization locations. Figures 53 and 54 also illustrate the significant WOCSS variation produced at 25 m AGL when station S-2 was initialized, respectively, with s'able and unstable data, and the differences between station S-2 and station S-1 at 25 m AGL under unstable conditions (see Appendix A) are plotted in Fig. 55.

Figure 56 illustrates the magnitude of the wind speeds associated with the vector differences indicated in Fig. 55. Both Figs. 55 and 56 suggest that unstable case differences were very dependent on placement of initialization data in the modeled Czechoslovakian space (see Appendix A for locations of S-1 and S-2). Because terrain influence on the unstable case differences is minor (compared

94

to the effect of initialization data placement), there appears to be little physical significance in the unstable case results. However, the distribution of vector differences in the stable case comparison (see Fig. 52), where average wind speeds at 25 m AGL were approximately 80% less than average unstable case wind speeds, appears to be much more influenced by terrain effects. For example, stable case speed differences, as illustrated in Fig. 57, appear to be closely associated with the occurrence of rugged terrain areas, which required further analysis.

For example, terrain slope, the rate at which terrain elevation, z, changes in the horizontal

$$dz = \left(\frac{\partial z}{\partial x}\right) dx + \left(\frac{\partial z}{\partial y}\right) dy \tag{15}$$

and the change in slope

$$d^2z = \left(\frac{\partial^2 z}{\partial x^2}\right) dx^2 + \left(\frac{\partial^2 z}{\partial y^2}\right) dy^2 \tag{16}$$

were solved for over the selected 20×20 km^2 Czechoslovakian terrain in an attempt to infer physical significance in the stable case result differences illustrated in Figs. 52 and 57. The dz and d^2z values were translated, respectively, into θ and $d\theta$ elevation angles above the $x - y$ tangent plane.

Figure 58(a) and 58(b) illustrate, respectively, the θ and $d\theta$ solutions for the Cech. site, which agree well with the original terrain elevation data depicted in Fig. 7(b) – for example, low slope, plain areas within the Cechoslovakian terrain site are inversely correlated with the frequency of occurrence of plotted contours in Fig. 58.

In analyzing where stable wind speed differences were ≥ 1.0 m/s, it was dis-covered that 100% of these differences occurred between the 475-525 m terrain elevation zones within the 20 × 20 km^2 Czech. site. These zones were repre-sentative of the Czech. site's mean elevation (e.g., the minimum, mean, and maximum terrain elevation ASL was, respectively, 374.0, 488.9, and 746.0 m). Analysis was then focused on the correlation between this occurrence of wind speed differences ≥ 1.0, θ, and $d\theta$ (see Table 27).

Table 28 indicates that approximately 100% of these speed differences, ≥ 1.0 m/s between the 475-525 m ASL terrain zones, occurred along relatively low to moderate slopes (0° − 12°). Table 29 presents further analysis results that indicated a significant amount (57%) of the wind speed differences ≥ 1.0 m/s also occurred in the vicinity of moderate changes in slope (4° − 8°).

Figure 59 illustrates the widely distributed and selective correlation between θ, $d\theta$, and wind speed differences ≥ 0.25 m/s. As Tables 28 and 29 suggest, significant wind speed differences do not generally coincide with steepest slopes or changes in slope, but Fig. 59 does show that significant wind differences are closely coupled to areas where terrain slope varies frequently. Figures 57 and 59, therefore, appear to illustrate a physically significant Czech. site WOCSS model response under the given sparse data stable conditions, where wind speeds were < 3.0 m/s; and this particular WOCSS model result demonstrates the unrealistic value in assuming a single wind speed and direction to be representative, for example, in high resolution atmospheric transport applications over 20 km × 20 km moderately complex terrain areas.

Table 23. Summary u component windfield statistics for Czech. site 10, 25, and 100 m stable case WOCSS ($u_{station1}$) and WOCSS ($u_{station2}$) windfield outputs (rms=Root Mean Square Difference, agi = Agreement Index, and r=Correlation Coefficient).

Component Sources	Statistic	250m grid
$u_{sta.1}$-$u_{sta.2}$	rms 10m	0.002996
$u_{sta.1}$-$u_{sta.2}$	rms 25m	0.086433
$u_{sta.1}$-$u_{sta.2}$	rms 100m	0.029136
$u_{sta.1}$-$u_{sta.2}$	agi 10m	0.999565
$u_{sta.1}$-$u_{sta.2}$	agi 25m	0.959164
$u_{sta.1}$-$u_{sta.2}$	agi 100m	0.896098
$u_{sta.1}$-$u_{sta.2}$	r 10m	0.999193
$u_{sta.1}$-$u_{sta.2}$	r 25m	0.920526
$u_{sta.1}$-$u_{sta.2}$	r 100m	0.809951

Table 24. Summary v component windfield statistics for Czech. site 10, 25, and 100 m stable case WOCSS ($v_{station1}$) and WOCSS ($v_{station2}$) windfield outputs (rms=Root Mean Square Difference, agi = Agreement Index, and r=Correlation Coefficient).

Component Sources	Statistic	250m grid
$v_{sta.1}$-$v_{sta.2}$	rms 10m	0.010131
$v_{sta.1}$-$v_{sta.2}$	rms 25m	0.222958
$v_{sta.1}$-$v_{sta.2}$	rms 100m	0.078130
$v_{sta.1}$-$v_{sta.2}$	agi 10m	0.999590
$v_{sta.1}$-$v_{sta.2}$	agi 25m	0.973557
$v_{sta.1}$-$v_{sta.2}$	agi 100m	0.835209
$v_{sta.1}$-$v_{sta.2}$	r 10m	0.999179
$v_{sta.1}$-$v_{sta.2}$	r 25m	0.948924
$v_{sta.1}$-$v_{sta.2}$	r 100m	0.707207

Table 25. Summary u component windfield statistics for Czech. site 10, 25, and 100 m unstable case WOCSS ($u_{station1}$) and WOCSS ($u_{station2}$) windfield outputs (rms=Root Mean Square Difference, agi = Agreement Index, and r=Correlation Coefficient).

Component Sources	Statistic	250m grid
$u_{sta.1}$-$u_{sta.2}$	rms 10m	0.472591
$u_{sta.1}$-$u_{sta.2}$	rms 25m	0.047367
$u_{sta.1}$-$u_{sta.2}$	rms 100m	0.013240
$u_{sta.1}$-$u_{sta.2}$	agi 10m	0.002275
$u_{sta.1}$-$u_{sta.2}$	agi 25m	0.692139
$u_{sta.1}$-$u_{sta.2}$	agi 100m	0.976293
$u_{sta.1}$-$u_{sta.2}$	r 10m	-0.098538
$u_{sta.1}$-$u_{sta.2}$	r 25m	0.481701
$u_{sta.1}$-$u_{sta.2}$	r 100m	0.953453

Table 26. Summary v component windfield statistics for Czech. site 10, 25, and 100 m unstable case WOCSS ($v_{station1}$) and WOCSS ($v_{station2}$) windfield outputs (rms=Root Mean Square Difference, agi = Agreement Index, and r=Correlation Coefficient).

Component Sources	Statistic	250m grid
$v_{sta.1}$-$v_{sta.2}$	rms 10m	1.611782
$v_{sta.1}$-$v_{sta.2}$	rms 25m	0.102231
$v_{sta.1}$-$v_{sta.2}$	rms 100m	0.082092
$v_{sta.1}$-$v_{sta.2}$	agi 10m	0.005405
$v_{sta.1}$-$v_{sta.2}$	agi 25m	0.829984
$v_{sta.1}$-$v_{sta.2}$	agi 100m	0.938916
$v_{sta.1}$-$v_{sta.2}$	r 10m	-0.020724
$v_{sta.1}$-$v_{sta.2}$	r 25m	0.680182
$v_{sta.1}$-$v_{sta.2}$	r 100m	0.881847

10M WOCSS S STA1 U+V SPEED 250M GRID
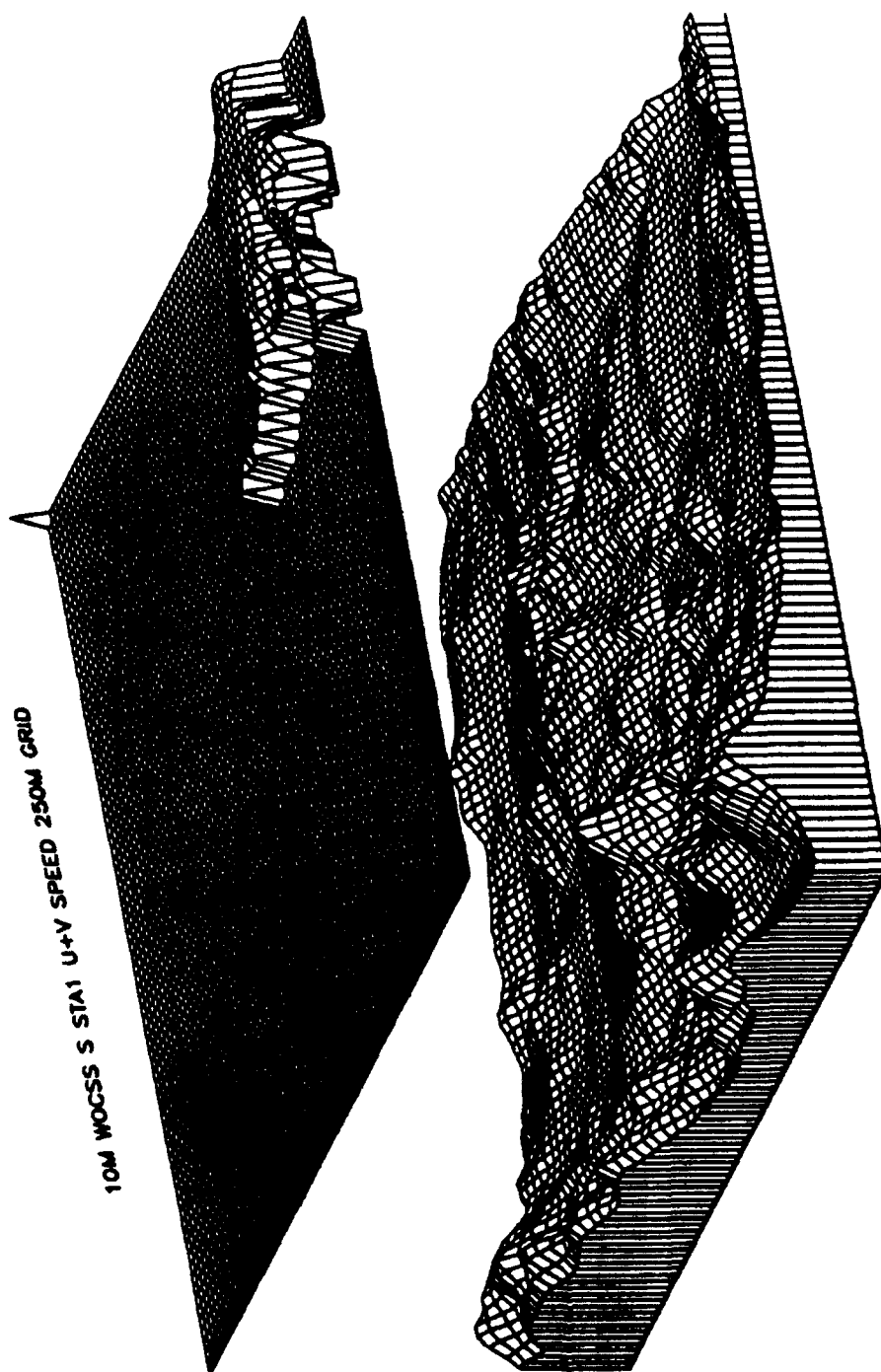
Figure 50. WOCSS Station 1 stable 10 m case wind speed plot for the Czech. site using 250 X 250 square m grid cells (81 X 81). Czech. site terrain elevation is plotted below the speed surface plot (north is located at the top labeled edge of the plotted regions). Minimum, average, and maximum speed values are, respectively, 0.000, 0.845, and 2.202 m/s, where speed increases along the vertical axis.
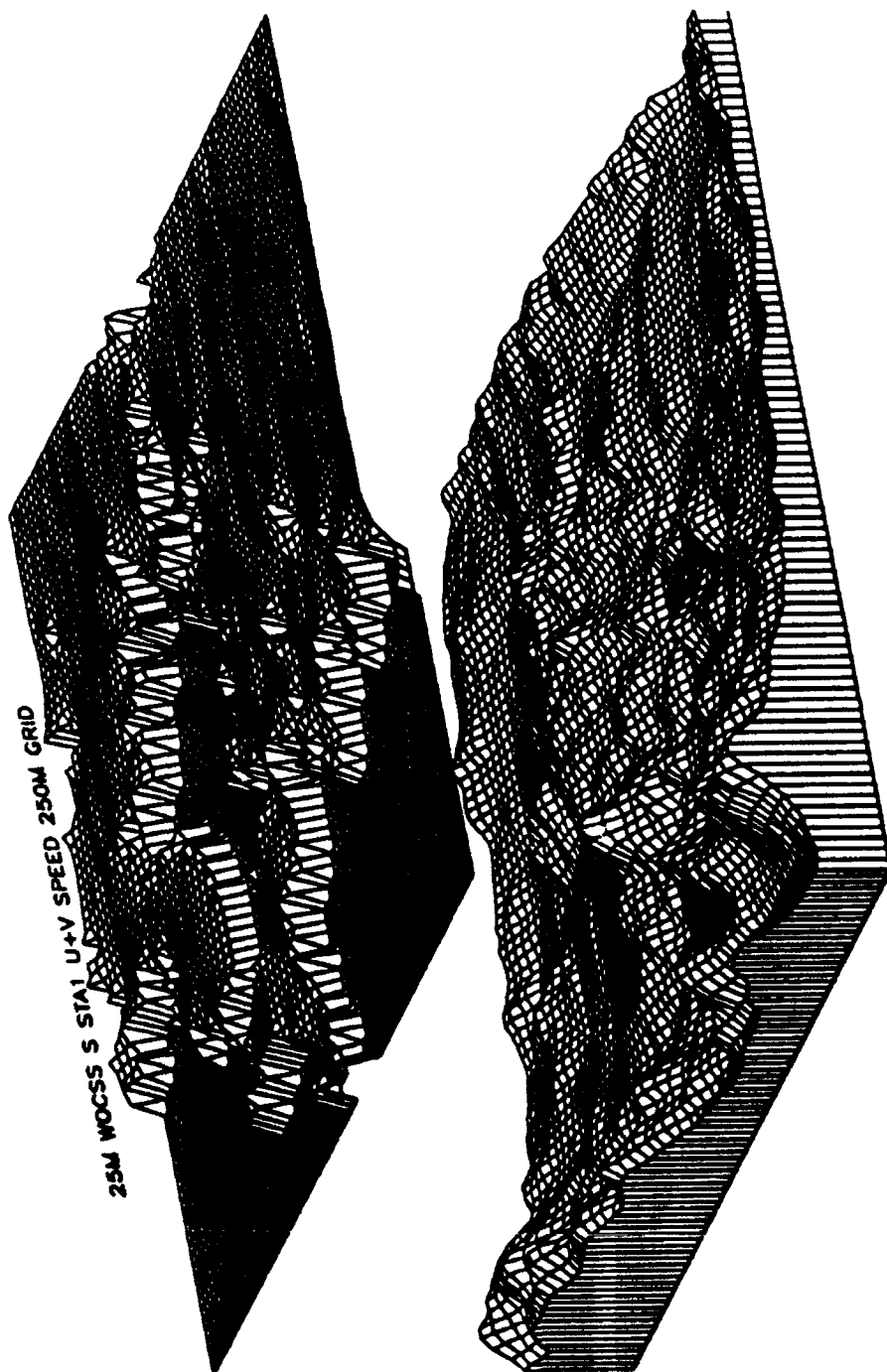
Figure 51. WOCSS Station 1 stable 25 m case wind speed plot for the Czech. site using 250 X 250 square m grid cells (81 X 81). Czech. site terrain elevation is plotted below the speed surface plot (north is located at the top labeled edge of the plotted regions). Minimum, average, and maximum speed values are, respectively, 0.000, 0.812, and 2.202 m/s, where speed increases along the vertical axis.
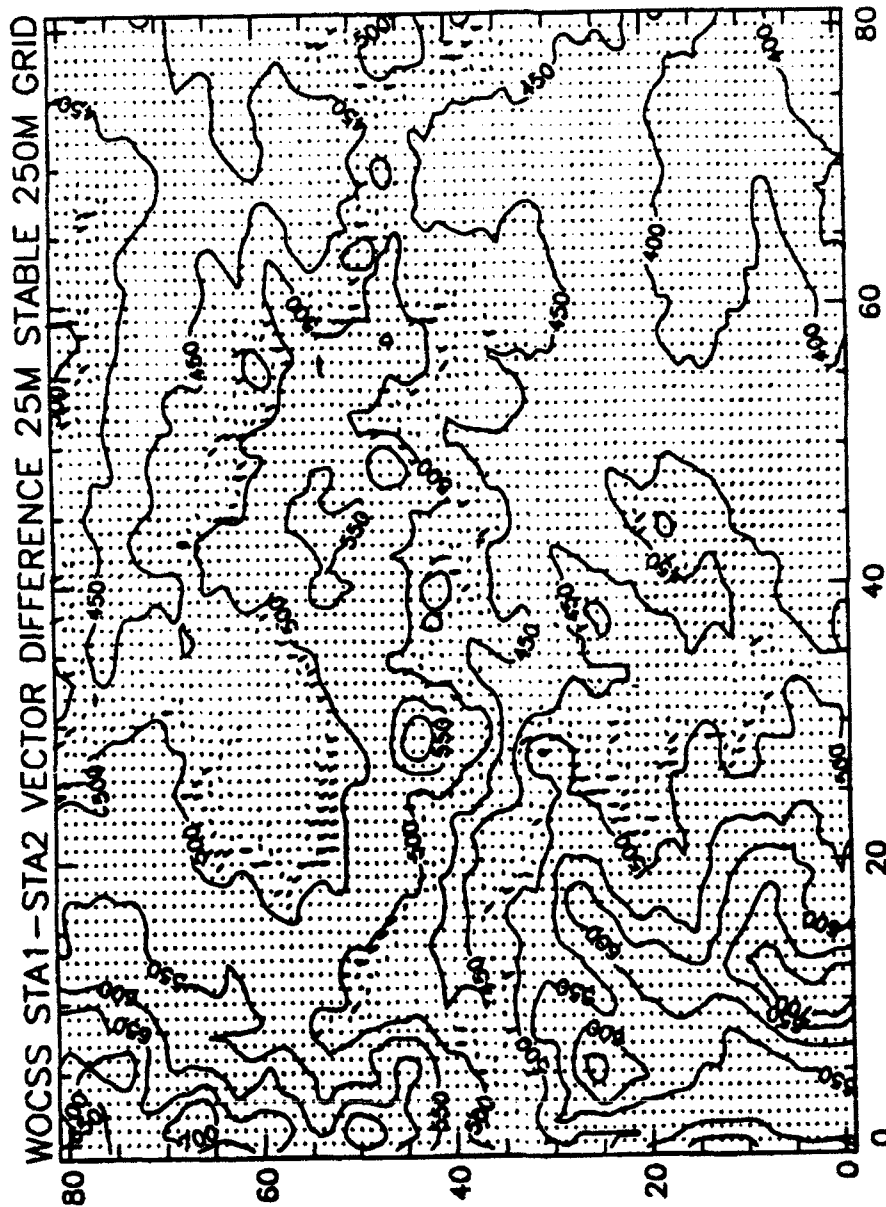
Figure 52. WOCSS Station 1- Station 2 stable 25 m case wind vector difference plot for the Czech. site using 250 X 250 square m grid cells (81 X 81). Czech. site terrain elevation is plotted below the speed surface plot (north is located at the top labeled edge of the plotted regions). Magnitude of average vector differences = 0.066 m/s, and magnitude of maximum vector difference = 1.811 m/s.
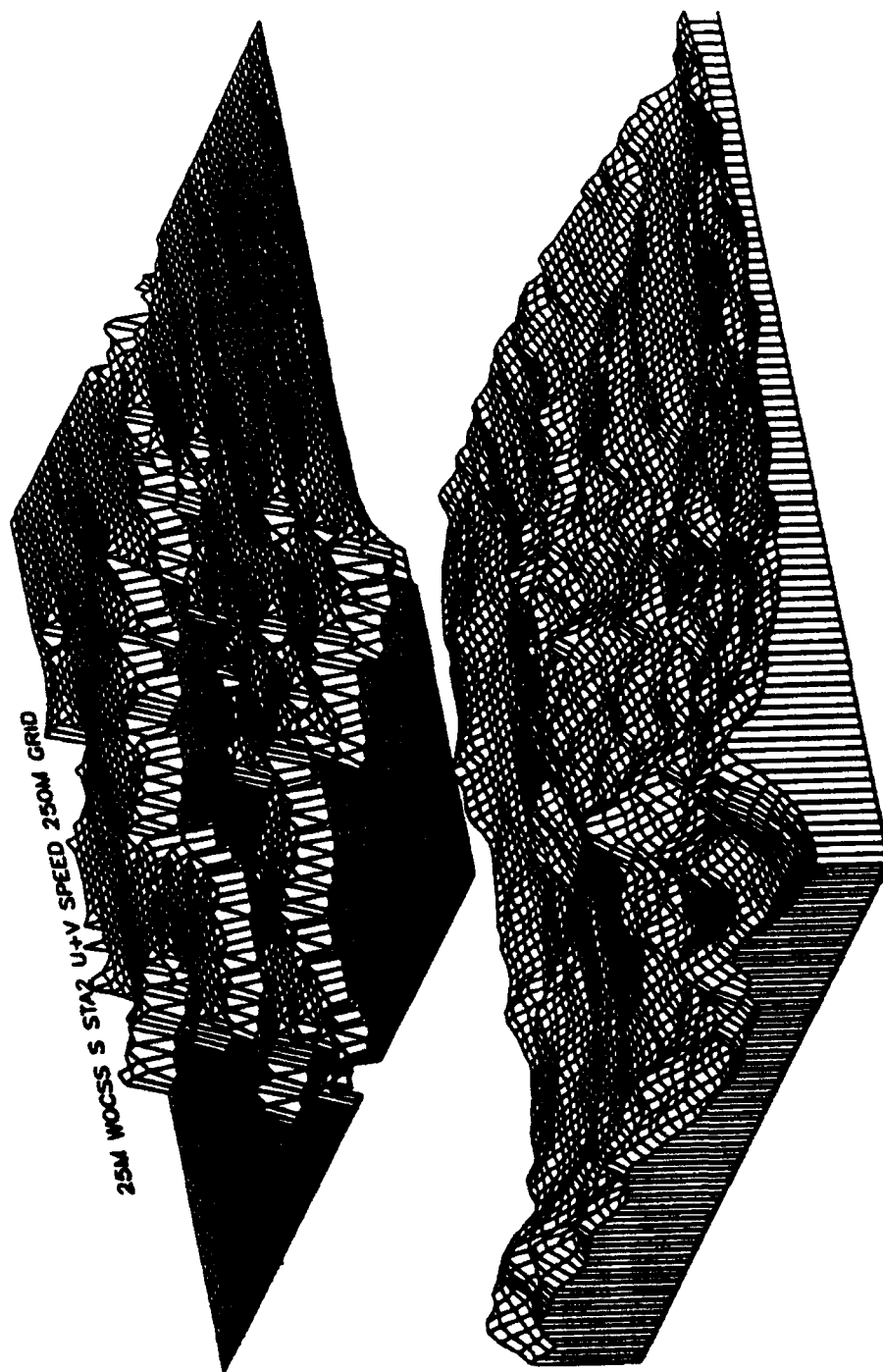
Figure 53. WOCSS Station 2 stable 25 m case wind speed plot for the Czech. site using 250 X 250 square m grid cells (81 X 81). Czech. site terrain elevation is plotted below the speed surface plot (north is located at the top labeled edge of the plotted regions). Minimum, average, and maximum speed values are, respectively, 0.000, 0.812, and 2.196 m/s, where speed increases along the vertical axis.

25M WOCSS U STA2 U+V SPEED 250M GRID
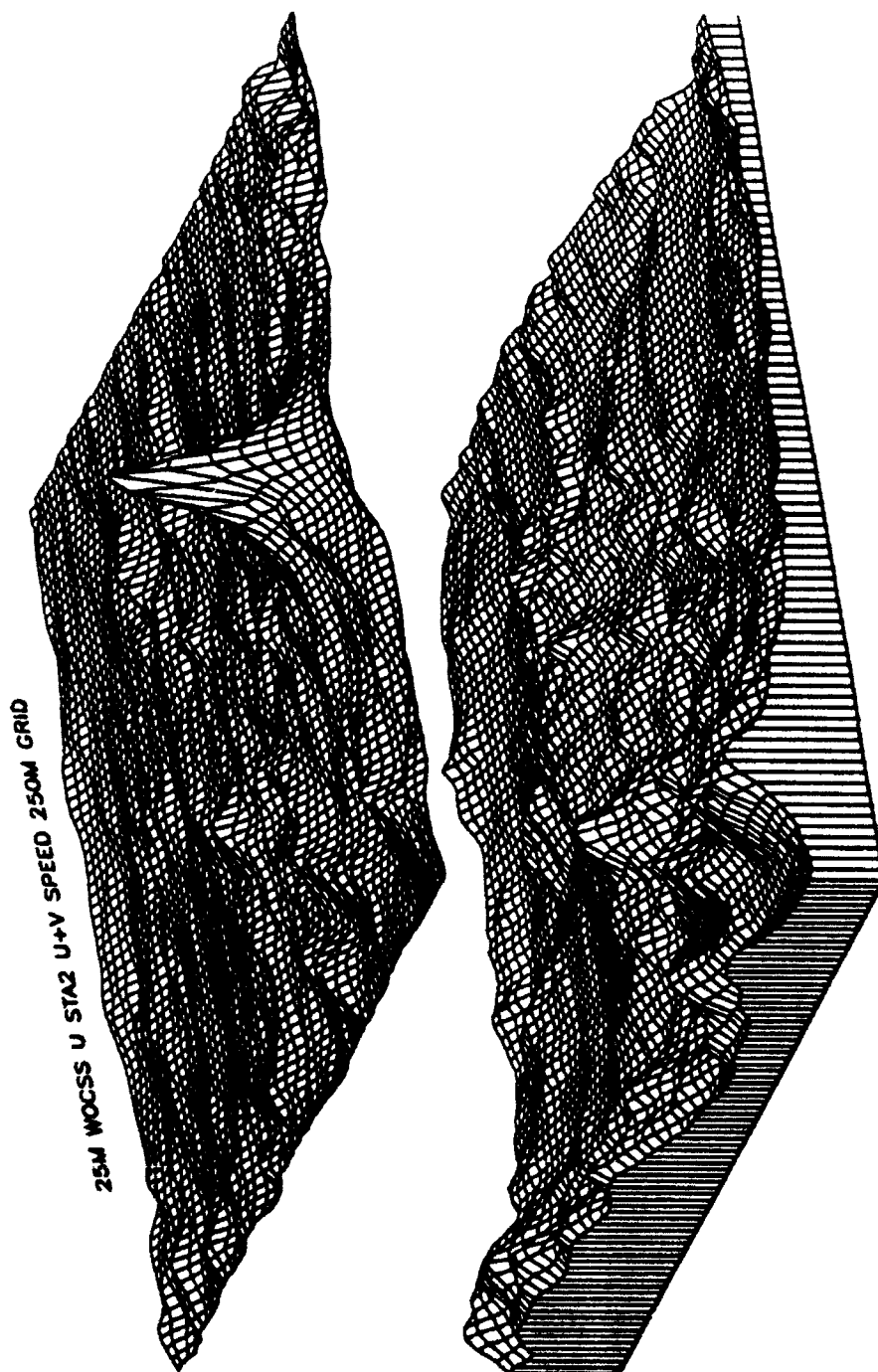
Figure 54. WOCSS Station 2 unstable 25 m case wind speed plot for the Czech. site using 250 X 250 square m grid cells (81 X 81). Czech. site terrain elevation is plotted below the speed surface plot (north is located at the top labeled edge of the plotted regions). Minimum, average, and maximum speed values are, respectively, 4.153, 4.191, and 5.533 m/s, where speed increases along the vertical axis.
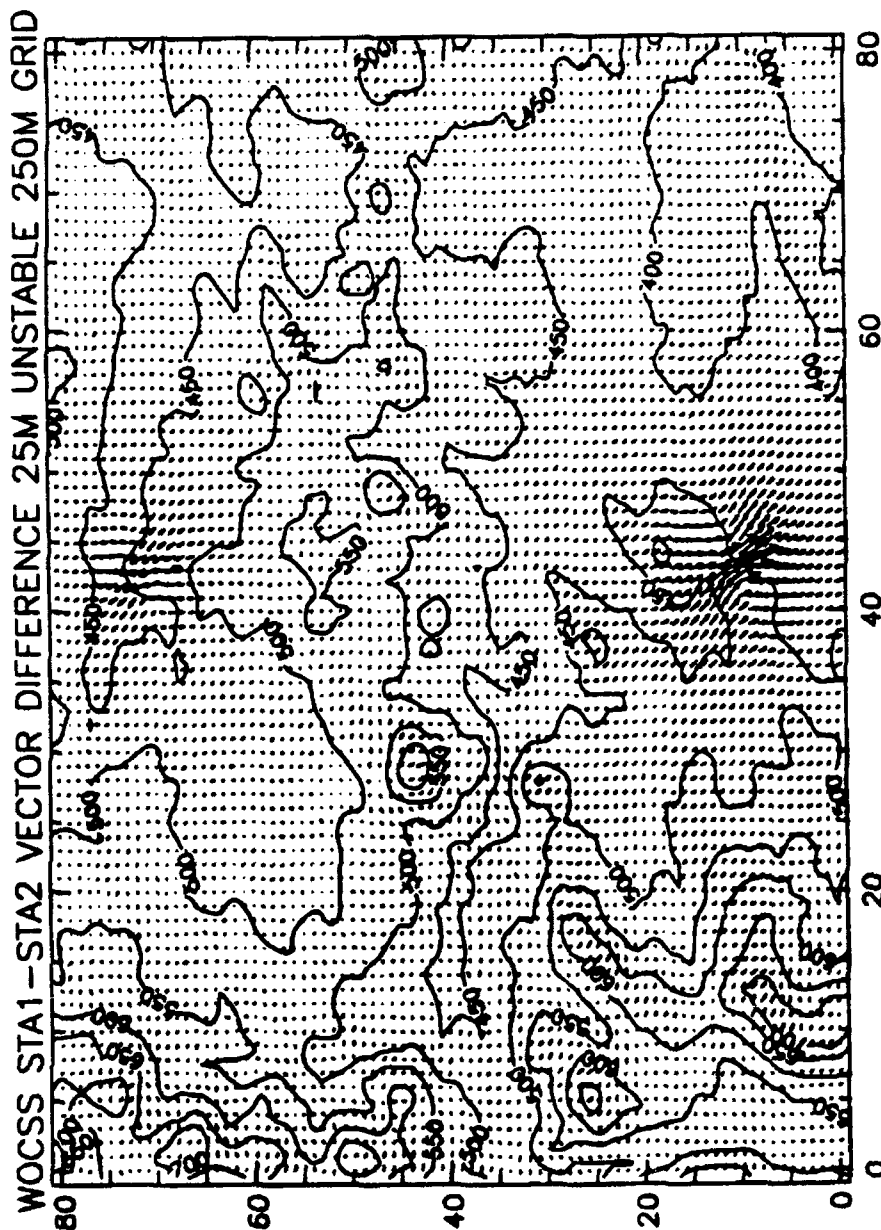
Figure 55. WOCSS Station 1- Station 2 unstable 25 m case wind vector difference plot for the Czech. site using 250 X 250 square m grid cells (81 X 81). Czech. site terrain elevation is plotted below the speed surface plot (north is located at the top labeled edge of the plotted regions). Magnitude of average vector differences = 0.063 m/s, and magnitude of maximum vector difference = 1.292 m/s.

25M WOCSS UNSTBL STA2-1 U+V SPEED DELTAS 250M GRID
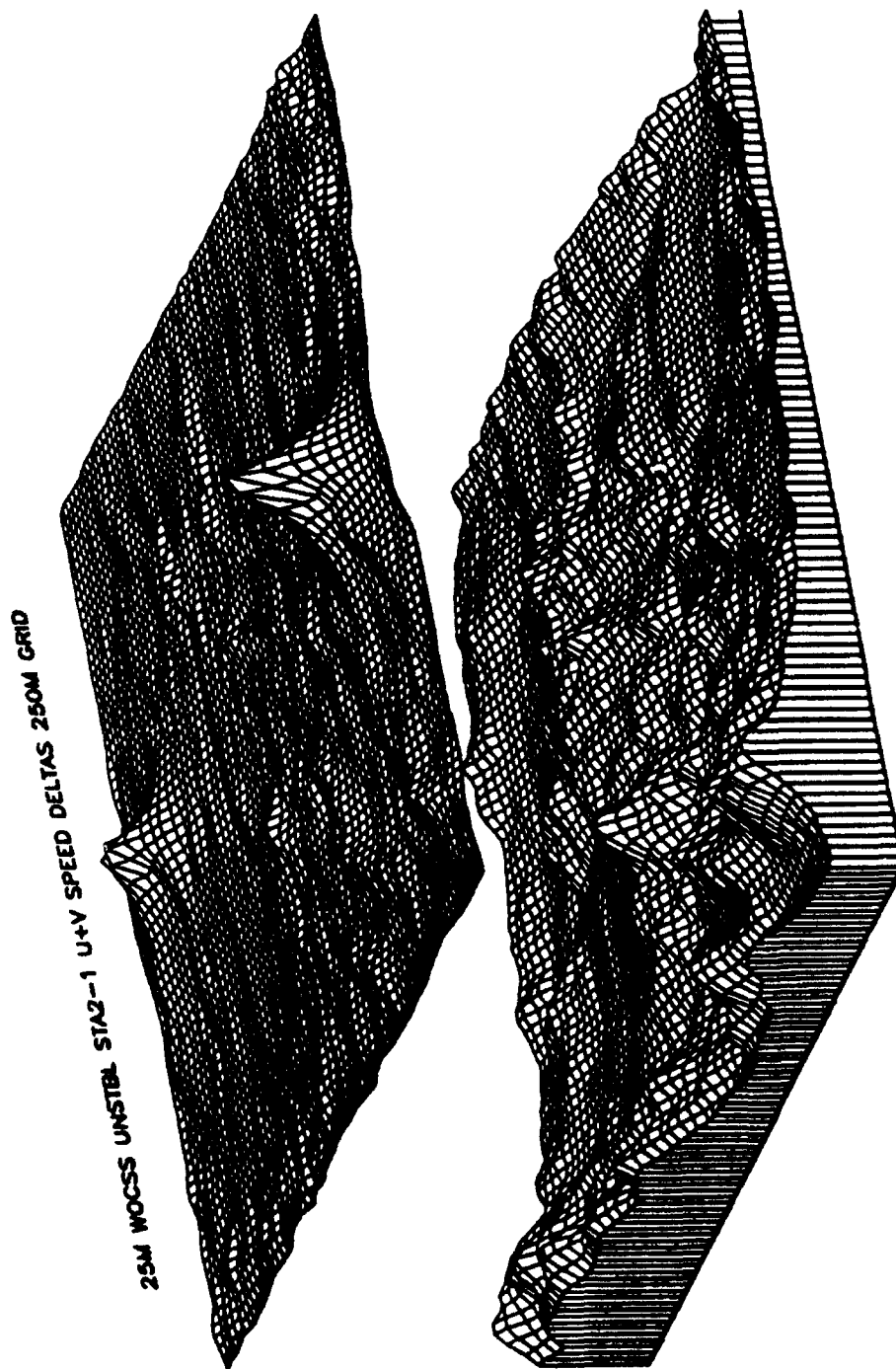
Figure 56. WOCSS Station 1- Station 2 unstable 25 m case wind sped difference plot for the Czech. site using 250 X 250 square m grid cells (81 X 81). Czech. site terrain elevation is plotted below the speed surface plot (north is located at the top labeled edge of the plotted regions). Magnitude of average speed differences = 0.063 m/s, and magnitude of maximum speed difference = 1.292 m/s, with speed increasing upward along the vertical plot axis..
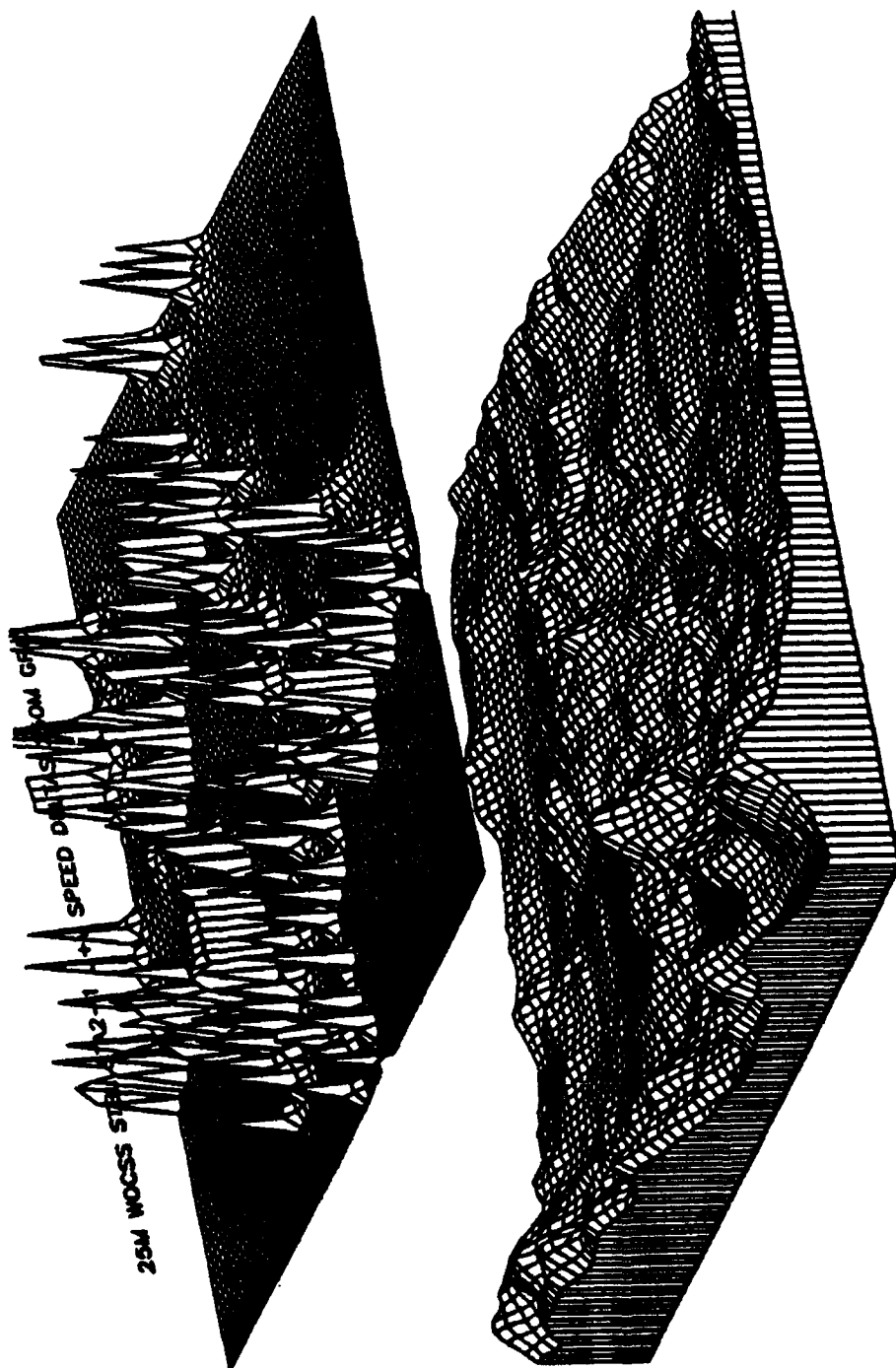
Figure 57. WOCSS Station 1 - Station 2 stable 25 m case wind sped difference plot for the Czech. site using 250 X 250 square m grid cells (81 X 81). Czech. site terrain elevation is plotted below the speed surface plot (north is located at the top labeled edge of the plotted regions). Magnitude of average speed differences = 0.066 m/s, and magnitude of maximum speed difference = 1.811 m/s, with speed increasing upward along the vertical plot axis..
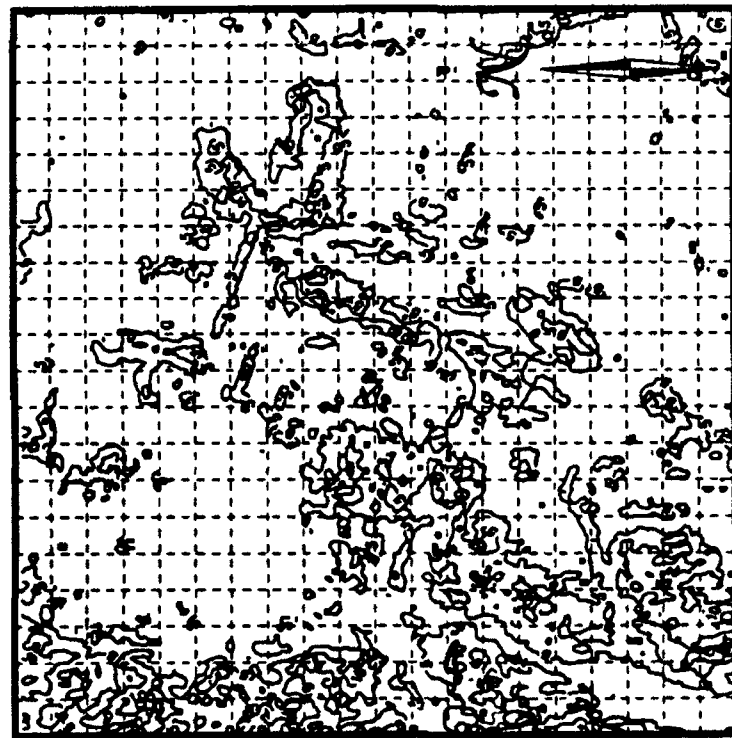
(a)
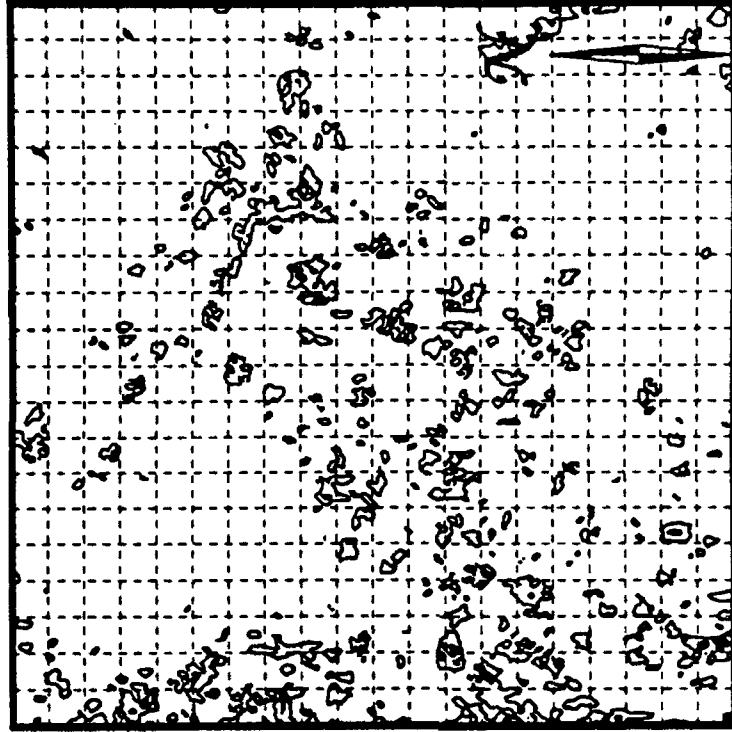
(b)

Figure 58. Czechoslovakia site slope map (a) using 100-m grid spacing for the same area illustrated in Fig. 7(b), where slope contours are plotted at 5, 10, 15, and 20 degrees. Minimum, mean, and maximum slope values (in degrees) are, respectively, 0.00, 3.87, and 23.67. The breaks in slope map (b), also for the 20 km X 20 km Czech. site, has contours plotted for 5, 10, 12.5, and 15 degree changes in slope. Minimum, mean, and maximum changes in slope (also in degrees) are, respectively, 0.00, 2.36, and 17.00. Both slope (a) and breaks in slope (b) agree well with original DTED data in Fig. 7(b). For example, the frequency of slope and breaks in slope contours are significantly coupled to the higher elevation features apparent in Fig. 14.

Table 27. Local maximum slope, θ, and changes in slope, $d\theta$, in degrees, for the Czechoslovakian 20 km × 20 km² terrain site using 100 m grid spacing.

	θ	$d\theta$
MINIMUM	0.00°	0.00°
MEAN	3.87°	2.36°
MAXIMUM	23.67°	17.0°

Table 28. Correlation (in percent) of θ and the occurrence of 25 m AGL stable case wind speed differences greater than or equal to 1.0 m/s for the Czechoslovakian 20 km × 20 km² terrain site.

θ (in degrees)	wind speed differences $\geq$ 1.0 m/s
$0° \leq \theta < 6°$	49 %
$6° \leq \theta < 12°$	51 %
$12° \leq \theta < 24°$	0 %

Table 29. Correlation (in percent) of $d\theta$ and the occurrence of 25 m AGL stable case wind speed differences greater than or equal to 1.0 m/s for the Czechoslovakian 20 km × 20 km² terrain site.

$d\theta$ (in degrees)	wind speed differences $\geq$ 1.0 m/s
$0° \leq d\theta < 4°$	43 %
$4° \leq d\theta < 8°$	57 %
$8° \leq d\theta < 17°$	0 %

(b)

(a)
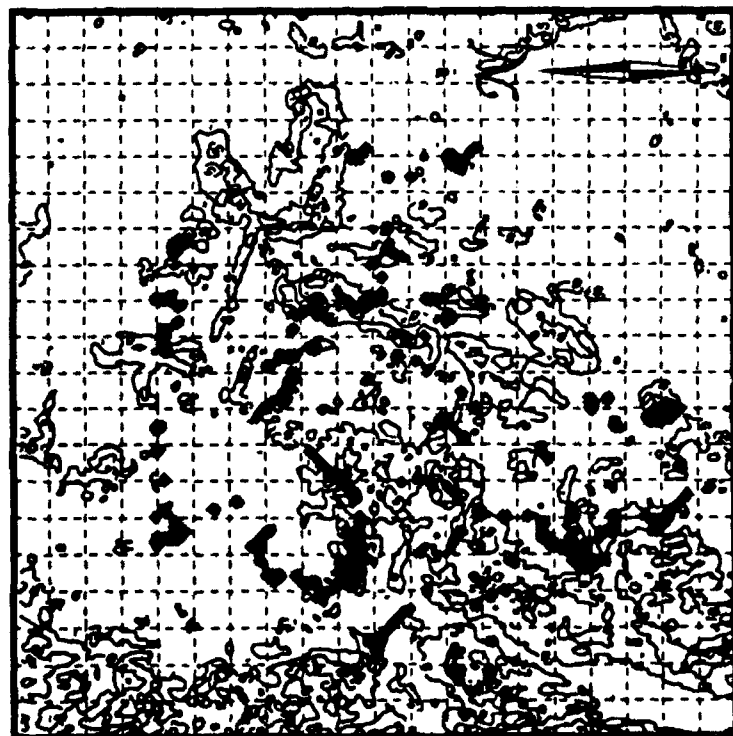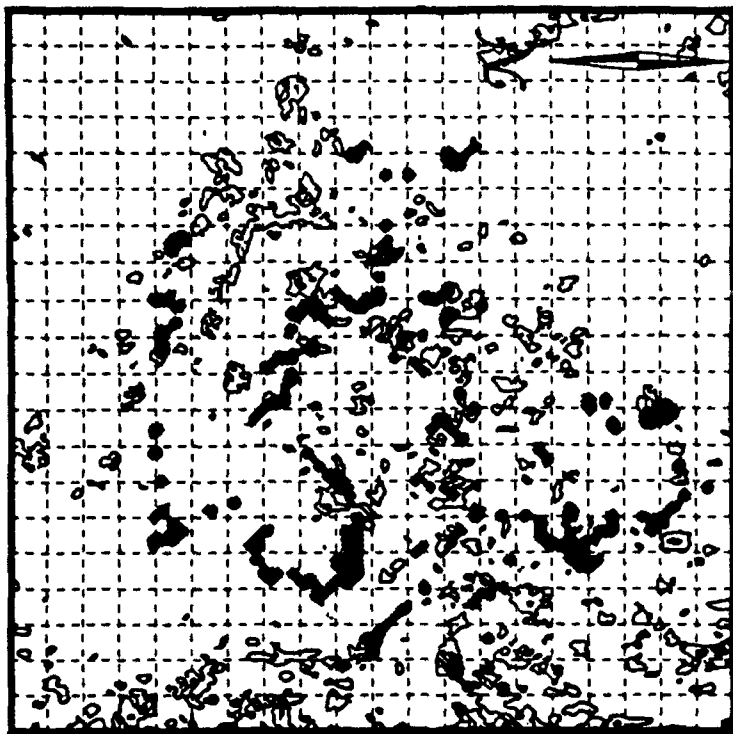
Figure 59. Same as Fig. 58, except that 25 m AGL stable case S1-S2 wind speed differences greater than or equal to 0.25 m/s are included (shaded regions). Widely distributed, significant wind difference regions appear strongly associated with the more complex slope areas from visual inspection of both (a) and (b) above.

4 CONCLUSIONS

Under the light wind speeds used to initialize all stable and unstable case runs (see Appendix A), WSMR, NTC, and Project Wind WOCSS 10 and 25 m AGL results generally contributed significant supplementary physical insight into flow dynamics that were missed by the OBWIND model. The exaggerated extent of WOCSS flow restricted space at 10 m AGL for Project Wind stable conditions (Fig. 46), and for NTC 25 m AGL stable conditions (Fig. 42), suggest that the WOCSS model is oversensitive to terrain complexity greater than that at the WSMR site (e.g., Figs. 25 and 34 demonstrate a more reasonable, moderated application of flow restricted space prediction).

However, the validity of WOCSS model responsiveness to variations in intermediate to very complex terrain appears to improve as wind speeds are increased more toward neutral conditions (see Table 6 and Table A9). Under the light wind speeds considered in this study the WOCSS model appears to predict reasonably valid flow restricted space predictions for use in terrain complexity $\leq$ to the WSMR site terrain (see Table 5 and Fig. 10).

Conversely, the WOCSS model has some serious limitations that are never compensated for. For example, localized horizontal wind direction and speed changes (resulting from mechanical forcing that occurs in nature where flow surfaces intersect with terrain obstacles) are not calculated (e.g., see Fig. 24). This limitation severely restricts the utility of unmodified WOCSS windfields in high resolution atmospheric transport application work.

But results from Table 6 and Figs. 19-21 indicate that the WOCSS model demonstrates significant and reasonable responsiveness to typical stable and unstable variations in boundary layer conditions, as they are observed to behave in nature; this WOCSS windfield responsiveness in predicting reasonable stratified variation in flow restricted spaces could be incorporated as a supplemental

initialization improvement for use in another model. For example, initialization data modified to incorporate the effects of flow restricted spaces, predicted by the WOCSS model, could then be used to initialize a basic mass consistency model, such as OBWIND, thereby improving the overall validity of composite model outputs.

Results from this study, therefore, suggest that the WOCSS model could be selectively employed to produce improved and reasonable estimations of terrain-windfield coupling effects for applications that have not previously considered 1) the dynamics in forcing flow over mechanical obstacles; and 2) the influence of boundary layer kinetic energy and stability effects on flow fields. The results listed in Appendix C (Tables C4 and C5) also suggest that WOCSS solutions should not present significant run-time burdens to users of the WOCSS model. The monotonic performance of WOCSS interpolation operations, also evident in the results of this study, are an algorithm design problem that could be restructured and improved in the future; therefore, this performance characteristic is not a permanent detraction from the WOCSS model's potential validity.

The research work presented here, therefore, demonstrates that the WOCSS model can be employed to simulate complex terrain flow dynamic effects better than basic mass balancing/interpolation schemes, such as the OBWIND model. Measures of the WOCSS model's performance presented in this report suggest that, although it does not simulate dynamic atmospheric flow structure in complex terrain with exceptional fidelity, the WOCSS model has the potential to provide improved dynamic flow structure approximations for a variety of application purposes that currently incorporate only kinematic solutions or that use only a single selected mean wind speed and direction over a complex terrain surface; in this context, the WOCSS model could provide solutions of atmospheric flow structures that have a significantly improved degree of validity.

Potential application of this WOCSS model utility could be incorporated, for example, at the National Training Center (NTC) in California where the U.S. Army carries out low level helicopter training exercises year-round. Terrain is very rugged at the NTC (see Figs. 5 and 10), and flight forecast support is limited there, partially because the NTC occupies a relatively data sparse area, and the availability of experienced forecasters permanently stationed at the NTC is severely limited thus making it an ideal location for reliable, complex terrain wind model applications. WOCSS model guidance could be used, by local NTC forecasters to supplement their present low level flight hazard analysis schemes, thereby improving accuracy of hazard area predictions, which would improve upon the safety of flight operations at the NTC.

Other priority applications that could benefit from incorporating more valid wind field initialization include the U.S. Army's Combined Obscuration Model for Battlefield-Induced Contaminants (COMBIC), developed by Hoock et al. (1987). The effectiveness of applications such as COMBIC are very dependent on the reliability of input environmental factors, such as wind direction and speed. Selective use of the WOCSS model to produce inputs for complex terrain COMBIC applications has the potential to significantly improve current COMBIC methodology, which could ultimately benefit other models that employ COMBIC inputs.

Although difficult to quantify, improved decision making and resource effectiveness could be realized from incorporating the WOCSS model into application environments, such as the ones referred to above. These improvements will result from more well founded decisions made by users of decision aid applications that require valid atmospheric flow structure information, even under data sparse circumstances.

Technical results from this study suggest that 250 m × 250 m grid spacing is a practical limit in reporting on the high resolution performance of modeling and simulation results in 20 km × 20 km spaces. The 250-m grid spacing is also

probably acceptable for high resolution field application use in rural settings, dependent on detailed analysis of terrain complexity (Fig. 10). Even the 1000-m grid spacing could be used if execution run-time, and available storage device had to be reduced, but there would be significant degradations in resolving local flow feature detail (e.g., compare Figs. 31 and 32). However, grid spacing $\leq$ 100 m is recommended for urban scale applications that address the influence of mechanical forcing induced by significant urban structures (e.g., skyscraper and industrial/commercial complexes).

Other results of this study suggest that flow layer output that is used as input to other applications must be carefully selected because of the WOCSS model's stratified responsivenese to initial conditions (see Figs. 19-21 and Table 6). For example, the selection of the flow surface elevation must be significantly related to mean obscurant transport levels in COMBIC applications, which are largely buoyancy considerations.

Results from this study also suggest that no single statistical measure used here (e.g., root mean square difference, agreement index, or correlation coefficients) can be relied upon to infer a complete characterization of model validity, especially without the assistance of supplemental graphic, spatial analyses. For example, in this study, OBWIND-WOCSS correlation coefficients generally tended to increase as grid spacing resolution and predicted flow restricted space decreased (e.g., as distance from the terrain surface increased in the vertical). However, agreement index values produced smaller and less consistent changes when grid space resolution decreased; agreement index changes were generally more responsive to predictions of flow restricted space in the vertical stratification comparisons, but this trend was also inconsistent in most of the study results.

REFERENCES

Arya, S.P., 1988: Introduction to Micrometeorology, Academic Press, New York, 307 pp.

Asculai, E., Doron, E., and Terliuc, B., 1984: "Mesoscale flow over complex terrain, a field study in the Lake Kinneret area," Boundary-Layer Meteorol. 30(1/4), 313-331.

Bannon, P.R., and Zehnder, J.A., 1989: "Baroclinic flow over a mountain ridge," J. Atmos. Sci. 46(5), 703-714.

Beljaars, A.C.M., Walmsley, J.L., and Taylor, P.A., 1987: "Mixed spectral finite- difference model for neutrally stratified boundary layer flow over roughness changes and topography," Boundary-Layer Meteorol. 38(3), 273-303.

Bhumralkar, C.M., Mancuso, R.L., Ludwig, F.L., and Renne, D.S., 1980: "A Practical and Economic Method for Estimating Wind Characteristics at Potential Wind Energy Conversion Sites," Solar Energy 25, 55-65.

Bhumralkar, C.M., Ludwig, F.L., and Mancuso, R.L., 1978: "Estimation of Wind Characteristics at Po tential Wind Energy Conversicn Sites," SRI Project 6537, SRI International, 333 Ravenswood Avenue, Menlo Park, CA 94025, 72 p.

Brown, R.A., 1991: Fluid Mechanics of the Atmosphere, Academic Press, Inc., NewYork, 489 pp.

Cionco, R.M. 1989: "Design and Execution of Project Wind," 19th Conference on Agricultural and Forest Meteorology and the 9th Conference on Biometeorology and Aerobiology, March 7-10, 1989, Charleston, South Carolina.

Davis, C.G., Bunker, S.S., and Mutschlecner, J.P, 1984: "Atmospheric transport models for complex terrain," J. Climate and Appl. Meteorol. 23(2), 235-238.

Deardorff, J.W., Ueyoshi, K., and Han, Y.-J., 1984: "Numerical study of terrain-induced mesoscale motions and hydrostatic form drag in a heated, growing mixed layer," J. Atmos. Sci. 41(8), 1420-1441.

Dickerson, M.H., 1978: "MASCON-A mass consistency atmospheric flux model for regions with com plex terrain," J. Appl. Meteorol. 17, 241-253.

Dinar, N., 1984: "Mass consistent models for wind distribution in complex terrain, fast algorithms for three-dimensional problems," Boundary-Layer Meteorol. 30(1/4), 177-199.

Endlich, R.M., 1967: "An Iterative Method for Altering the Kinematic Properties of Wind Fields," J. Appl. Meteorol. 6, 837-844.

Endlich, R.M., Ludwig, F., Bhumralkar, C., and Estoque, M., 1982: "A Diagnostic Model for Estimating Wind a Potential Sites for Wind Turbines," J. Appl. Meteorol. 21, 1441-1454.

Endlich, R.M., 1984: "Wind energy estimates by use of diagnostic model," Boundary-Layer Meteorol. 30(1/4), 375-386.

Erasmus, D.A., 1986: "A Model for objective simulation of boundary layer winds in an area of complex terrain," J. Climate and Appl. Meteorol. 25(12), 1832-1841.

Fast, J.D., and Takle, E.S., 1988: "Application of a quasi-nonhydrostatic parameterization for numerically modeling neutral flow over an isolated hill," Boundary-Layer Meteorol. 44(3), 285-304.

Goodin, W., McRae, G., and Seinfeld, J., 1980: "An Objective Analysis Technique for Constructing Three-dimensional Urban-scale Wind Fields," J. Appl. Meteorol. 19, 98-108.

Han, Y.-J., Ueyoshi, K., and Deardorff, J.W., 1982: "Numerical Study of Terrain-Induced Mesoscale Motions in a Mixed Layer," J. Atmos. Sci. 39, 2464-2476.

Hansen, S.H., and Flanigan, R.T., 1989: "User's Manual to Process Defense Mapping Agency Elevation Data," Internal Technical Report, U.S. Army Atmospheric Sciences Laboratory, White Sands Missile Range, New Mexico 88002-5501.

Henmi, T., and Tabor, P.A., 1988: "Principles and evaluation of a three-dimensional windflow model over the National Training Center (Fort Irwin, CA) area," ASL-IR-0233, U.S. Army Atmospher ic Sciences Laboratory, White Sands Missile Range, New Mexico 88002-5501.

Henmi and Tabor, 1990: "Assimilation of Wind Field Over Complex Terrain," Fifth Conference on Mountain Meteorology, 118-124.

Hess, S.L., 1979: Introduction to Theoretical Meteorology Robert E. Krieger Publishing Co., New York, 362 pp.

Hodges, J.S., and Dewar, J.A., 1990: "A 97% Solution to Model Validation," Military Operations Re search Society Mini-Symposium on Simulation Validation, Albuquerque, New Mexico, 17 pp.

Holtslag, A., and van Ulden, A., 1983: "A simple scheme for daytime estimates of surface fluxes from routine weather data," J. Climate and Appl. Meteorol. 22, 517-529.

Holton, J.R., 1979: An Introduction to Dynamic Meteorology, Academic Press, New York, 391 pp.

Hoock, D.W., Sutherland, R.A., and Clayton, D., 1987: "Combined Obscuration Model For Battlefield-Induced Contaminants (COMBIC)," TR-0221-11, U.S. Army Atmospheric Sciences Laboratory, White Sands Missile Range, New Mexico 88002-5501.

Hooke, W.H., 1986: "Gravity Waves," Chapter 12, Mesoscal Meteorology and Forecasting, American Meteorological Society, Boston, MA, 272-288.

Huschke, R., 1989: Glossary of Meteorology, American Meteorological Society, Boston, Mass., 638 pp.

Kao, S.K., 1981: "An Analytical Solution for Three-Dimensional Stationary Flows in the Atmosphere Boundary Layer Over Terrain," J. Appl. Meteorol. 20, 386-390.

King, D.S. and Bunker, S.S., 1984: "Application of atmospheric transport models for complex terrain," J. Climate and Appl. Meteorol. 23(2), 239-246.

Lee, H.N., and Kau, W.S., 1984: "Simulation of three-dimensional wind flow over complex terrain in the atmospheric boundary layer," Boundary-Layer Meteorol. 29(4), 381-396.

Lee, M., and Hansen, S., 1989: "Portable Low-Level Aviation Turbulence Decision Aids Evaluated at White Sands Missile Range," 10th Annual Electro-Optical Systems Atmospheric Effects Library/Tactical Weather Intelligence (EOSAEL/TWI) Conference Proceedings, Las Cruces, New Mexico, U.S.A., 47-56.

Liu, C.Y. and Goodin, W.R., 1976: "An Iterative Algorithm for Objective Wind Field Analysis," Mon. Wea. Review 104, 784-792.

Ludwig, F.L., Endlich, R.M., and Nitz, K.C., 1986: "Inclusion of Energy Considerations in a Mass-Consistent Wind Interpolation Scheme," Proc. 6th EOSAEL/TWI Conference 2, 387-399.

Ludwig, F.L. and Endlich, R.M., 1988: "User's Guide for the Winds on Critical Streamline Surfaces (WOCSS) Code," ASL-CR-88-0001/0680-1, U.S. Army Atmospheric Science Laboratory, White Sands Missile Range, New Mexico 88002-5501.

Ludwig, F.L., Endlich, R.M., and Lester, P., 1990: "A Computer Code for Objective Analysis of Tur bulence and Winds in the Lower Atmosphere," ASL-CR-90-0001/0680-1, U.S. Army Atmo spheric Sciences Laboratory, White Sands Missile Range, New Mexico 88002-5501.

Mahrer, Y. and Pielka, R.A., 1975: "A Numerical Study of the Air Flow Over Mountains Using the Two-Dimensional Version of the University of Virginia Mesoscale Model," J. Atmos. Sci. 32, 2144-2155.

Marwitz, J.D., 1983: "The kinematics of orographic airflow during Sierra storms." J. Atmos. Sci. 40, 1218-1227.

Mass, C.F., and Dempsey, D.P., 1985: "A One-level, Mesoscale Model for Diagnosing Surface Winds in Mountainous and Coastal Regions," Mon. Wea. Review 13, 1211-1227.

Nastrom, G.D., Fritts, D.C., and Gage, K.S., 1987: "Investigation of terrain effects on the mesoscale spectrum of atmospheric motions," J. Atmos. Sci. 44(2), 3087-3096.

Orlanski, I., 1975: "A Rational Subdivision of Scales for Atmospheric Processes," Bull. Am. Meteorol. Soc. 56, 527- 530.

Pielke, R.A., 1984: Mesoscale Meteorological Modeling, Academic Press, Inc., New York, 612 pp.

Queney, P., 1948: "The Problem of Air Flow Over Mountains: A Summary of Theoretical Studies," Bull. Amer. Meteorol. Soc. 29, 16-26.

Riegel, C.A., 1974: Lecture Notes on Atmospheric Dynamics and Thermodynamics, San Jose State University, CA, 550 pp.

Sears, F.W., Zemansky, M.W., and Young, H.D., 1982: University Physics, 6th Edition, Addison-Wesley Publishing Co., Menlo Park, California, 929 pp.

Sherman, C.A., 1978: "A Mass-Consistent Model for Wind Field over Complex Terrain," J. Appl. Meteorol. 17, 312-319.

Smedman, A-S., and Bergstrom, H., 1984: "Flow characteristic above a very low and gently sloping hill," Boundary-Layer Meteorol. 29(1), 21-37.

Smith, R.B., 1988: "Linear theory of stratified flow past an isolated mountain in isosteric coordinates," J. Atmos. Sci. 45(24), 3889-3896.

Steyn, D.G., and McKendry, I.G., 1988: "Quantitative and Qualitative Evaluation of a Three-Dimensional Mesoscale Numerical Model Simulation of a Sea Breeze in Complex Terrain," Mon. Wea. Review 116, 1914-1926.

Sutherland, R., Hansen, F., and Bach, W., 1986: "A quantitative method for estimating pasquill stability class from windspeed and sensible heat flux density," Boundary-Layer Meteorol. 37, 357-369.

Tucker, D.F., and Henmi, T., 1990: "Usefulness of a diagnostic wind model for real-time analysis of the wind field," ASL-TR-0274, U.S. Army Atmospheric Sciences Laboratory, White Sands Missile Range, New Mexico 88002-5501.

Willmott, C.J., Ackleson, S.G., Davis, R.E., Feddema, J.J., Klink, K.M., Legates, D.R., O'Donnel, J., and Rowe, C.M., 1985: "Statistics for the Evaluation and Comparison of Models," J. of Geo physical Research 90, 8995-9005.

van Ulden, A., and Holtslag, A., 1985: "Estimation of Atmospheric Boundary Layer Parameters for Diffusion Applications," J. Climate and Appl. Meteorol. 24, 1196-1207.

APPENDIX A

Meteorological Initialization Data

Surface meteorological observation towers that provided observation data in this research work had anemometer wind sensors elevated at approximately ten meters above ground level. Sensor locations at the WSMR, NTC, and Project WIND sites are indicated in Figs. A1-3, and Tables A1-3. Radiosonde upper-air observation data was also available at the WSMR and Project WIND sites. Figure A4 and Table A4 note the initialization points for the Czechoslovakian site, for which no actual meteorological data was available. Tables A5-8 list the actual surface initialization data used in the case studies.

Case study initialization data were broken down into stable and unstable conditions. Several stability criteria were used to analyze all observation data sets. For example, Pasquill's Stability Categories [1] were relied upon to initially classify the stability rating of each surface observation set, primarily using wind speed and time of day (insolation inferencing). Table A9 lists the Pasquill Stability Category scheme that was used to carry out an initial classification. Local diurnal trends in pressure, and temperature were taken into consideration to further rate each observation set's stability ratings.

Temperature lapse rate in the vertical was also considered where radiosonde data was available (see Figs A5-A8). Potential temperature, θ, is plotted as a function of height above ground level in Figs. A5-A8 and was solved for using the following equation (from Hess, 1979):

$$\theta = T(\frac{p}{1000})^{-\kappa} \qquad (A-1)$$

where T is the temperature of a parcel of air that has been moved adiabatically

---
[1]Arya, 1988.

119

to a new pressure, p. The κ term[2] is equivalent to R/c_p, where R represents the *specific gas constant*, and c_p is the *specific heat capacity at constant pressure*.

The potential temperature lapse rate, $\frac{d\theta}{dz}$, in Figs. A5-A8 illustrate the vertical stability classification according to the criteria in Table A10. Actual vertical temperature profile data was used for the WSMR and Project WIND model runs. These data were then modified to develop representative initialization data for the NTC and Czechoslovakian sites. It should be noted that the increase in non-linear behavior of the WSMR vertical temperature profile, in Fig. A5, over that of the Project WIND data (Fig. A7) resulted from a higher frequency of observation data being collected during the WSMR radiosonde ascents.

The actual WSMR and Project WIND $\frac{d\theta}{dz}$ are noted in Table A11. These data were used to develop vertical lapse rate initialization data for the NTC and Czechoslovakian model runs. For example, the observed lapse rates for WSMR and Project WIND were averaged and then reduced by a factor of 50%. The 50% reduction was implemented to reduce the generated lapse rates to more neutral conditions, a major assumption in the application of a logarithmic velocity profile equation, which is discussed after the temperature profile construction methodology has been reviewed.

Several steps were used to construct theoretical vertical temperature profiles for the NTC and Czechoslovakian sites. First, the pressure at sea level was estimated for each site under both the stable and unstable thermal conditions (noted in Tabes A6 and A8, respectively). This required extrapolating site temperatures to sea level using the standard atmospheric lapse rate of 6.5°C/km (Huschke, 1989).

---

[2]κ has a value of 0.286 for dry air (Hess, 1979).

Then an equation of state was used to calculate a representative sea level pressure (Hess, 1979):

$$p = \rho R T \qquad (A-2)$$

where p is pressure, ρ is density (set at 0.0012250 gm/cm^3, from Huschke, 1979), R is a specific gas constant (2870.4 mb cm^3/gm K for dry air, from Riegel, 1974), and T is the temperture (in Kelvin).

The hypsometric formula was then used to solve for the pressure of each observation site under each stability condition (from Riegel, 1974):

$$z_2 - z_1 = -\frac{R_d}{g} \int_{p_1}^{p_2} T^* \frac{dp}{p} \qquad (A-3)$$

where $z_2 - z_1$ is the difference in vertical elevation between the points of interest, R_d is the specific gas constant for dry air, g is acceleration due to gravity, p_1 and p_2 are the pressures at points z_1 and z_2, respectively, and T^* is the virtual temperature.

T^* can be found using the following equation, also from Riegal (1974):

$$T^* = T \left(1 + 0.608 \frac{\epsilon \cdot e}{p - (1 - \epsilon)e} \right) \qquad (A-4)$$

where T is the observed temperature, ϵ is the ratio of the mass of water vapor to the mass of dry air, e is the partial pressure due to water vapor, and p is the total pressure. In this research work, only dry air cases are considered; therefore, both ϵ and e are zero. As a result, $T^* \approx T$ is a valid assumption, and T can be used in equation A-3. After solving equation A-3 for p_2, then equation A-1 can be used to find θ for each case at each site. From this point, Table A11 can be used to quickly construct vertical temperature profiles (see Figs. A6 and A8).

Since radiosonde data were not available for the NTC and Czechoslovakian sites, hypothetical wind initialization data were developed using a logarithmic velocity profile approximation (Arya, 1988) assuming a neutral boundary layer

$$U = u^* \frac{1}{k} \ln \frac{z}{z_o} \qquad (A-5)$$

121

where U is the mean horizontal wind speed as a function of friction velocity, u^*, von Karman's constant, k, the roughness parameter, z_o, and height above a surface, z. The friction velocity term is defined as $u^* \equiv \sqrt{\frac{\tau_o}{\rho}}$, where τ_o is surface shear stress, and ρ is the fluid density.

Variability of the NTC terrain elevation data was greater than any other site (see Table 5). Therefore, an approximation for z_o at the NTC was made (from Arya, 1988), and this value was scaled to the fractional variability of the Czechoslovakian site's elevation data (see Table A12). The u^* term used for the NTC vertical wind profile was solved for using actual observation data at $z=10$ m, and the selected value for z_o. Then the logarithmic velocity profile equation was employed to develop the vertical wind profile initialization data for the NTC model runs. A similar approach was used to generate initialization profile data for the Czechoslovakian model runs, except that the surface winds were user specified instead of being actual observation data (see Tables A12 and A13).

To develop accurate vertical wind direction profiles the theoretical Ekman spiral was employed through the use of the following equations, also from Hess (1979),

$$u = u_g[1 - e^{(-\sqrt{f/2K} \cdot z)} \cos(\sqrt{f/2K} \cdot z)] \qquad (A-6)$$

$$v = u_g e^{(-\sqrt{f/2K} \cdot z)} \sin(\sqrt{f/2K} \cdot z) \qquad (A-7)$$

where u and v are wind speed components in the x and y directions respectively, f is the Coriolis parameter ($\approx 10^{-4} s^{-1}$), K originated as a eddy-exchange coefficient constant (empirically set at $\approx 5 \times 10^4 cm^2 s^{-1}$), and z represents vertical elevation above ground level. An *Ekman* boundary layer balances coriolis, pressure gradient, and frictional forces with height, up to the lowest atmospheric level free from surface effect influences; winds at and above this level are referred to as geostrophic and are represented above as the u_g and v_g components (Hess,

1979). Plots of the modeled wind profiles used in the NTC and Czecoslovakian simulation runs are illustrated in Figs. A6 and A8, respectively.

In summary, the averaged observation data at the WSMR and Project WIND site had slightly stronger wind velocities ($\approx \overline{2.46m/s}$ at 10 m above ground level) for the unstable cases versus stable cases. The unstable cases also had greater average magnitudes in potential temperature lapse rates ($\approx \overline{0.83°C}$) within the first 100 m above ground level (see Figs. A5 and A7). These properties of the observed stable and unstable conditions were carried over in the construction of missing data for the NTC and Czechoslovakian sites, but in these cases the properties were adjusted toward neutral conditions – to accommodate the use of equations A-5 - A-7 (see Figs A6 and A8).

Part of the meteorological initialization data presented here was acquired from actual field observations. The WSMR and Project WIND sites had complete sets of 10-meter surface observation data that were coupled to radiosonde vertical profile data. The NTC site illustrated a transition toward more data sparse field conditions, where only a limited number of 10 meter surface observations were available. However, using classical methods, correlated vertical data were developed to establish complete sets of reasonable model initialization data.

Then transition toward the worst case scenario, in terms of data sparsity, was established for the Czechoslovakian site; no observation data was available for initializing model runs for this site. However, by tailoring properties of observation data from the other sites, in conjunction with the selective application of classical meteorological theory, reasonable model initialization data was also developed for the Czechoslovakian site. The construction of this hypothetical, user specified, initialization data illustrates methods that could be used to improve the credibility and resolution of environmental conditions in remote site simulation activities.
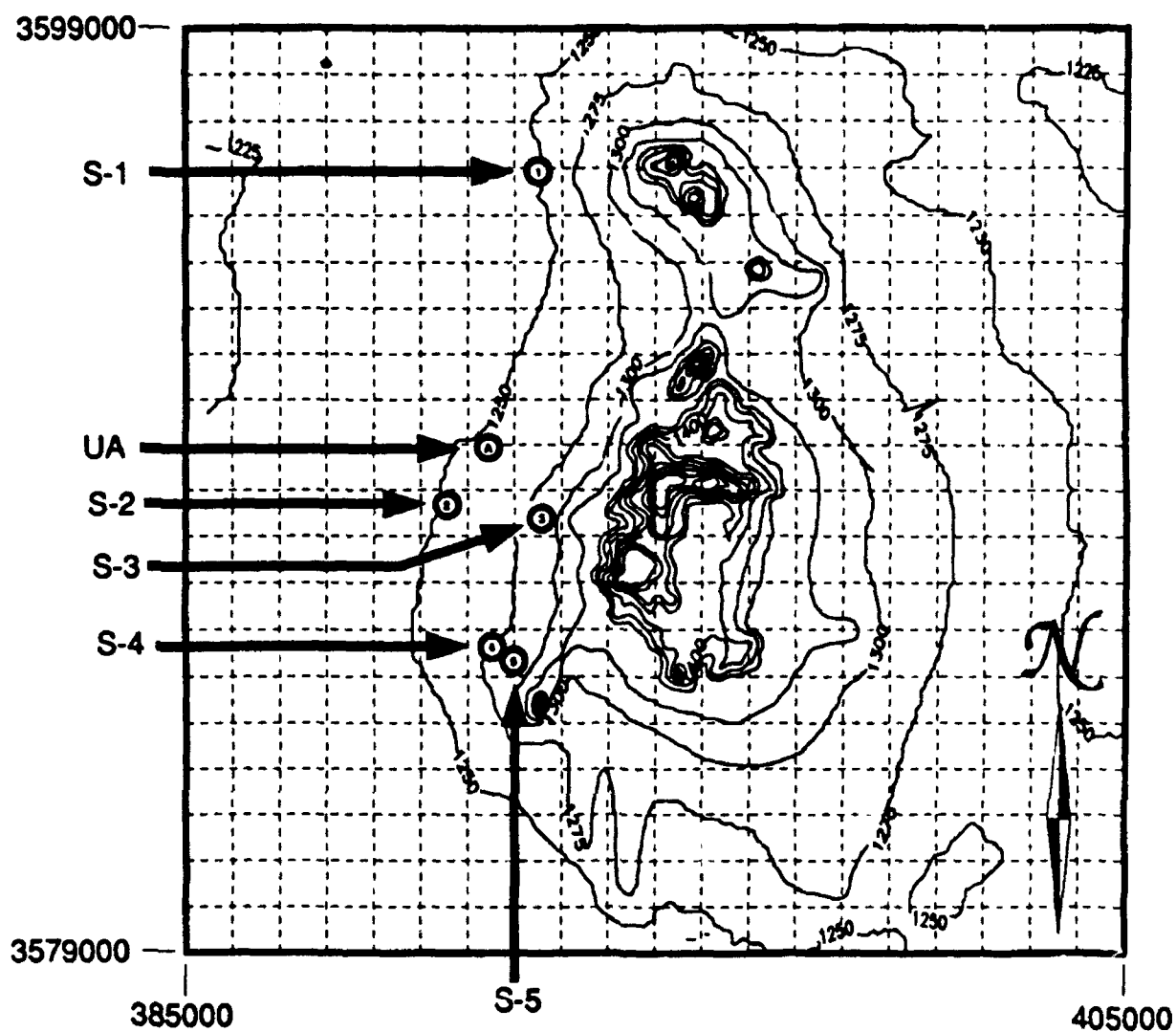
Figure A1. WSMR surface meteorological observation tower locations (S-1 through S-5), and the radiosonde observation launch site (UA). UTM coordinate references are included.

Table A1. WSMR meteorological observation sensor locations.

Observation Site	UTM Easting	UTM Northing	Surface Elevation (m)
S-1	392426.7	3595988.4	1250.0
S-2	390597.0	3588896.5	1254.1
S-3	392637.9	3588464.9	1288.9
S-4	391510.3	3585415.8	1282.3
S-5	391632.1	3585256.1	1322.2
UA	391483.2	3589972.6	1253.0
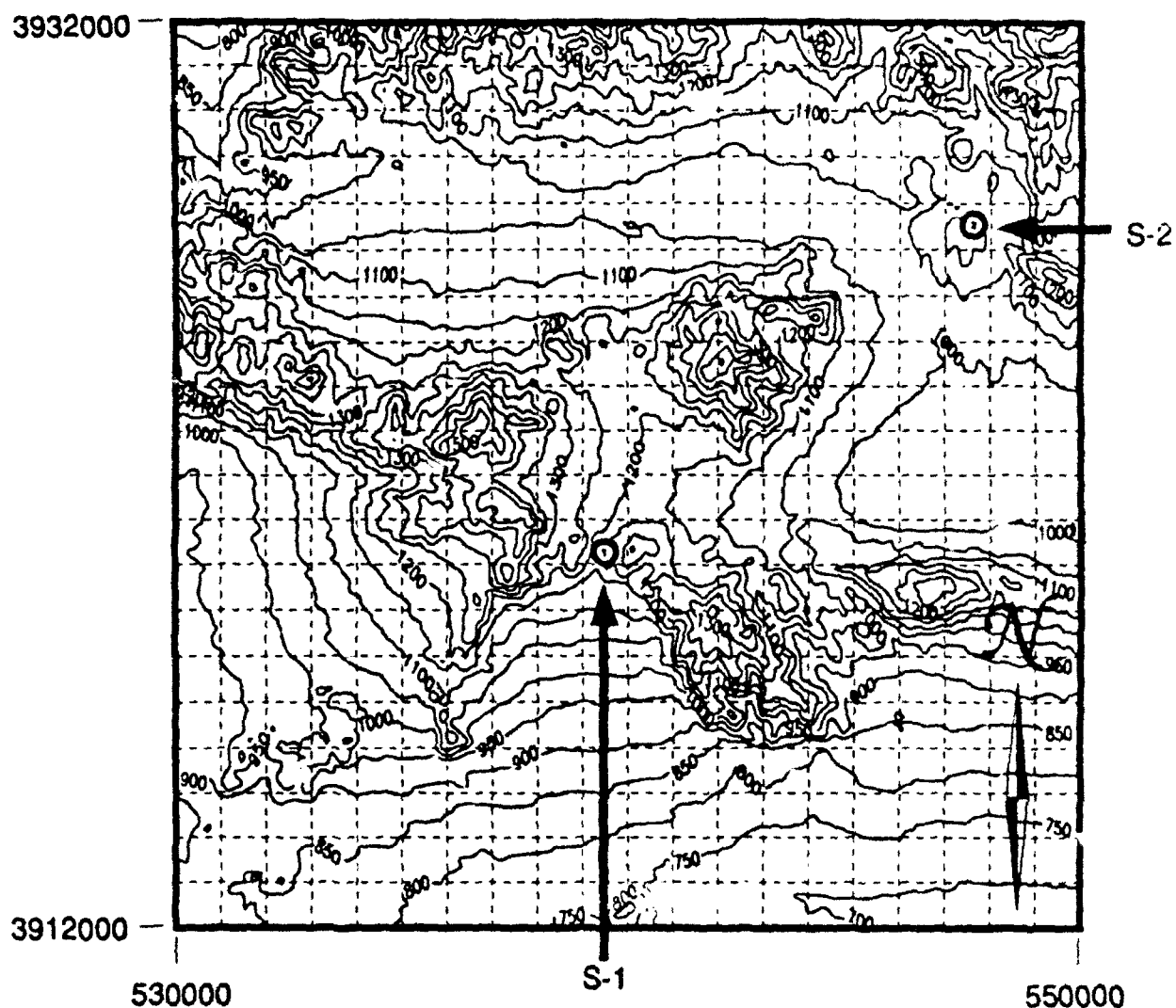
Figure A2. NTC surface meteorological observation tower locations (S-1 and S-2). No radiosonde sites were available in this study area. UTM coordinate references are included.

Table A2. NTC meteorological observation sensor locations.

Observation Site	UTM Easting	UTM Northing	Surface Elevation (m)
S-1	539500.0	3920200.0	1180.0
S-2	547800.0	3927500.0	1080.0
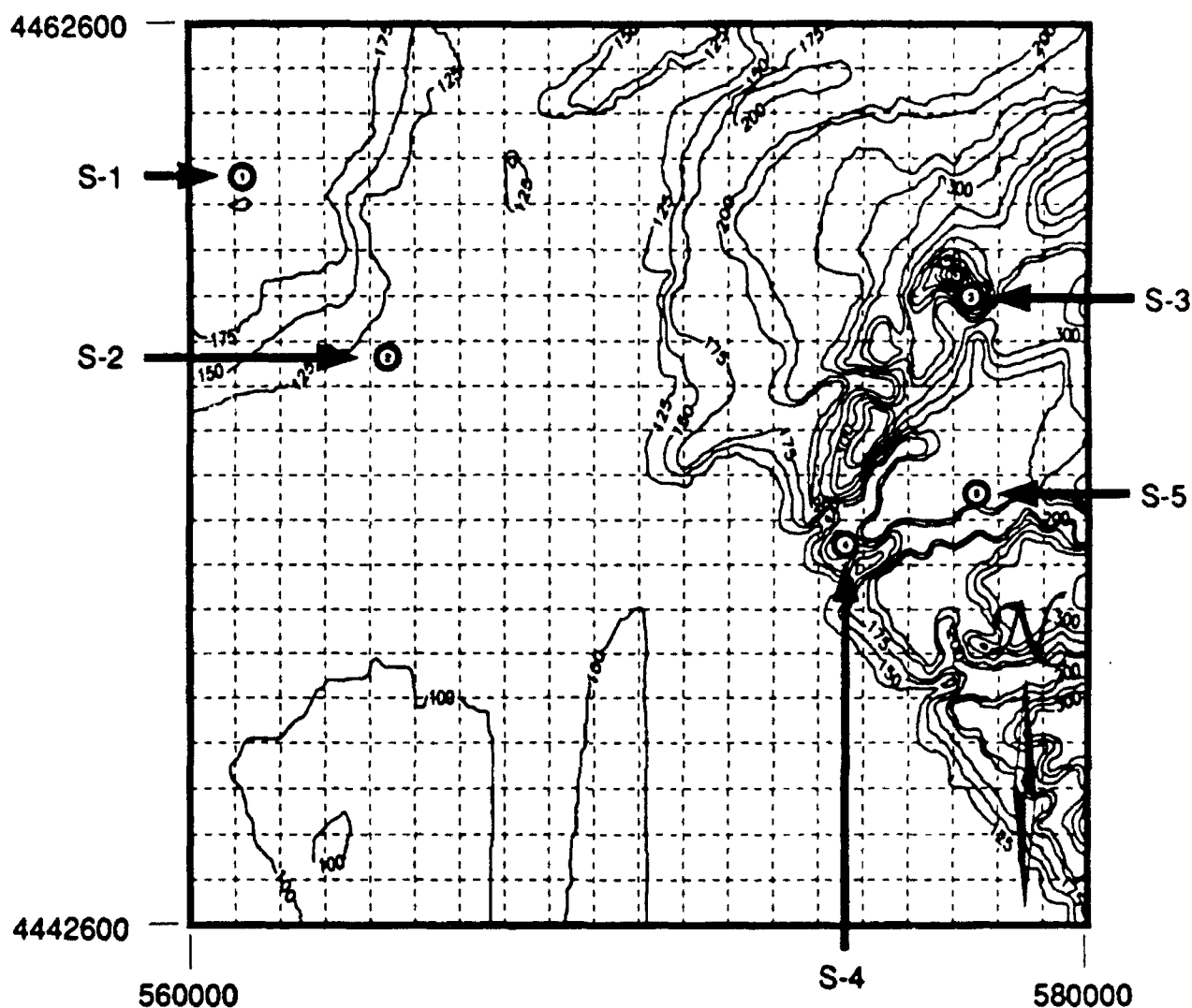
Figure A3. Project WIND surface meteorological observation tower locations
(S-1 through S-5). The radiosonde observation launch site was co-
located at tower S-4's location. UTM coordinate references given.

Table A3. Project WIND meteorological observation sensor locations.

Observation Site	UTM Easting	UTM Northing	Surface Elevation (m)
S-1	561170.0	4459350.0	216.0
S-2	564400.0	4455350.0	137.0
S-3	577760.0	4456650.0	543.0
S-4	574500.0	4451100.0	253.0
S-5	577380.0	4452180.0	271.0
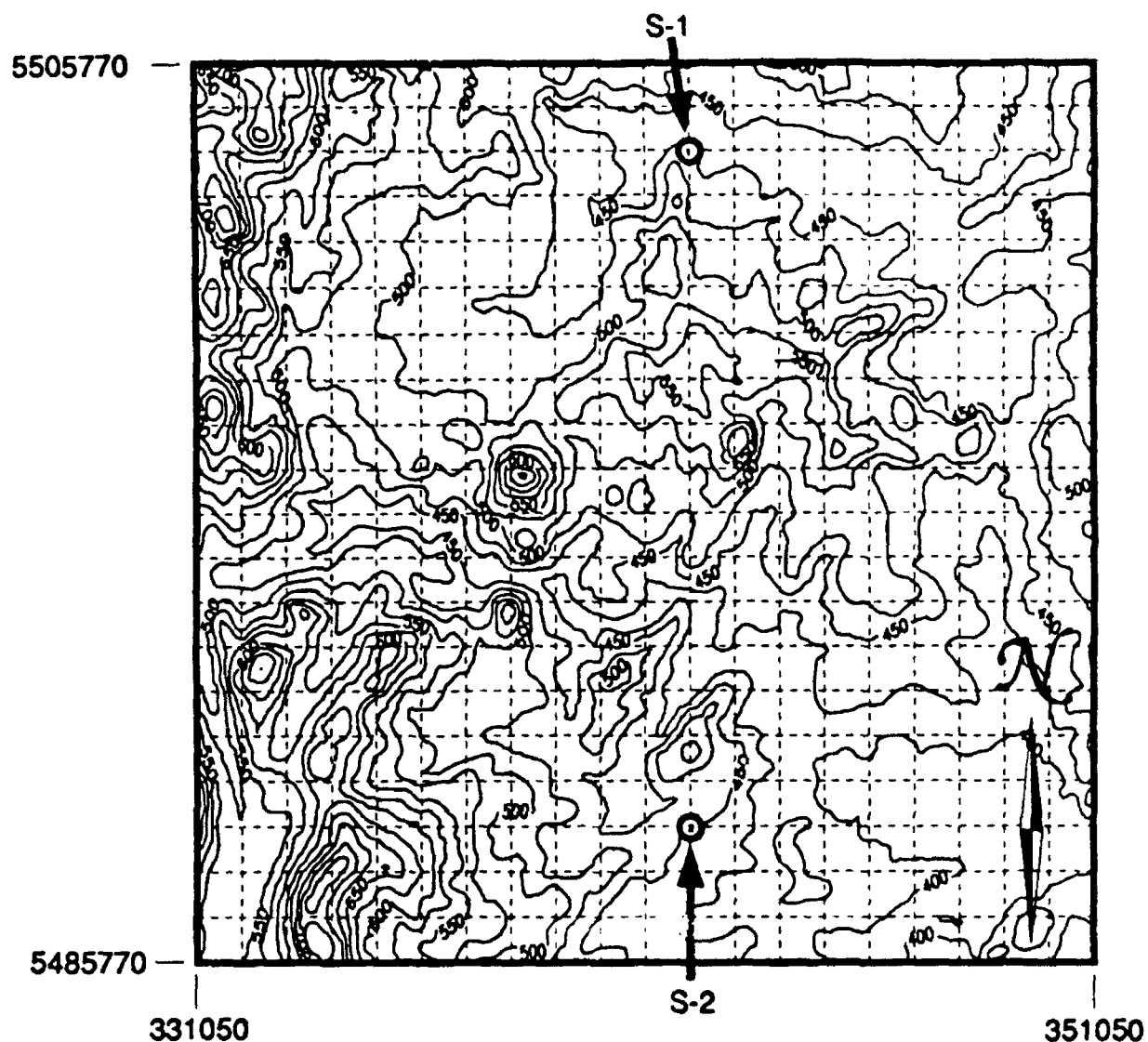
Figure A4. Czechoslovakian surface meteorological initialization points (S-1 and S-2). No actual surface or upper air data was used for this study area; meteorological data was strictly user defined. UTM references given.

Table A4. Czechoslovakian meteorological data initialization points.

Initialization Points	UTM Easting	UTM Northing	Surface Elevation (m)
S-1	342050.0	5503770.0	450.0
S-2	342050.0	5488770.0	450.0

Table A5.1 WSMR surface wind observation data (15 minute averages) under diurnally stable, early morning atmospheric conditions at 03:00 L on 21 July 1991.

Station	Wind Speed (m/s)	Wind Direction (deg)	Temp. (C)
S-1	2.77	049	21.64
S-2	2.08	041	22.01
S-3	1.78	051	22.56
S-4	1.70	056	22.54
S-5	3.45	080	22.53
AVG	2.36	055	22.26

Table A5.2 WSMR surface wind observation data during unstable, late-afternoon conditions at 16:00 L on 27 July 1991.

Station	Wind Speed (m/s)	Wind Direction (deg)	Temp. (C)
S-1	2.86	074	30.17
S-2	3.18	086	30.18
S-3	6.52	074	29.54
S-4	5.45	087	30.79
S-5	6.04	085	29.99
AVG	4.81	081	30.13

Table A6.1 NTC surface wind observation data (15 minute averages) under stable, early morning conditions at 01:00 L on 24 February 1988.

Station	Wind Speed (m/s)	Wind Direction (deg)	Temp. (C)
S-1	1.03	173	12.78
S-2	2.57	120	14.44
AVG	1.80	147	13.61

Table A6.2 NTC surface wind observation data during unstable, mid-afternoon conditions at 15:00 L on 22 February 1988.

Station	Wind Speed (m/s)	Wind Direction (deg)	Temp. (C)
S-1	3.09	355	20.00
S-2	3.09	325	20.00
AVG	3.09	340	20.00

Table A7.1 Project WIND surface wind observation data under diurnally stable, late evening atmospheric conditions at 23:00 L on 25 June 1985.

Station	Wind Speed (m/s)	Wind Direction (deg)	Temp. (C)
S-1	1.96	345	27.40
S-2	2.12	341	28.00
S-3	0.81	300	27.60
S-4	2.64	307	28.20
S-5	1.86	306	28.00
AVG	1.88	320	27.84

Table A7.2 Project WIND surface wind observation data during unstable, mid-afternoon atmospheric conditions at 15:00 L on 25 June 1985.

Station	Wind Speed (m/s)	Wind Direction (deg)	Temp. (C)
S-1	3.16	169	33.80
S-2	2.59	152	34.20
S-3	5.02	174	31.70
S-4	5.30	212	33.50
S-5	5.66	197	33.80
AVG	4.35	181	33.40

Table A8.1 Hypothetical surface wind initialization data for the Czechoslovakian terrain representative of stable conditions.

Station	Wind Speed (m/s)	Wind Direction (deg)	Temp. (C)
S-1	1.02	315	10.00
S-2	1.02	315	10.00

Table A8.2 Hypothetical surface wind initialization data for the Czechoslovakian terrain representative of unstable conditions.

Station	Wind Speed (m/s)	Wind Direction (deg)	Temp. (C)
S-1	3.06	315	20.00
S-2	3.06	315	20.00

Table A9. Pasquill's Stability Categorization scheme [3] used to initially classify surface meteorological data into stable and unstable sets. *Ext*=extreme, *Mod*=moderate, and *Slt*=slight.

Wind Speed (m/s)	Mod-Slg Daytime Insolation	Nighttime
<2	Ext-Mod Unstable	–
2	Ext-Mod Unstable	Slt-Mod Stable
4	Mod-Slt Unstable	Near Neutral
6	Slt Unstable-Near Neutral	Near Neutral
>6	Slt Unstable-Near Neutral	Near Neutral

Table A10. Potential temperature lapse rate, $\frac{d\theta}{dz}$, vertical stability classification scheme [4]

Lapse Rate	Stability Rating
$d\theta/dz < 0$	UNSTABLE
$d\theta/dz = 0$	NEUTRAL
$d\theta/dz > 0$	STABLE

Table A11. Potential temperature lapse rate, $\frac{d\theta}{dz}$, in actual observation data selected for the WSMR and Project WIND model runs. Here dz represents the distance between ground level (sfc) and 100 m above ground level, and $d\theta$ is the difference between $\theta_{100\ m}$ and θ_{sfc}.

Site	Stable $d\theta/dz$	Unstable $d\theta/dz$
WSMR	+1.85°	−2.60°
Project WIND	+2.95°	−3.85°
AVERAGE	+2.40°	−3.23°

---

[3] Arya, 1988.
[4] Hess, 1979.
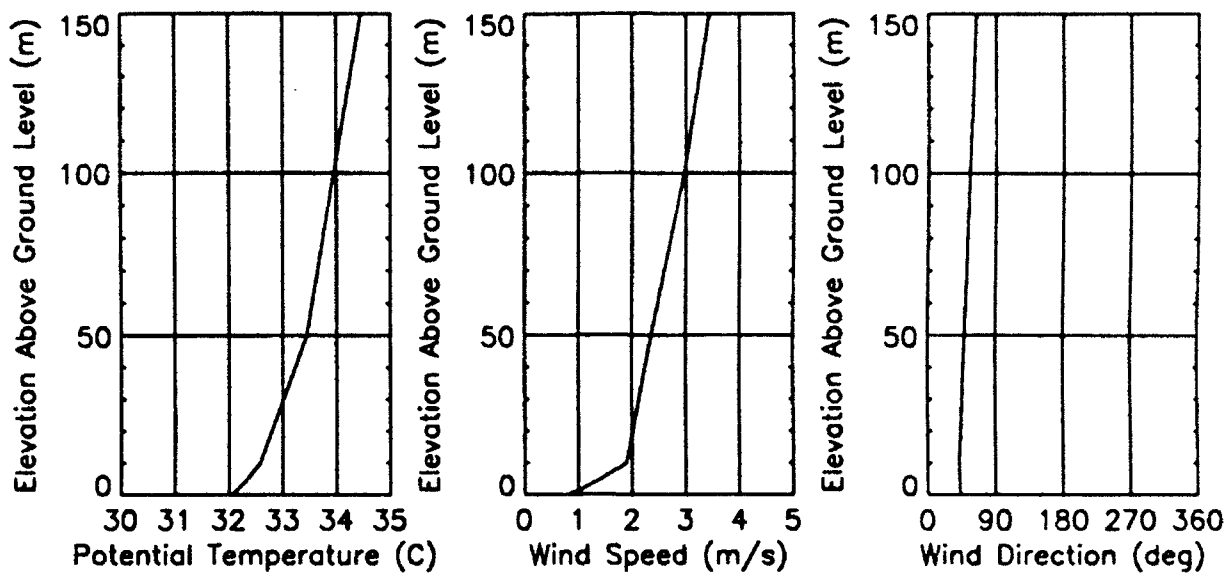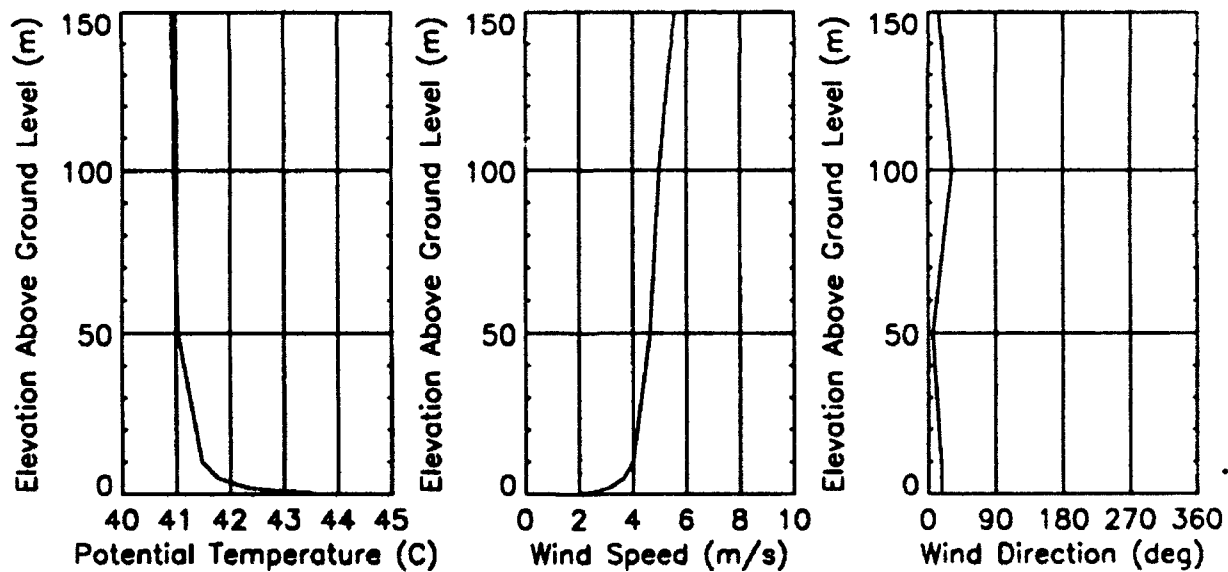
Figure A5. WSMR stable (a) and unstable (b) meteorological upper air initialization data correlated with the surface observation data in Tables A5.1 and A5.2, respectively.
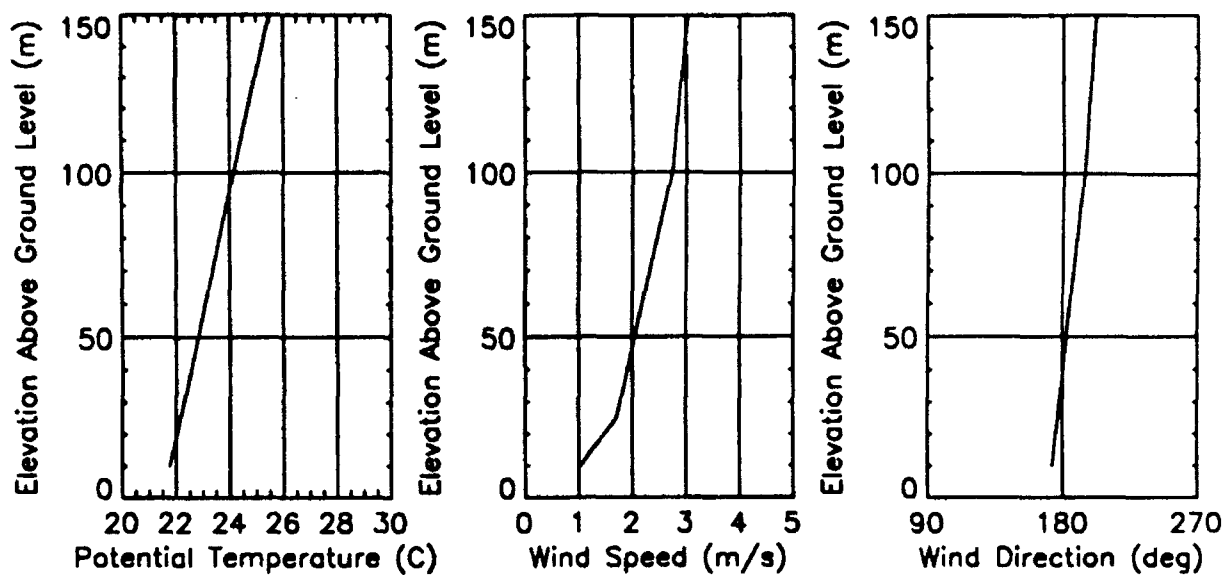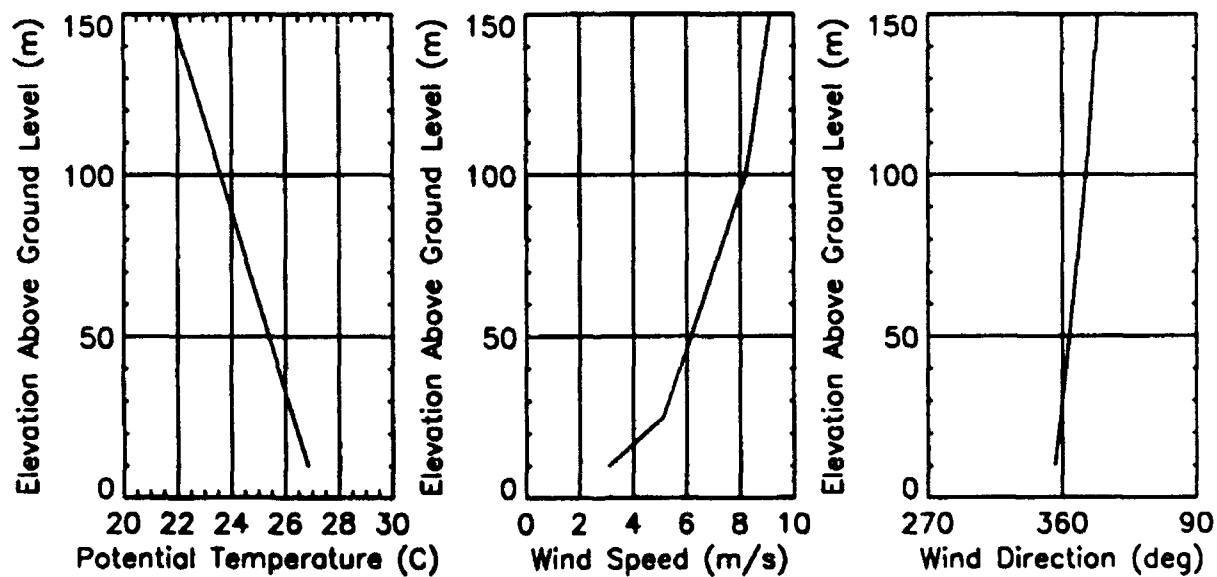
Figure A6. NTC stable (a) and unstable (b) modeled upper air initialization scheme that was correlated with the surface observation data in Tables A6.1 and A6.2, respectively, for observation site S-1 (Fig. A2 and Table A2).

132
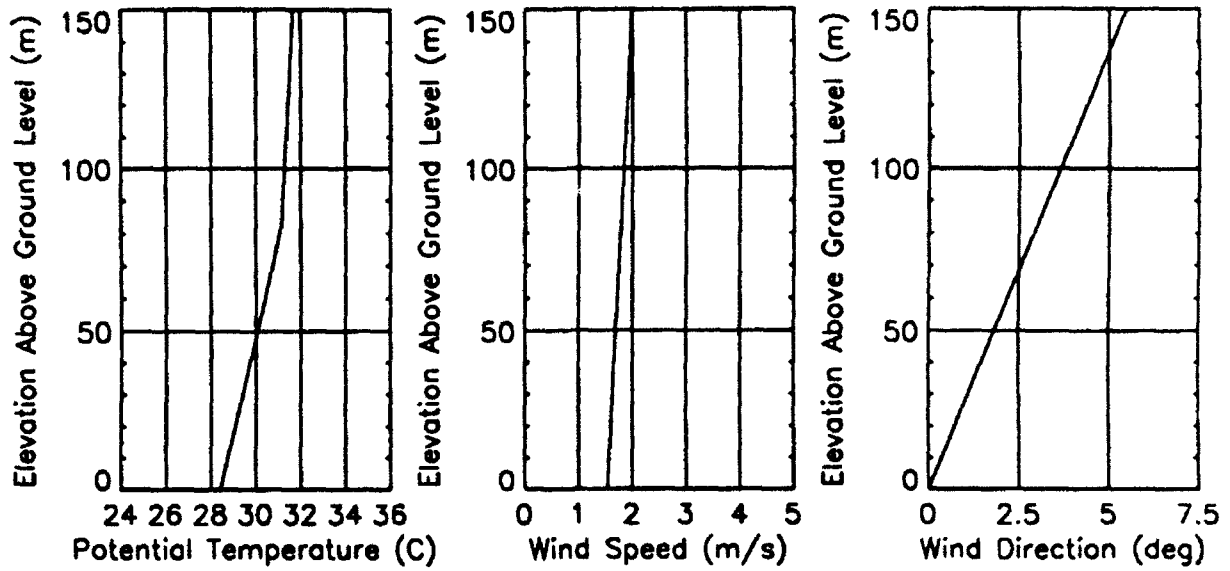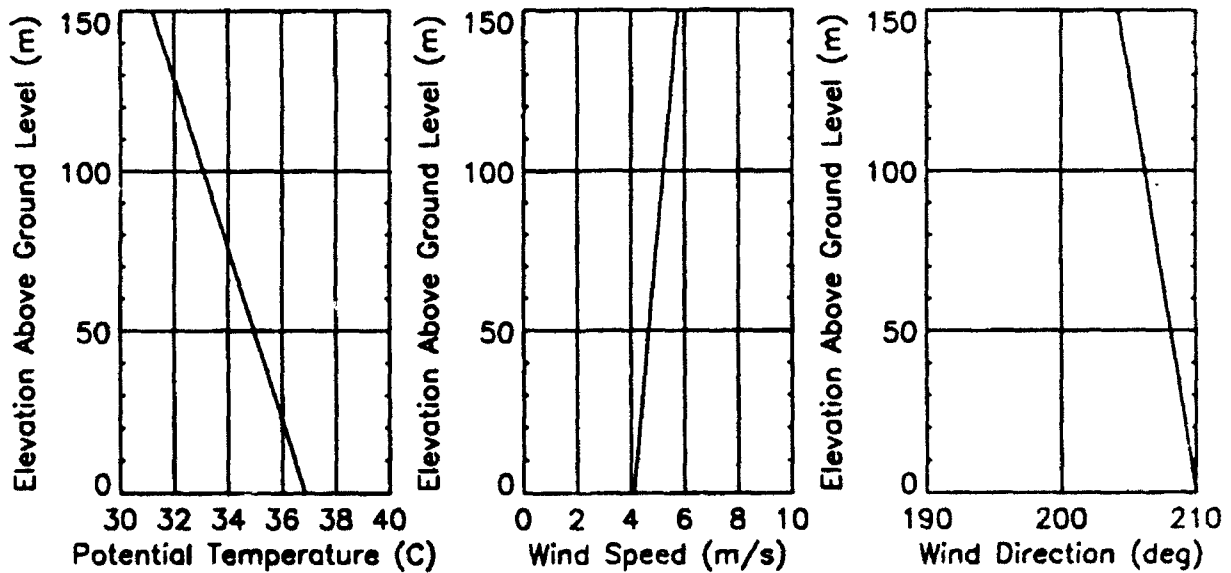
Figure A7. Project WIND stable (a) and unstable (b) meteorological upper air initialization data correlated with the surface observation data in Tables A7.1 and A7.2, respectively.

133
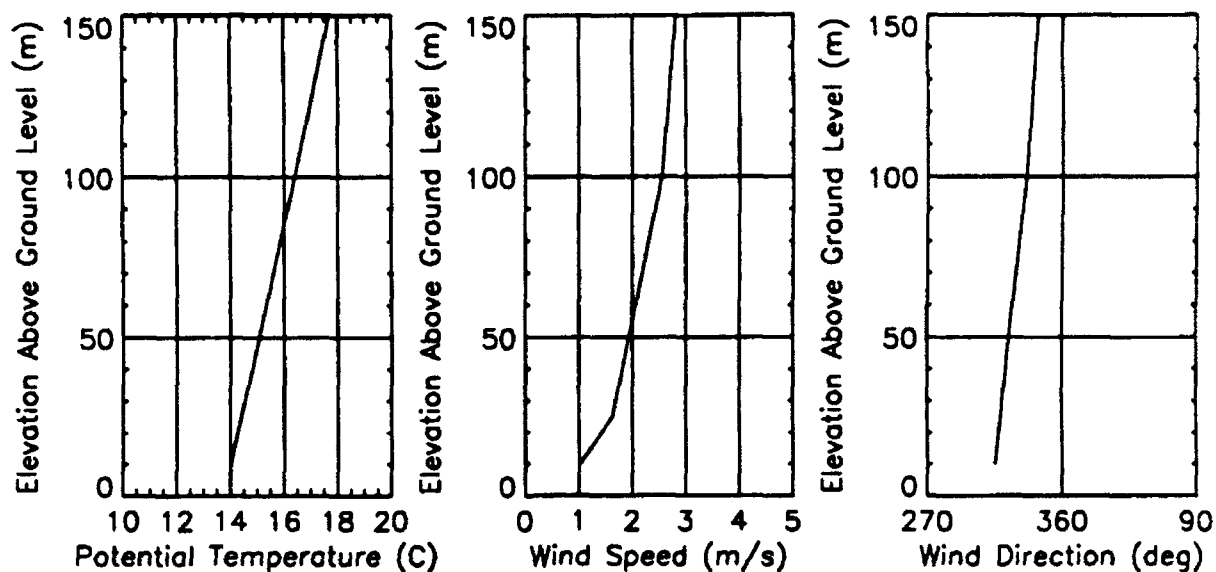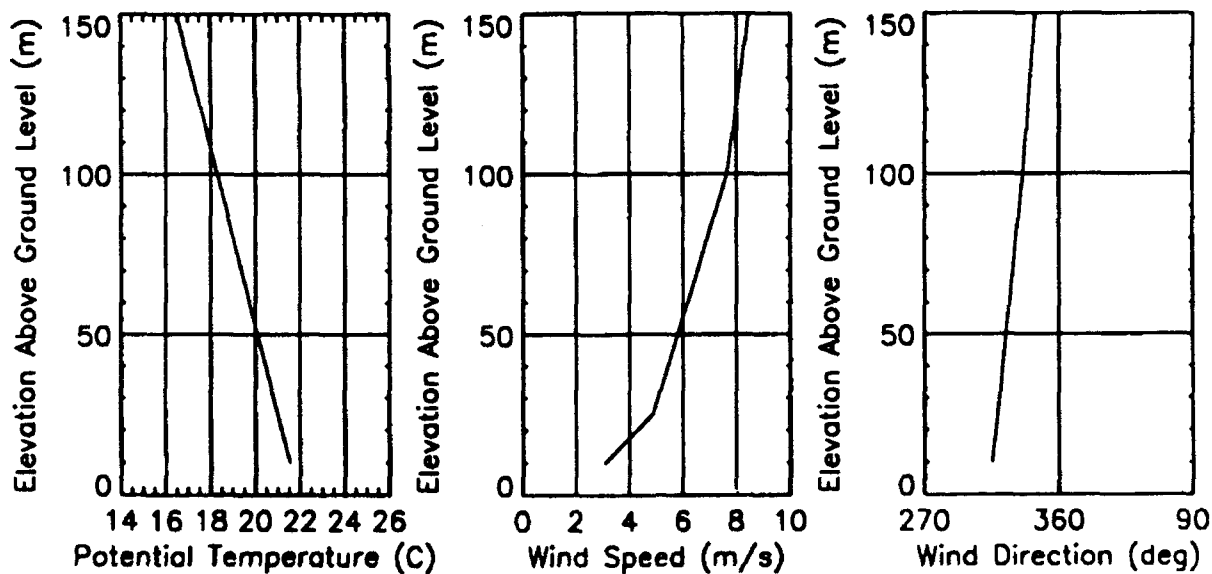
Figure A8. Czechoslovakian stable (a) and unstable (b) modeled upper air initialization scheme that was correlated with the user specified conditions in Ttables A8.1 and A8.2, respectively. Both the stable and unstable profiles were applied to observation sites S-1 and S-2 (see Fig. A4 and Table A4).

Table A12. Approximation for z_o at the NTC from Arya (1988), and the scaling of this z_o value to the normalized variability of the Czechoslovakian site's elevation data (see Table 5). The Czechoslovakian site elevation data had 38% of the NTC site's elevation data variability. The possible range of z_o for hilly-mountainous terrain was set at 1.93-2.50 (from Arya, 1988). The magnitude of this range (0.57) was then scaled to the relative variability of the Czechoslovakian site's terrain elevation data (e.g., $(0.57 \times 0.38) + 1.93 = 2.15$).

Site	STD.DEV.(elevation)	Relative Variability	z_o
NTC	172.57	172.57/172.57 = 1.0	2.5
Czechoslovakia	65.76	65.76/172.57 = 0.38	2.15

Table A13. The friction velocity, u^*, in m/s from the 10 m initialization conditions for the NTC and Czechoslovakian sites (Tables A6 and A8, respectively) using equation A-5.

Site	Stable u^*	Unstable u^*
NTC	0.2972	0.8916
Czechoslovakia	0.2654	0.7963

APPENDIX B

Sample of Analysis Software Source Code

The following source code, written in a Kernighan and Ritchie style C computer programming language, is a sample of the software that was developed to carry out the analysis of wind model outputs (discussed in the Results section). Figure B1 illustrates the file structure of this particular program which was used to process 100 m grid OBWIND and WOCSS results. In the 100 m grid results, each model produced 40,401 u components, as well as 40,401 v components, resulting in a total of 161,604 combined data components per layer (e.g., at 10, 25, and 100 m above ground level).

The program described here performs minimum, mean, maximum, standard deviation, root-mean-squared difference, and agreement index calculations on the separated u and v components of selected OBWIND and WOCSS wind vector files for one layer per program execution. The program also solves for the u and v vector differences over all grid points and calculates the speed of any selected u and v component fields.

Program users specify the names of the two uv data files of interest, as well as the name of the output file near the top of *variables.h*, which is an include file in the main program, *shell.c*. Each significant analysis step carried out in the program was modularized so that users may quickly de-select unnecessary calculations to reduce program run-time (which was typically 115 seconds for a complete analysis run on a Sun SPARCstation IPC computer). Output from a single execution of this program would look similar to the following example:

WSMRstats.100m (Sample Program Output Data File)

min u1 component = -0.462111   min v1 component = -0.250070

Avg u1 component = -0.575035   Avg v1 component = -0.373936

max u1 component = -0.788063   max v1 component = -0.502560

min u2 component = 0.000000   min v2 component = 0.000000

Avg u2 component = -1.190638   Avg v2 component = -0.859763

max u2 component = -1.460600   max v2 component = -1.460600

u1 std.deviation = 0.038507   v1 std.deviation = 0.050773

u2 std.deviation = 0.350084   v2 std.deviation = 0.253497

rmsd for u1-u2   = 0.716975   rmsd for v1-v2   = 0.555462

u1-u2 agmnt indx = 0.999990   v1-v2 agmnt indx = 0.999986

Figure B1. Program file structure and dependencies during program execution.
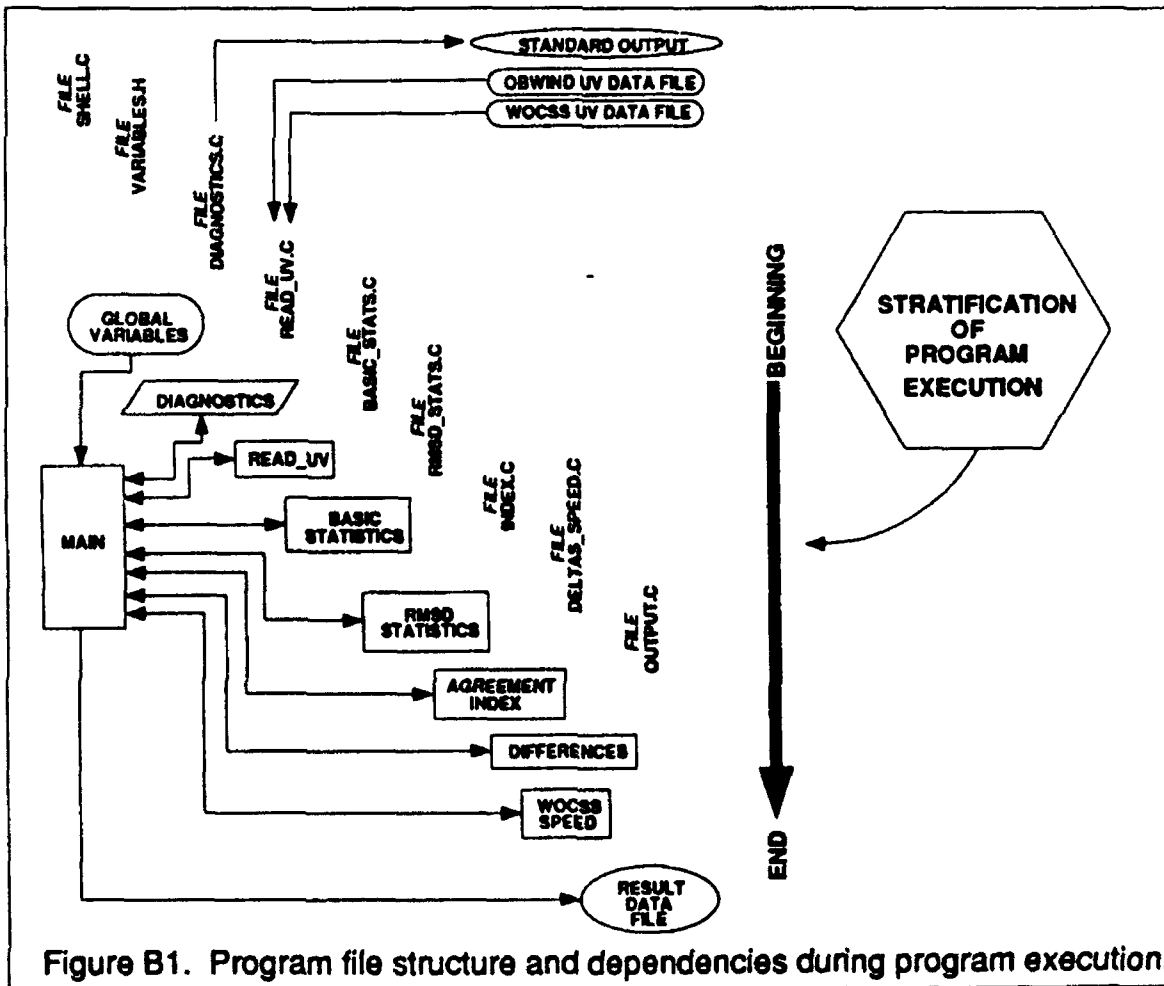
```
/***************************************************************/
/* PROGRAM: SHELL.C;                                        */
/* Date: 06/05/92;                                          */
/* Programmer: Martin Lee;                                  */
/* Purpose: Analyze and compare OBWIND & WOCSS model results; */
/* Use: sys/file.h                                          */
/*      stdio.h                                             */
/*      math.h;                                             */
/*      variables.h allows user to specify file parameters; */
/*      read wind data into program = read_uv.c;            */
/*      a) uv wind file = "wsmr.stable.lvlluv" (example);   */
/*      b) uv wind file = "wsmr.unstable.lvlluv"(example);  */
/***************************************************************/

#include <sys/file.h>
#include <stdio.h>
#include <math.h>/* compile with -lm for access to math library */
#include "variables.h"
#include "diagnostics.c"
#include "read_uv.c"
#include "basic_stats.c"
#include "rmsd_stats.c"
#include "index.c"
#include "deltas_speed.c"
#include "output.c"


/***************************************************************/

main()
{
    printf("\n MAIN calling OBWIND uv READ!\n\n");
    read_uv(UV1,u1,v1);             /* for OBWIND u-v components   */
    printf("\n MAIN calling WOCSS uv READ!\n\n");
    read_uv(UV2,u2,v2);             /* for WOCSS u-v components    */
    printf("\n MAIN calling basic statistics functions!\n\n");
    basic_statistics(&u1stats,u1);    /* for OBWIND u component */
    basic_statistics(&v1stats,v1);    /* for OBWIND v component */
    basic_statistics(&u2stats,u2);    /* for WOCSS u component  */
    basic_statistics(&v2stats,v2);    /* for WOCSS v component  */
/*  diagnostic_1();                           /* preliminary stats */
    printf("\n MAIN calling RMSD agreement index functions!\n\n");
    rmsd_stats(u1,v1,u2,v2);                /* root mean square dif. */
    printf("\n MAIN calling index calculation!\n\n");
    index();                                /* agreement index */
/*  diagnostic_3();                          /* final check */
    printf("\n MAIN calling difference calculation!\n\n");
    difference();                           /* u & v subtractions */
    printf("\n MAIN calling speed calculation!\n\n");
/*  wocss_speed();                           /* WOCSS |uv| speeds */
    printf("\n MAIN calling output routine!\n\n");
    output_stats();                          /* save analysis results */
    printf ("\n END SHELL.C\n");
    return(0);
}
/********************* END shell.c ************************/
```

```
/*********************************************************/
/* variables.h;                                       */
/* Date: 06/05/92;                                    */
/* Programmer: Martir Lee;                            */
/* Purpose: declare glcbal program variable*;         */
/*********************************************************/

#define X       201             /* number of x grid points */
#define Y       201             /* number of y grid points */
#define SIZE    40401           /* total number of points! */
#define UV1 "LEVEL3-UV"         /* OBWIND 100m UV DATA */
#define UV2 "UV3.DATA"          /* WOCSS  100m UV DATA */
#define STATS "WSMRstats.100m"  /* statistical results file */

/*********************************************************/

#define ABS(a)  (float)(sqrt((double)(a)*(a)))
#define SQR(a)  ((a)*(a))
#define pi      3.14159265

/*********************************************************/

struct grid_pt {
                        float component;
                };
struct grid_pt ul[X][Y],v1[X][Y];
struct grid_pt u2[X][Y],v2[X][Y];

/*********************************************************/

struct data_stats {
        float avg;
        float data_avg;
        float min_data;
        float max_data;
        double std;
        double data_std;
        float data_threshold;
                };
struct data_stats u1stats,v1stats;
struct data_stats u2stats,v2stats;

/*********************************************************/

FILE *fp,*u_deltas,*v_deltas,*uv_speed,*output;

/*********************************************************/

char filename[81];
int i,j,num;
float value,u_diff,v_diff,speed;
double u_register,v_register,delta_u,delta_v,rmsd_u,rmsd_v;
double inner_u_sum,w_u_prime,o_u_prime,inner_v_sum;
double w_v_prime,o_v_prime,d_u,d_v;

/****************** END variables.h *******************/
```

```c
/**********************************************************/
/* diagnostics.c                                         */
/* Date: 06/05/92;                                       */
/* Programmer: Martin Lee;                               */
/* Purpose: error detection/trapping;                    */
/**********************************************************/

void
diagnostic_1()
{          /* BEGIN first diagnostic */
   printf("\n in first diagnostic!\n\n");
   printf("Average u1 component = %f\n",u1stats.data_avg);
   printf("Average v1 component = %f\n",v1stats.data_avg);
   printf("min u1 component = %f\n",u1stats.min_data);
   printf("max u1 component = %f\n",u1stats.max_data);
   printf("min v1 component = %f\n",v1stats.min_data);
   printf("max v1 component = %f\n\n",v1stats.max_data);
   printf("Average u2 component = %f\n",u2stats.data_avg);
   printf("Average v2 component = %f\n",v2stats.data_avg);
   printf("min u2 component = %f\n",u2stats.min_data);
   printf("max u2 component = %f\n",v2stats.max_data);
   printf("min v2 component = %f\n",u2stats.min_data);
   printf("max v2 component = %f\n",v2stats.max_data);
   printf ("\n exiting first diagnostic!\n\n");
}          /* END first diagnostic */


void
diagnostic_2()
{          /* BEGIN second diagnostic */
   printf("\n in second diagnostic!\n\n");
   printf("i= %d, j= %d\n",i,j);
   printf("u1= %f\n",u1[i][j].component);
   printf("v1= %f\n",v1[i][j].component);
   printf("u2= %f\n",u2[i][j].component);
   printf("v2= %f\n",v2[i][j].component);
   printf("u_register = %f\n",u_register);
   printf("v_register = %f\n",v_register);
   printf ("\n exiting second diagnostic!\n\n");
}          /* END second diagnostic */


void
diagnostic_3()
{          /* BEGIN third diagnostic */
   printf("\n in third diagnostic!\n\n");
   printf("rmsd for u = %f\n",(float)rmsd_u);
   printf("rmsd for v = %f\n",(float)rmsd_v);
   printf("agreement index for u = %f\n",d_u);
   printf("agreement index for v = %f\n",d_v);
   printf ("\n exiting third diagnostic!\n\n");
}          /* END third diagnostic */

/***************** END diagnostics.c *****************/
```

```
/*******************************************************************/
/* read_uv.c;                                                      */
/* Date: 06/05/92;                                                 */
/* Programmer: Martin Lee;                                         */
/* Purpose: Read UV wind data files;                               */
/*******************************************************************/

void
read_uv(uv_file,u,v)
char uv_file[];
struct grid_pt u[X][Y];
struct grid_pt v[X][Y];
{

   strcpy(filename,uv_file);
   fp = fopen(filename, "r");

   if (fp == NULL)
   {
      printf("Error on open\n");
      exit(0);
   }

   rewind(fp);

   for (i=0; i<=X-1; i++)
   {
      for (j=0; j<=Y-1; j++)
      {
         num = fscanf(fp,"%f",&value);
         if(num != 1)
         {
             printf("Error on u read\n");
             exit(0);
         }
         u[i][j].component = value;
      }
   }

   for (i=0; i<=X-1; i++)
   {
      for (j=0; j<=Y-1; j++)
      {
         num = fscanf(fp,"%f",&value);
         if(num != 1)
         {
             printf("Error on v read\n");
             exit(0);
         }
         v[i][j].component= value;
      }
   }

}
/********************* END read_uv.c *********************/
```

```c
/***************************************************************/
/*  basic_stats.c                                           */
/*  DATE: 06/05/92;                                         */
/*  PURPOSE: perform basic statistical tests on input data array; */
/*  PROGRAMMER: Martin Lee;                                 */
/***************************************************************/
void
basic_statistics(stats,data)
struct data_stats *stats;
struct grid_pt data[X][Y];
{

/* BEGIN Calculation of the MEAN data[X][Y] components */
   stats->avg = 0.0;
   for (i=0; i<X-1; i++)
   {
      for (j=0; j<Y-1; j++)
         stats->avg = stats->avg + data[i][j].component;
   }
   stats->data_avg = stats->avg/SIZE;
/* END Calculation of the MEAN d[X][Y] components */

/* BEGIN Calculation of the MIN, and MAX data[X][Y] components */
   stats->min_data=stats->data_avg;
   stats->max_data=stats->data_avg;
   for (i=0; i<X-1; i++)
   {
      for (j=0; j<Y-1; j++)
      {
         if(ABS(data[i][j].component) < ABS(stats->min_data))
            stats->min_data = data[i][j].component;
         if(ABS(data[i][j].component) > ABS(stats->max_data))
            stats->max_data = data[i][j].component;
      }
   }
/* END Calculation of the MIN, and MAX data[X][Y] components */

/* BEGIN Standard Deviations of the data[X][Y] components */
   stats->std = 0.0;
   for (i=0; i<X-1; i++)
   {
     for (j=0; j<Y-1; j++)
     stats->std = stats->std+SQR(data[i][j].component-stats->data_avg);
   }
   stats->data_std = sqrt(stats->std/SIZE);
/* END Standard Deviations of the data[X][Y] components */

/* BEGIN find |thresholds| of the data[X][Y] components */
   stats->data_threshold = ABS(stats->data_avg) + stats->data_std;
/* END find upper thresholds of the data[X][Y] components */

}
/****************** END basic_stats.c ******************/
```

143

```c
/***********************************************************************/
/*   rmsd_stats.c                                                      */
/*   DATE: 06/05/92;                                                   */
/*   PURPOSE: carry out RMSD calculation on wind model data;           */
/*   PROGRAMMER: Martin Lee;                                           */
/***********************************************************************/

void
rmsd_stats(u1r,v1r,u2r,v2r)
struct grid_pt u1r[X][Y];
struct grid_pt v1r[X][Y];
struct grid_pt u2r[X][Y];
struct grid_pt v2r[X][Y];
{

/* BEGIN RMSD Calculation for u1r-v1r, and u2r-v2r wind fields */

    delta_u = 0.0;
    delta_v = 0.0;
    delta_u = 0.0;
    delta_v = 0.0;

    for (i=0; i<=X-1; i++)
    {
        for (j=0; j<=Y-1; j++)
        {

            delta_u = (u2r[i][j].component)-(u1r[i][j].component);

            u_register = SQR(delta_u) + u_register;



            delta_v = (v2r[i][j].component)-(v1r[i][j].component);

            v_register = SQR(delta_v) + v_register;


/*          diagnostic_2();                      /* rmsd error trap */

        }
    }

    rmsd_u = sqrt(u_register/SIZE);
    rmsd_v = sqrt(v_register/SIZE);

/* END RMSD Calculation for u1r-v1r, and u2r-v2r wind fields */

}

/******************** END rmsd_stats.c ********************/
```

```c
/***************************************************************/
/*   index.c                                                 */
/*   DATE: 06/05/92;                                         */
/*   PURPOSE: agreement index test of wind model data;       */
/*   PROGRAMMER: Martin Lee;                                 */
/***************************************************************/

void
index()
{

/* BEGIN agreement index of ulr-vlr, and u2r-v2r wind fields */

    inner_u_sum = 0.0;
    w_u_prime = 0.0;
    o_u_prime = 0.0;
    inner_v_sum = 0.0;
    w_v_prime = 0.0;
    o_v_prime = 0.0;

    for (i=0; i<=X-1; i++)
    {
       for (j=0; j<=Y-1; j++)
       {

          w_u_prime = ABS(u2[i][j].component - u1stats.data_avg);

          o_u_prime = ABS(u1[i][j].component - u1stats.data_avg);

          inner_u_sum = inner_u_sum + SQR(w_u_prime + o_u_prime);


          w_v_prime = ABS(v2[i][j].component - v1stats.data_avg);

          o_v_prime = ABS(v1[i][j].component - v1stats.data_avg);

          inner_v_sum = inner_v_sum + SQR(w_v_prime + o_v_prime);

       }
    }

    d_u = 1.0 - SIZE*SQR(rmsd_u)/inner_u_sum;

    d_v = 1.0 - SIZE*SQR(rmsd_v)/inner_v_sum;

/* END agreement index of ulr-vlr, and u2r-v2r wind fields */

}

/******************** END index.c ********************/
```

145

```c
/****************************************************************/
/*  deltas_speed.c                                            */
/*  DATE: 06/05/92;                                           */
/*  PURPOSE: find differences and speeds of u and v fields;   */
/*  PROGRAMMER: Martin Lee;                                   */
/****************************************************************/

void
difference()
{
    if((u_deltas=fopen("u.deltas","w+"))==NULL)
    {
       fprintf(stderr,"cannot open u.deltas!\n");
       exit(1);
    }
    rewind(u_deltas);
    if((v_deltas=fopen("v.deltas","w+"))==NULL)
    {
       fprintf(stderr,"cannot open v.deltas!\n");
       exit(1);
    }
    rewind(v_deltas);
    for (i=0; i<=X-1; i++)
    {
       for (j=0; j<=Y-1; j++)
       {
            u_diff = u2[i][j].component - u1[i][j].component;
            fprintf(u_deltas,"%f\n",u_diff);

            v_diff = v2[i][j].component - v1[i][j].component;
            fprintf(v_deltas,"%f\n",v_diff);
       }
    }
}   /* end differences */


void
wocss_speed()
{
    if((uv_speed=fopen("uv.speed","w+"))==NULL)
    {
       fprintf(stderr,"cannot open u.deltas!\n");
       exit(1);
    }
    rewind(uv_speed);
    for (i=0; i<=X-1; i++)
    {
       for (j=0; j<=Y-1; j++)
       {
         speed = sqrt(SQR(u2[i][j].component)+SQR(v2[i][j].component));
         fprintf(uv_speed,"%f\n",speed);
       }
    }
}    /* end wocss_speed */

/******************** END deltas_speed.c ********************/
```

```c
/****************************************************************/
/*  output.c                                                   */
/*  DATE: 06/05/92;                                            */
/*  PURPOSE: file analysis results;                            */
/*  PROGRAMMER: Martin Lee;                                    */
/****************************************************************/

void
output_stats()
{

    strcpy(filename,STATS);
    output = fopen(filename, "w+");

    if (output == NULL)
    {
        printf("Error on open\n");
        exit(0);
    }

    rewind(output);

    fprintf(output,"%s\n",filename);
    fprintf(output,"\n");

    fprintf(output,"min u1 component = %f\n",u1stats.min_data);
    fprintf(output,"min v1 component = %f\n",v1stats.min_data);
    fprintf(output,"Avg u1 component = %f\n",u1stats.data_avg);
    fprintf(output,"Avg v1 component = %f\n",v1stats.data_avg);
    fprintf(output,"max u1 component = %f\n",u1stats.max_data);
    fprintf(output,"max v1 component = %f\n",v1stats.max_data);
    fprintf(output,"\n");
    fprintf(output,"min u2 component = %f\n",u2stats.min_data);
    fprintf(output,"min v2 component = %f\n",u2stats.min_data);
    fprintf(output,"Avg u2 component = %f\n",u2stats.data_avg);
    fprintf(output,"Avg v2 component = %f\n",v2stats.data_avg);
    fprintf(output,"max u2 component = %f\n",v2stats.max_data);
    fprintf(output,"max v2 component = %f\n",v2stats.max_data);
    fprintf(output,"\n");
    fprintf(output,"u1 std.deviation = %f\n",u1stats.data_std);
    fprintf(output,"v1 std.deviation = %f\n",v1stats.data_std);
    fprintf(output,"u2 std.deviation = %f\n",u2stats.data_std);
    fprintf(output,"v2 std.deviation = %f\n",v2stats.data_std);
    fprintf(output,"\n");
    fprintf(output,"rmsd for u = %f\n",(float)rmsd_u);
    fprintf(output,"rmsd for v = %f\n",(float)rmsd_v);
    fprintf(output,"\n");
    fprintf(output,"agreement index for u = %f\n",d_u);
    fprintf(output,"agreement index for v = %f\n",d_v);


}
/******************** END output.c ************************/
```

APPENDIX C

Summary of Software Execution Details

Both the OBWIND model (841 lines of source code) and the WOCSS model (4,343 lines of source code) were installed, configured, compiled, and tested prior to commencement of the model runs. Each model was configured to produce windfield outputs at 10, 25, and 100 m above ground level. Each model was then sequentially initialized and executed with the correct terrain and meteorological data for each study site. Figure C1 maps out all of the OBWIND and WOCSS model runs that were executed to satisfy the cross-model study design goals (illustrated in Fig. 10). Execution of all OBWIND and WOCSS model runs indicated in Fig. C1 produced 5,688,360 wind field data elements. These wind field data elements represented the orthogonal x and y axes components of individual wind vectors, $\vec{V}$, produced by the model runs at each grid point (e.g., $\vec{V} = u\hat{i} + v\hat{j}$, where $u = u\hat{i}$ and $v = v\hat{j}$ are the x and y axes component vectors, respectively; and $\hat{i}$ and $\hat{j}$ are the respective unit vectors along the x and y axes). Table C1 summarizes the number of u and v wind field vector components produced during each model run, and Table C2 summarizes the cumulative total of these components produced from all the model runs executed. Sizes of the resulting computer files containing these wind field components are noted in Table C3.

Table C1. Number of individual wind component data elements produced during both an OBWIND and WOCSS model run.

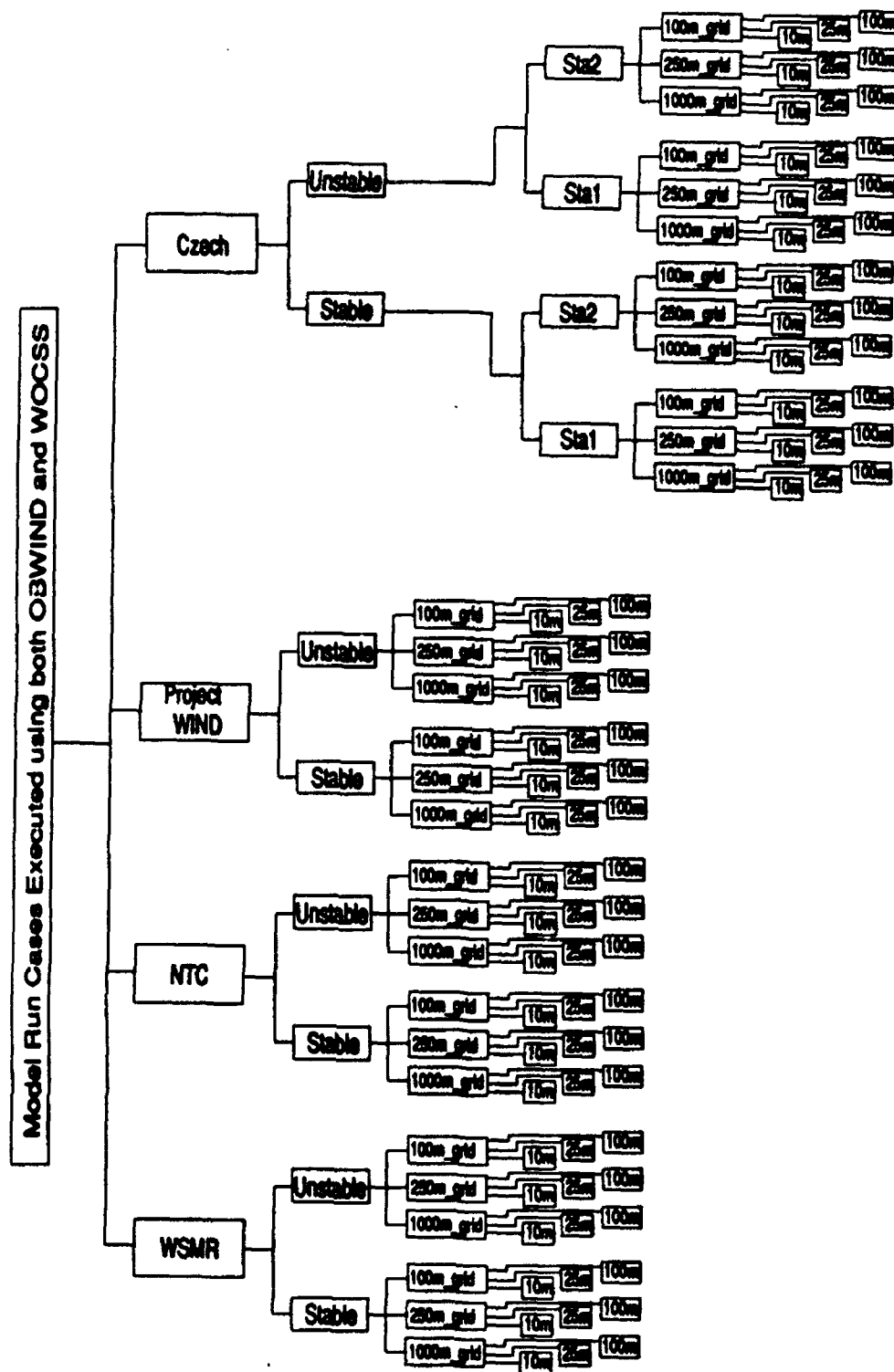| Grid Spacing (m)	u components	v components
1000 (each model run/per layer)	441	441
250 (each model run/per layer)	6,561	6,561
100 (each model run/per layer)	40,401	40,401
Total output/model/layer	47,403	47,403
Combined outputs/model/layer	94,806	

Figure C1. OBWIND and WOCSS model runs were completed, and the horizontal uv wind vector data files were saved for 10, 25, and 100 m above ground level in the file directory scheme illustrated above.

Table C2. Total number of individual data elements produced during OBWIND and WOCSS model runs for WSMR, NTC, Project WIND, and Czechoslovakia.

Model Runs	u components	v components
OBWIND + WOCSS output/layer	94,806	94,806
Stable + Unstable Cases/layer	189,612	189,612
(WSMR+NTC+Proj.WIND)/layer	**568,836**	**568,836**
Czech. sta. 1 stable/layer	189,612	189,612
Czech. sta. 2 unstable/layer	189,612	189,612
Total for Czechoslovakian runs	**379,224**	**379,224**
Cumulative Total for 1 level	948,060	948,060
Cumulative Total for 3 levels	2,844,180	2,844,180
u & v elements from all runs	**5,688,360**	

Table C3. Combined u and v windfield output data file sizes (in kilobytes) for both OBWIND and WOCSS model runs.

Model Runs	100m grid	250m grid	1000m grid
OBWIND/layer/run	329	139	9.3
WOCSS/layer/run	329	139	9.3
OBWIND+WOCSS/layer	658	278	18.6
OBWIND+WOCSS/3 layers	1,974	834	55.8
Stable(S)+Unstable(U) runs	3,948.0	1,668.0	111.6
Cumulative total for S+U runs	**5,727.6**		
Cumulative total for all runs	**34,365.6**		

To produce this resultant output data, model runs required the equivalent of 4.3 hours of uninterrupted, dedicated CPU time (detailed in Tables C4 and C5) on a Sun Microsystems SPARCstation IPC computer workstation. [1] The execution times presented in Tables C4 and C5 are very dependent on the number of layers solved for by each model, as well as on all other user specified input/output configuration specifications.

---

[1] A 17.4 million instructions per second (MIPS), 2.1 million floating point operations per second (MFLOPS), 25-MHz SPARC proccessor platform with 8 MegaBytes of random access memory (RAM) and a 1.2 GigaByte hard disk.

Tables C4 and C5 imply that the WOCSS model executes, on an average basis (over 100, 250, and 1000 m grids), approximately 3 times faster than the OBWIND model. The reduction in WOCSS execution time is primarily due to differences between the OBWIND and WOCSS models' interpolation schemes and internal algorithm process implementation.

Table C4. Typical, dedicated CPU time (in seconds) required to make OBWIND and WOCSS model runs – where all standard output was redirected to a file (e.g., no screen outputs were presented during model execution to reduce bias in program run-times).

Grid Spacing (m)	OBWIND	WOCSS
100 (per run)	994	327
250 (per run)	155	61
1000 (per run)	5.5	5.4
Total (per model run)	1,154.5	393.4
Combined Total/run	1,547.9	

Table C5. Total estimate of dedicated CPU time (in seconds) required to make all cross-case OBWIND and WOCSS model runs – where standard output was redirected to a file (e.g., no screen outputs were presented during model execution to reduce bias in program run-times).

Model runs	OBWIND	WOCSS
Total WSMR runs	2,309.0	786.8
Total NTC runs	2,309.0	786.8
Total Proj.WIND runs	2,309.0	786.8
Total Czech. runs	4,618.0	1,573.6
Cumulative Total	11,545.0	3,934.0
Combined Cum. Total	15,479.0	

DISTRIBUTION LIST FOR PUBLIC RELEASE

Commandant
U.S. Army Chemical School
ATTN: ATZN-CM-CC (S. Barnes)
Fort McClellan, AL 36205-5020

NASA/Marshall Space Flight Center
Deputy Director
Space Science Laboratory
Atmospheric Sciences Division
ATTN: ES01 (Dr. George H. Fichtl)
Huntsville, AL 35812

NASA/Marshall Space Center
ATTN: Code ES44 (Dale Johnson)
Huntsville, AL 35812

NASA/Marshall Space Flight Center
Atmospheric Sciences Division
ATTN: Code ED-41
Huntsville, AL 35812

Deputy Commander
U.S. Army Strategic Defense Command
ATTN: CSSD-SL-L
  Dr. Julius Q. Lilly
P.O. Box 1500
Huntsville, AL 35807-3801

Commander
U.S. Army Missile Command
ATTN: AMSMI-RD-AC-AD
  Donald R. Peterson
Redstone Arsenal, AL 35898-5242

Commander
U.S. Army Missile Command
ATTN: AMSMI-RD-AS-SS
  Huey F. Anderson
Redstone Arsenal, AL 35898-5253

Commander
U.S. Army Missile Command
ATTN: AMSMI-RD-AS-SS
  B. Williams
Redstone Arsenal, AL 35898-5253

Commander
U.S. Army Missile Command
ATTN: AMSMI-RD-DE-SE
  Gordon Lill, Jr.
Redstone Arsenal, AL 35898-5245

Commander
U.S. Army Missile Command
Redstone Scientific Information
  Center
ATTN: AMSMI-RD-CS-R/Documents
Redstone, Arsenal, AL 35898-5241

Commander
U.S. Army Intelligence Center
  and Fort Huachuca
ATTN: ATSI-CDC-C (Mr. Colanto)
Fort Huachuca, AZ 85613-7000

Northrup Corporation
Electronics Systems Division
ATTN: Dr. Richard D. Tooley
2301 West 120th Street, Box 5032
Hawthorne, CA 90251-5032

Commander - Code 3331
Naval Weapons Center
ATTN: Dr. Alexis Shlanta
China Lake, CA 93555

Commander
Pacific Missile Test Center
Geophysics Division
ATTN: Code 3250 (Terry E. Battalino)
Point Mugu, CA 93042-5000

Lockheed Missiles & Space Co., Inc.
Kenneth R. Hardy
Org/91-01 B/255
3251 Hanover Street
Palo Alto, CA 94304-1191

Commander
Naval Ocean Systems Center
ATTN: Code 54 (Dr. Juergen Richter)
San Diego, CA 92152-5000

Meteorologist in Charge
Kwajalein Missile Range
P.O. Box 67
APO San Francisco, CA 96555

U.S. Department of Commerce
Mountain Administration Support
    Center
Library, R-51 Technical Reports
325 S. Broadway
Boulder, CO 80303

Dr. Hans J. Liebe
NTIA/ITS S 3
325 S. Broadway
Boulder, CO 80303

NCAR Library Serials
National Center for Atmos Rsch
P.O. Box 3000
Boulder, CO 80307-3000

HQDA
ATTN: DAMI-POI
Washington, DC 20310-1067

Mil Asst for Env Sci Ofc of
    The Undersecretary of Defense
for Rsch & Engr/R&AT/E&LS
Pentagon - Room 3D129
Washington, DC 20301-3080

HQDA
DEAN-RMD/Dr. Gomez
Washington, DC 20314

Director
Division of Atmospheric Science
National Science Foundation
ATTN: Dr. Eugene W. Bierly
1800 G. Street, N.W.
Washington, DC 20550

Commander
Space & Naval Warfare System Command
ATTN: PMW-145-1G (LT Painter)
Washington, DC 20362-5100

Commandant
U.S. Army Infantry
ATTN: ATSH-CD-CS-OR
    Dr. E. Dutoit
Fort Benning, GA 30905-5090

USAFETAC/DNE
Scott AFB, IL 62225

Air Weather Service
Technical Library - FL4414
Scott AFB, IL 62225-5458

USAFETAC/DNE
ATTN: Mr. Charles Glauber
Scott AFB, IL 62225-5008

Commander
U.S. Army Combined Arms Combat
ATTN: ATZL-CAW (LTC A. Kyle)
Fort Leavenworth, KS 66027-5300

Commander
U.S. Army Space Institute
ATTN: ATZI-SI (Maj Koepsell)
Fort Leavenworth, KS 66027-5300

Commander
U.S. Army Space Institute
ATTN: ATZL-SI-D
Fort Leavenworth, KS 66027-7300

Commander
Phillips Lab
ATTN: PL/LYP (Mr. Chisholm)
Hanscom AFB, MA 01731-5000

Director
Atmospheric Sciences Division
Geophysics Directorate
Phillips Lab
ATTN: Dr. Robert A. McClatchey
Hanscom AFB, MA 01731-5000

Raytheon Company
Dr. Charles M. Sonnenschein
Equipment Division
528 Boston Post Road
Sudbury, MA 01776
Mail Stop 1K9

Director
U.S. Army Materiel Systems
  Analysis Activity
ATTN: AMXSY-MP (H. Cohen)
APG, MD 21005-5071

Commander
U.S. Army Chemical Rsch,
  Dev & Engr Center
ATTN: SMCCR-OPA (Ronald Pennsyle)
APG, MD 21010-5423

Commander
U.S. Army Chemical Rsch,
  Dev & Engr Center
ATTN: SMCCR-RS (Mr. Joseph Vervier)
APG, MD 21010-5423

Commander
U.S. Army Chemical Rsch,
  Dev & Engr Center
ATTN: SMCCR-MUC (Mr. A. Van De Wal)
APG, MD 21010-5423

Director
U.S. Army Materiel Systems
  Analysis Activity
ATTN: AMXSY-AT (Mr. Fred Campbell)
APG, MD 21005-5071

Director
U.S. Army Materiel Systems
  Analysis Activity
ATTN: AMXSY-CR (Robert N. Marchetti)
APG, MD 21005-5071

Director
U.S. Army Materiel Systems
  Analysis Activity
ATTN: AMXSY-CS (Mr. Brad W. Bradley)
APG, MD 21005-5071

Director
U.S. Army Research Laboratory
ATTN: AMSRL-D
2800 Powder Mill Road
Adelphi, MD 20783

Director
U.S. Army Research Laboratory
ATTN: AMSRL-OP-CI-A
  (Technical Publishing)
2800 Powder Mill Road
Adelphi, MD 20783

Director
U.S. Army Research Laboratory
ATTN: AMSRL-OP-CI-D, Record Copy
2800 Powder Mill Road
Adelphi, MD 20783

Director
U.S. Army Research Laboratory
ATTN: AMSRL-SS-SH
  Dr. Z.G. Sztankay
2800 Powder Mill Road
Adelphi, MD 20783

National Security Agency
ATTN: W21 (Dr. Longbothum)
9800 Savage Road
Ft George G. Meade, MD 20755-6000

U. S. Army Space Technology
  and Research Office
ATTN: Brenda Brathwaite
5321 Riggs Road
Gaithersburg, MD 20882

OIC-NAVSWC
Technical Library (Code E-232)
Silver Springs, MD 20903-5000

The Environmental Research
  Institute of Michigan
ATTN: IRIA Library
P.O. Box 134001
Ann Arbor, MI 48113-4001

Commander
U.S. Army Research Office
ATTN: DRXRO-GS (Dr. W.A. Flood)
P.O. Box 12211
Research Triangle Park, NC 27709

Dr. Jerry Davis
North Carolina State University
Department of Marine, Earth, &
  Atmospheric Sciences
P.O. Box 8208
Raleigh, NC 27650-8208

Commander
U. S. Army CECRL
ATTN: CECRL-RG (Dr. H. S. Boyne)
Hanover, NH 03755-1290

Commanding Officer
U.S. Army ARDEC
ATTN: SMCAR-IMI-I, Bldg 59
Dover, NJ 07806-5000

U.S. Army Communications-Electronics
  Command EW/RSTA Directorate
ATTN: AMSEL-RD-EW-OP
Fort Monmouth, NJ 07703-5206

Commander
U.S. Army Satellite Comm Agency
ATTN: DRCPM-SC-3
Fort Monmouth, NJ 07703-5303

6585th TG (AFSC)
ATTN: RX (CPT Stein)
Hollomar AFB, NM 88330

Department of the Air Force
OL/A 2nd Weather Squadron (MAC)
Holloman AFB, NM 88330-5000

PL/WE
Kirtland AFB, NM 87118-6008

Director
U.S. Army TRADOC Analysis Command
ATTN: ATRC-WSS-R
White Sands Missile Range, NM 88002

USAF Rome Laboratory Technical
Library, FL2810 Corridor W, Site 262,
RL//SUL (DOCUMENTS LIBRARY)
26 Electronics Parkway, Bldg 106
Griffiss AFB, NY 13441-4514

AFMC/DOW
Wright-Patterson AFB, OH 0334-5000

Commandant
U.S. Army Field Artillery School
ATTN: ATSF-TSM-TA
  Mr. Charles Taylor
Fort Sill, OK 73503-5600

Commander
Naval Air Development Center
ATTN: Al Salik (Code 5012)
Warminister, PA 18974

Commander
U.S. Army Dugway Proving Ground
ATTN: STEDP-MT-DA-M
  Mr. Paul Carlson
Dugway, UT 84022

Commander
U.S. Army Dugway Proving Ground
ATTN: STEDP-MT-DA-L
Dugway, UT 84022

Commander
U.S. Army Dugway Proving Ground
ATTN: STEDP-MT-M (Mr. Bowers)
Dugway, UT 84022-5000

Defense Technical Information Center
ATTN: DTIC-FDAC   (2)
Cameron Station
Alexandria, VA 22314

Commanding Officer
U.S. Army Foreign Science &
  Technology Center
ATTN: CM
220 7th Street, NE
Charlottesville, VA 22901-5396

Naval Surface Weapons Center
Code G63
Dahlgren, VA 22448-5000

Commander
U.S. Army OEC
ATTN: CSTE-EFS
Park Center IV
4501 Ford Ave
Alexandria, VA 22302-1458

Commander and Director
U.S. Army Corps of Engineers
Engineer Topographics Laboratory
ATTN: ETL-GS-LB
Fort Belvoir, VA 22060

TAC/DOWP
Langley AFB, VA 23665-5524

U.S. Army Topo Engineering Center
ATTN: CETEC-ZC
Fort Belvoir, VA 22060-5546

Commander
Logistics Center
ATTN: ATCL-CE
Fort Lee, VA 23801-6000

Commander
USATRADOC
ATTN: ATCD-FA
Fort Monroe, VA 23651-5170

Science and Technology
101 Research Drive
Hampton, VA 23666-1340

Commander
U.S. Army Nuclear & Cml Agency
ATTN: MONA-ZB Bldg 2073
Springfield, VA 22150-3198